ISSN 2435-1288

Nikon Research Report

Vol.7 2025

Purpose of publication

This publication is being created to widely introduce the achievements of research and development activities conducted by Nikon Corporation. This is a result of R&D based on Nikon's core technologies of "opto-electronics" and "precision" technologies that have been incorporated in new products and/or often valued by external organizations such as academic societies.

Foreword

Director
Senior Executive Vise President
CTO

Yasuhiro Ohmura

Amid constant changes in the natural environment and society, we face diverse challenges every day. At Nikon, we aim to contribute to the realization of a sustainable society through our business activities by deeply understanding our customers' true needs, collaborating on solutions, and driving innovation together.

We have pursued our vision of becoming *a key technology solutions company in a global society where humans and machines co-create seamlessly* by 2030. This year concludes our current medium-term management plan and serves as the period in which we will formulate our next medium-term plan. To fulfill our vision and meet the expectations of society and our customers, we are committed to exploring the value we can deliver and advancing the technologies that form the foundation for value creation.

Executive Fellow
General Manager of Advanced Technology
Research & Development

Masaaki Doi

I am pleased to present this year's report showcasing the Nikon Group's research and development initiatives. You will find cutting-edge technologies related to each of our business fields, with a focus on our core strengths in applied optics and precision technologies.

In the field of Digital Manufacturing, we highlight the metal additive manufacturing technology we focused on growing towards 2030. In the field of Healthcare business, microscopy technology facilitating assisted reproductive health is featured. From our Imaging business, we feature a power zoom lens with Nikon's renowned optical performance and added enhanced video capabilities. In addition, an innovative in-vehicle camera system that integrates a telephoto lens and a wide-angle lens to capture both distant and peripheral areas simultaneously is described. You will also find optical technology for free-space optical communications via satellites, and encoder technology widely used in industrial machinery such as industrial robots.

Although this report offers only a glimpse into the Nikon Group's technological advancements, I hope it provides greater awareness of our initiatives and inspires new opportunities for Nikon's technologies to benefit society and the environment.

Nikon Research Report Vol.7
目次／ CONTENTS

技術解説/Technical Reports

研究開発論文/Research and Development Reports

技術解説

Technical Reports

Lasermeister LM300A＋SB100で実現する自動補修ソリューションの紹介

安葉浩一

Introduction to Automated Repair Solution Enabled by Lasermeister LM300A + SB100

Koichi YASUBA

ニコンは2019年に金属3D プリンター Lasermeister 100A を発売し，2024年には LM300A と SB100を発売し，これら装置を用いた自動補修ソリューションを提案した．LM300A は大出力レーザーと造形空間の拡大により，タービンブレードなどの大型部品補修に対応する．SB100は内蔵3D スキャナーによる高精度な形状計測や補修部位の自動抽出，さらに LM300A 用の加工パス自動生成を行う．両機をセットで使用することで，計測から積層造形まで一連の自動補修プロセスを高精度かつ安定して繰り返し実行できる点が大きな強みである．タービンブレード補修では現品の歪みといった予測困難な課題にも対応し，±0.25 mm 以内の高精度補修を実現した．設計モデルがなくとも現物計測データのみで補修形状を生成でき，幅広い実務ニーズに応える．今後は金型など薄肉補修にも展開し，顧客ニーズに応じた自動補修ソリューションの拡充を目指す．

Nikon launched the metal three-dimensional (3D) printer Lasermeister 100A in 2019 and introduced LM300A and SB100 in 2024, based on which an automated repair solution was proposed. LM300A is equipped with a high-power laser and features a large build volume, thus enabling the repair of large components such as turbine blades. SB100 features a built-in 3D scanner for the precise measurement and automatic extraction of damaged areas, as well as for the automatic generation of tool paths for use with LM300A. This solution is advantageous as it uses both devices simultaneously, thus enabling a highly accurate and stable automated repair process from measurement to additive manufacturing. In repairing turbine blades, the system used can accommodate unpredict issues such as the deformation of actual components and affords a repair accuracy of ± 0.25 mm. Moreover, in cases where the original design model is unavailable, the system can generate repair shapes solely from measurement data, thus satisfying a wide range of practical requirements. In the future, Nikon plans to expand this solution to thin-walled components such as molds, thereby enhancing automated repair solutions in response to diverse customer requirements.

Key words 金属積層造形，3D 計測，欠損部位特定，タービンブレード補修，金型補修
additive manufacturing, 3D measurement, defect-area identification, turbine-blade repair, mold repair

1 Introduction

In 2019, Nikon launched the Lasermeister 100A (hereinafter referred to as the LM100A) optical processing machine (Fig. 1) as a new business initiative.

The LM100A is a metal additive manufacturing system, commonly referred to as a 3D printer, developed by applying one of Nikon's core competencies—laser control technology.

The LM101A, incorporating a five-axis mechanism, and the LM102A, equipped with advanced melt-control functions, have also been launched. Figure 2 shows the inspection of the build volume in the LM102A.

The LM100A series employs the Directed Energy Deposi-

Fig. 1　Lasermeister 100A

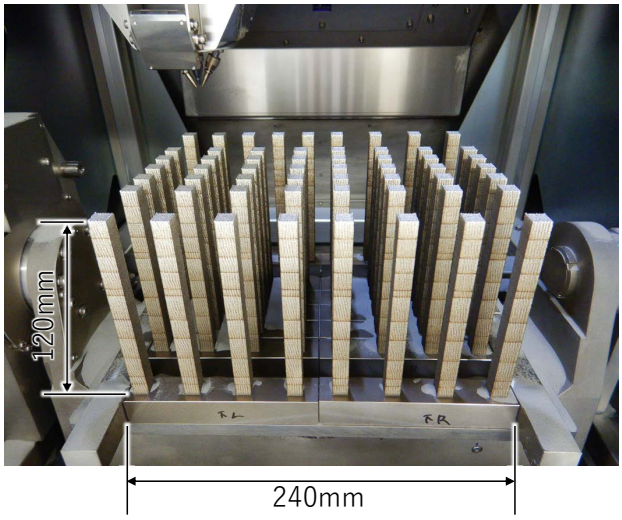

Fig. 2　Build scene using the Lasermeister 102A

Fig. 3
Lasermeister LM300A (right)
Lasermeister SR100 (left)

tion (DED) method, which involves the use of metal powder and a laser. Hereinafter, this “DED method using metal powder and a laser” is referred to simply as DED.

A method that is in contrast to DED is Laser Powder Bed Fusion (L-PBF), a method employed in Nikon SLM Solutions' systems. While both DED and L-PBF fabricate parts by irradiating metal powder with a laser to melt the metal, they differ significantly in how the metal powder is supplied. DED fabricates parts by irradiating the target object with a laser and concentrically supplying metal powder to the region of the target that has been melted. In contrast, L-PBF fabricates parts by irradiating a flat surface called a powder bed to melt the metal powder that is uniformly spread over the powder bed. Because of this difference in the metal powder supply principle, the fabrication approaches in which each method excels also differ.

One of the advantages DED has over L-PBF is that it facilitates additive manufacturing onto existing components. Given its metal powder supply principle, L-PBF inevitably covers the part fabricated up to that point with the metal powder it supplies. However, in additive manufacturing onto existing components, the process results in the existing parts being completely covered, making it difficult to determine the laser irradiation position. In contrast, with DED, the object to be irradiated by the laser is always visible, making it easier to align with the position where additive manufacturing is to be performed.

Leveraging this advantage and addressing customer needs, the Lasermeister LM300A and Lasermeister SB100 (Fig. 3) were newly developed, targeting “repair” applications, and launched in 2024. Hereinafter, they are referred to as LM300A and SB100, respectively.

2 Features of LM300A + SB100

The LM300A inherits the design lineage of the LM100A series. However, compared with the LM100A (maximum laser power: 200 W; build volume in vertical direction: 200 mm), the LM300A is designed with an increased maximum laser power of 300 W, providing greater melting capability, and a build volume of 400 mm in the vertical direction, making it easier to accommodate existing components. The expanded size in the vertical direction results from small gas turbine blades adopted as a concrete model for repair fabrication.

The primary role of the SB100 is to automate the repair process. The main hardware function it incorporates is a non-contact 3D measurement device, commonly referred to as a 3D scanner. Using this measuring instrument, the system performs shape measurement of the repair target, identification of the repair location, and generation of the geometry of the repair area. Furthermore, it has the capability of interfacing with the LM300A to generate machining paths executable by the LM300A.

By appropriately setting up the LM300A and SB100, it is possible to repeatedly perform repairs under identical conditions for repair targets of the same shape.

3 Concept of Repair Fabrication

The repair process is illustrated in Fig. 4.

(1) Initial setup

Set various parameters related to the repair, including the measurement conditions, laser power, powder feed rate, and model of the final shape serving as the repair

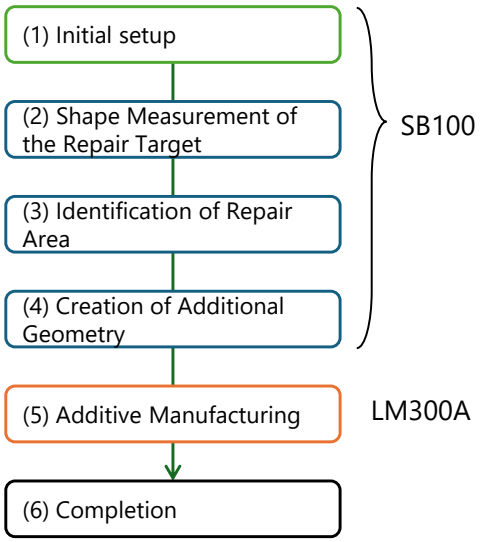

Fig. 4 Repair process

goal. It was determined that these settings need not be changed as long as both the final shape and the type of damage or wear remain unchanged.

(2) Shape Measurement of the Repair Target

The built-in 3D scanner is used to measure the shape of the repair target.

(3) Identification of Repair Area

The difference between the finished-shape model set in (1) and the 3D measurement results obtained with the 3D scanner is calculated. This difference corresponds to the defect area, which is the repair area itself.

(4) Creation of Additional Geometry

The shape of the repair area can be directly used for additive manufacturing. Based on the repair area identified in (3), a set of machining path data is generated for operating the LM300A, including all control commands for managing laser irradiation positions and power.

(5) Additive Manufacturing

The LM300A performs additive manufacturing based on the above machining path.

Based on the additive manufacturing capabilities developed with the LM100A, automation functions to facilitate "repair" were added and offered as the SB100. By adopting this concept, it became possible to make full use of the proven existing functions on the manufacturing unit side almost as they are, while focusing efforts on developing measurement functions for highly accurate detection of repair areas and on execution-control functions for implementing the repair strategy.

It should be noted that, when using the two devices based on the above concept, the challenge lies in position management. In this system, the measurement/manufacturing target is fixed to a designated table, which itself is transported between the devices. In other words, the table serves to link the two devices, and positional reproducibility among the two devices and the table is of critical importance. It is imperative to prevent any displacement of the measurement target (i.e., the additive manufacturing target) during this transfer and ensure high-precision positional reproducibility when installing the table itself.

To ensure positional reproducibility between the table and each device, a kinematic mount structure (Fig. 5) was adopted. The kinematic mount allows table installation to be performed with great ease and convenience while ensuring positional reproducibility, with an error of less than 0.01 mm.

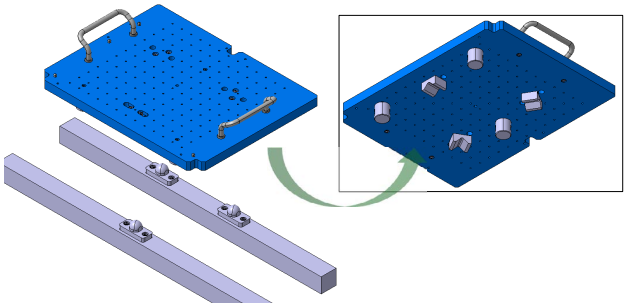

Fig. 5 Kinematic mount structure

In this way, position management between the LM300A and SB100 is made possible, with the table serving as the reference. For example, if a fixed point on the table that can be recognized by both the LM300A and SB100 is defined as the positional reference, then every location on the table can be uniquely correlated between the LM300A and SB100.

4 Turbine Blade Repair

In developing the LM300A, the initial repair target was set as turbine blades. Noting the fact that a viable repair business already exists, we collaborated with companies engaged in repair operations and set a practical goal of replacing the manual portions of existing business processes with the LM300A + SB100.

As a specific example, we focused on damage caused by wear at the blade tip (i.e., the blade's top end), which accounts for a large proportion of turbine blade repairs, setting the maximum blade length at 400 mm or less and the allowable positional deviation for additive manufacturing within ± 0.25 mm.

The specific repair targets are shown in Fig. 6.

In practice, several issues arose, the most significant

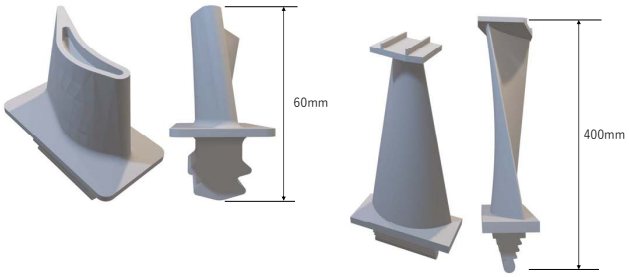

Fig. 6　Two types of turbine blade shapes targeted for repair

being deformation of the repair target itself. Compared with the turbine blade's design model, the actual component was significantly deformed, on the order of millimeters. It was found that simply calculating the difference between the design model and actual measurement results did not yield the intended additional geometry (Fig. 7).

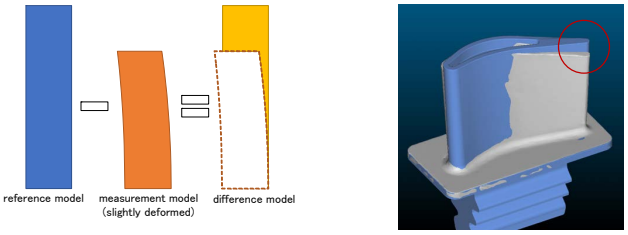

Fig. 7　Deformation of actual turbine blade

Ultimately, two methods were implemented.

The first method involves fitting the design model to the measurement results as closely as possible and then calculating the difference (Fig. 8). While this method is sufficiently versatile, there was concern about uncertainty arising from deforming the design model to match the actual component, which could cause the additional geometry to become unexpectedly distorted.

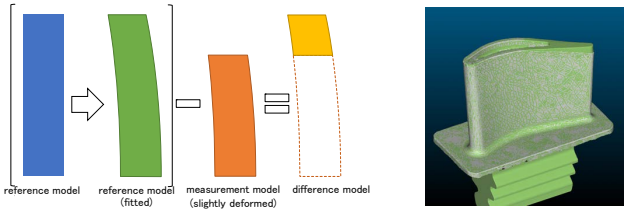

Fig. 8　Fitting the design model to the measurement results

The second method does not use the design model; instead, the measurement results are extended in the top-surface direction, and this increment is taken as the additional geometry (Fig. 9).

As this method simply extends the shape in the specified direction without applying smoothing or other processing, there was concern about the effect of discontinuities in the side-surface geometry on the manufacturing results. Fortu-

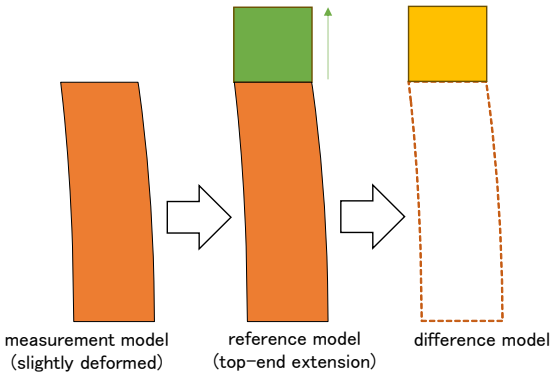

Fig. 9　Simple extension

nately, because post-processing for finishing was anticipated after manufacturing, it was determined that any such effects could be sufficiently remedied during subsequent machining. Given this background, it was found that this method was, in fact, well-suited for blade tip repair, and it was therefore adopted. In addition, turbine blade repair is often performed by companies who do not manufacture the blades, and in many cases, the design models themselves are difficult to obtain. Therefore, the fact that this method does not require a design model for comparison was also well-received.

These results are shown in Figs. 10 and 11.

Fig. 10　Turbine blade tip repair

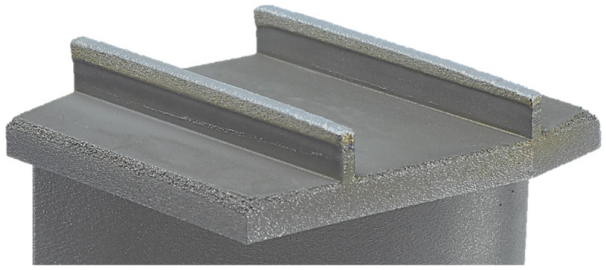

Fig. 11　Turbine blade shroud repair

The results of the shape measurement after repair manufacturing are shown in Fig. 12. This shows the difference between the repair result and repair target. As mentioned

earlier, the allowable target positional deviation was ± 0.250 mm; however, these results show that it is generally in the range of 0 to 0.5 mm. It was also discovered during the collaboration that, in repair work, a negative deviation (i.e., smaller than the target) is an unacceptable outcome. For the purpose of finishing the shape through post-processing, it became a mandatory requirement that the result be positive (i.e., larger than the target). In consideration of this, the additional machining model was designed to be approximately 0.25 mm larger around the entire circumference. This ensures that, even when accounting for the ± 0.25 mm positional deviation, subtracting the repair target shape from the repair result will not yield a negative value.

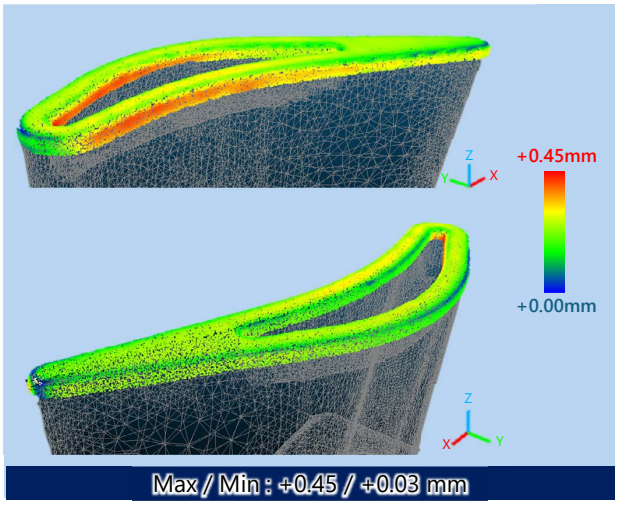

Fig. 12　Turbine blade tip repair measurement

5 Conclusion

Turbine blade repair, with its well-defined procedures and visually distinguishable defect areas, was an optimal first step for Nikon's proposed repair solution. In this way, we continue to demonstrate the value of the LM300A + SB100 through concrete applications. Having been able to present a clear example through turbine blade repair, we are fortunate to have also identified other repair needs. While turbine blade repairs involved several millimeters of build thickness, one such newly identified need is mold repair, which requires thin builds on the order of several hundred micrometers.

Going forward, we plan to further enhance repair applications using the Lasermeister, thereby leveraging Nikon's proprietary technologies to provide timely responses to specific requests.

安藁浩一　Koichi YASUBA
アドバンストマニュファクチャリング事業部
事業企画部
Business Planning Department
Advanced Manufacturing Business Unit

生殖補助医療技術における ICSI/IMSI と紡錘体観察

三宅範夫

ICSI/IMSI and Spindle Observation in Assisted Reproductive Technology†

Norio MIYAKE

生殖補助医療技術（ART: Assisted Reproductive Technology）の役割と，それを支える顕微鏡技術について紹介する．不妊症のカップルにとって ART は重要な選択肢であり，日本では2022年 4 月の不妊治療保険適用の開始以降，ART による新生児の割合が増加している．

ART は，卵子や精子，受精胚を扱い妊娠を支援する医療技術であり，顕微鏡を使用する体外受精（IVF）や卵細胞質内精子注入法（顕微授精，ICSI），卵細胞質内形態選別精子注入法（IMSI）などを含んでいる．ニコンは ART の各ステップに対応する正立顕微鏡，実体顕微鏡，倒立顕微鏡を提供しており，ART プロセスを支援している．例えば，正立顕微鏡は精子の運動性や形態の観察に適しており，実体顕微鏡は卵子や胚の立体的な観察を可能にする．一方，倒立顕微鏡は ICSI/IMSI の際に精子や卵子の詳細な観察を行い，Nikon Advanced Modulation Contrast（NAMC）や微分干渉観察によりコントラストを向上させる．また，紡錘体観察では円偏光を利用し，卵子内の紡錘体の配置を把握することで受精率を高めている．

これらの光学技術は，ART プロセスの効率化と精度向上に貢献しており，医療現場での負担軽減と治療成果の向上につながっている．ニコンはこれらの技術開発を通じて，社会的課題を解決するため取り組んでいる．

This article introduces the role of assisted reproductive technology (ART) and the microscopic techniques supporting it. ART is an important option for couples facing infertility. In Japan, since the implementation of insurance coverage for infertility treatments in April 2022, the proportion of newborns conceived through ART has been increasing. ART encompasses medical techniques that assist pregnancy by handling eggs, sperm, and embryos, including in-vitro fertilization (IVF), intracytoplasmic sperm injection (ICSI), and intracytoplasmic morphologically selected sperm injection (IMSI), which rely on microscopes for precision.

Nikon provides specialized microscopes, including upright, stereo, and inverted microscopes, tailored for each step of the ART process. Upright microscopes are ideal for analyzing sperm motility and morphology, whereas stereo microscopes enable three-dimensional observation of eggs and embryos. Inverted microscopes facilitate detailed observation during ICSI and IMSI procedures and use technologies such as Nikon advanced modulation contrast and differential interference contrast to enhance image clarity. Furthermore, spindle observation using circular polarization helps to identify spindle positioning within the eggs, which improves the success rates of fertilization.

These optical technologies increase the efficiency and accuracy of ART processes, reduce the burden on medical professionals, and improve the treatment outcomes. Nikon contributes to addressing the societal challenges through these innovations.

Key words 生殖補助医療技術，体外受精，顕微授精，IMSI, 紡錘体観察
assisted reproductive technology, in-vitro fertilization, intracytoplasmic sperm injection, intracytoplasmic morphologically selected sperm injection, spindle observation

1 Introduction

Declining birthrates have become a serious challenge not only in Japan but also in many other countries. The continuing decline in birthrates has social and economic impacts, including a decrease in the working population, the collapse of social security systems, and stagnation of economic growth. Various factors have been cited as causes of the declining birthrate, including the economic burdens of child rearing and education, lifestyle changes resulting from the

† The products introduced in this article are available in many countries worldwide; however, the technical explanations provided here are based on Japanese regulations. Please note that the availability and primary intended use may vary depending on your region/country.

increased women's participation in the workforce, and a rise in infertility attributable to environmental and health-related issues. In particular, for couples who wish to have children but find natural conception difficult, assisted reproductive technology (ART) represents an important option. In Japan, the total fertility rate has been steadily declining over the past 40 years [1]. Meanwhile, the proportion of newborns conceived through ART has been increasing. Furthermore, since April 2022, infertility treatments have been covered by insurance, and the number of general infertility treatments, such as artificial insemination, as well as ART, such as in-vitro fertilization (IVF) and intracytoplasmic sperm injection (ICSI), is expected to continue increasing in the future.

Throughout the history of assisted reproductive technology, Nikon has consistently collaborated with academia and medical institutions to develop groundbreaking products rooted in the needs of clinical practice. In recent years, aiming to reduce the workload of embryologists who support assisted reproductive technology, Nikon has been providing microscopes specialized for use in micro-insemination [2]. This paper presents an overview of ART and the microscopic techniques that support it.

2 Assisted Reproductive Technology (ART)

ART refers to medical technologies for treating infertility and supporting pregnancy and is a collective term encompassing all treatments and methods that involve handling human eggs and sperm, as well as the embryos fertilized from them, to achieve pregnancy. Even when the cause of infertility lies with the male partner, female partner, or both, pregnancy can be pursued through the use of appropriate techniques. A wide range of causes, including ovulatory disorders, tubal obstruction, endometriosis, reduced sperm quality, and immunological infertility, can be addressed. By employing IVF, ICSI, or intracytoplasmic morphologically selected sperm injection (IMSI)—all of which rely heavily on microscopy—it is possible to increase the likelihood of pregnancy even when sperm motility or count is low.

The main steps of ART are illustrated in Fig. 1. The ART cycle begins with the selection of sperm collected from the patient, followed by the selection of eggs, fertilization, and embryo culture, proceeding through various diagnostic and supportive processes until the embryos are returned to the patient's body for implantation.

The diameter of an egg is approximately 0.1 mm, while that of a sperm is approximately 0.05 mm. Given that the thickness of a single human hair is generally approximately

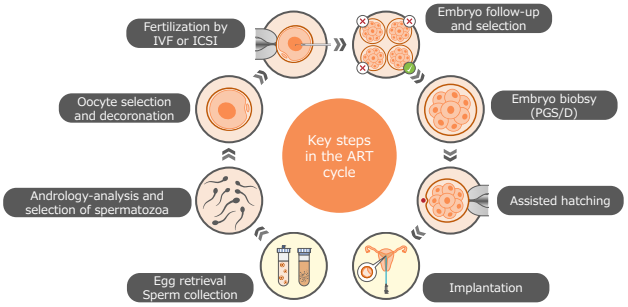

Fig. 1 ART cycle

0.05 mm to 0.1 mm, it is easy to visualize their size by considering them to be on a similar scale. In these main steps of ART, because extremely small eggs and sperm are handled, microscopes are employed in various workflows as tools to support observation.

3 Microscopes Utilized in the ART Cycle

From sperm collection and egg retrieval to fertilization and, ultimately, the selection of embryos for implantation, microscopic observation plays an extremely important role in ART. Nikon offers a full product lineup covering upright, stereo, and inverted microscopes, all of which are used in the major processes of ART. Here, the characteristics of the microscopes used are described along with the corresponding steps in the process.

3.1. Upright Microscope

In the "sperm analysis and selection" stage of the ART cycle, phase contrast observation using an upright microscope [3] is employed to determine whether the sperm are functioning properly (Fig. 2).

Fig. 2 Upright microscopes: ECLIPSE Si (left) and ECLIPSE Ci-L plus (right)

Phase contrast observation is a technique that imparts light–dark contrast to colorless and transparent specimens for visualization. It offers high detection sensitivity for thin specimens and is well-suited to observing sperm. Mean-

while, for thicker cells, the halo effect appears around their contours, making them difficult to observe; therefore, it is not suitable for observing eggs.

Evaluation parameters for sperm include motility, the numbers of motile and immotile sperm, sperm concentration, and morphology, all of which can be identified at relatively low magnification. The presence of abnormalities is considered to be associated with a reduced success rate of in-vitro fertilization.

3.2. Stereo Microscope

Equipped with independent zoom optical systems for the left and right eyes, a stereo microscope views an object from different angles on each side, producing differences (parallax) between the images perceived by the two eyes. The brain processes this parallax, enabling the perception of an object's depth and three-dimensional form. Because it allows three-dimensional observation without modifying the specimen, it is well suited for precision work. For this reason, stereo microscopes are used in "egg selection" and "embryo culture and selection" (Fig. 3). After retrieval, the eggs are examined, and those suitable for fertilization are selected. Mature eggs have a high potential for developing into normal embryos. Morphological characteristics such as egg size, morphology of the polar body, and thickness of the zona pellucida are important.

Fig. 3 Stereo microscopes: SMZ1270 (left) and SMZ800N (right)

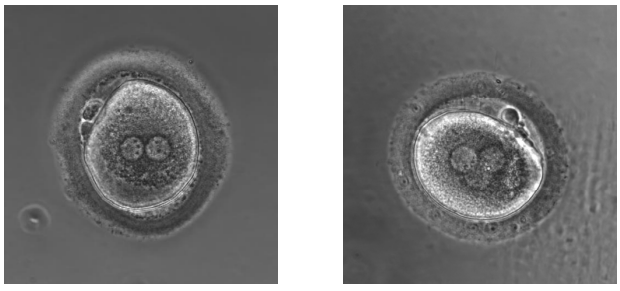

Fig. 4 Example of multinucleation: normal embryo with two pronuclei (left) and abnormal embryo with three pronuclei (right)

Image courtesy of Ronny Janssens, Centre for Reproductive Medicine, Brussels Free University, Belgium

The quality of an embryo is generally evaluated based on factors such as the number of cells at a specified time point, regularity of sizes and shapes, presence of multinucleation, and presence of vacuoles. Figure 4 shows examples of normal and abnormal embryos.

3.3. Inverted Microscope

In the ART cycle, fertilization is performed by either IVF or ICSI. Using an inverted microscope suitable for observing dish containers, ICSI, IMSI, and spindle observation are performed (Fig. 5).

Fig. 5 Inverted microscopes: ECLIPSE Ti2-I (left) and ECLIPSE Ti2-U (right)

ICSI is a method in which a sperm is injected into the cytoplasm of an egg using a manipulator and injector to achieve fertilization. The sperm is moved to the tip of the injector and injected into the egg at the focal plane. When the membrane of the egg is penetrated, a small amount of cytoplasm is aspirated and then re-injected into the egg together with the sperm (Fig. 6). In this process, a dedicated 20× or 40× objective lens is used for observation with modulation contrast [3], [4]. For example, observation can be performed using Nikon Advanced Modulation Contrast (NAMC) [5]. NAMC produces a light–dark contrast image with a three-dimensional appearance by adding shad-

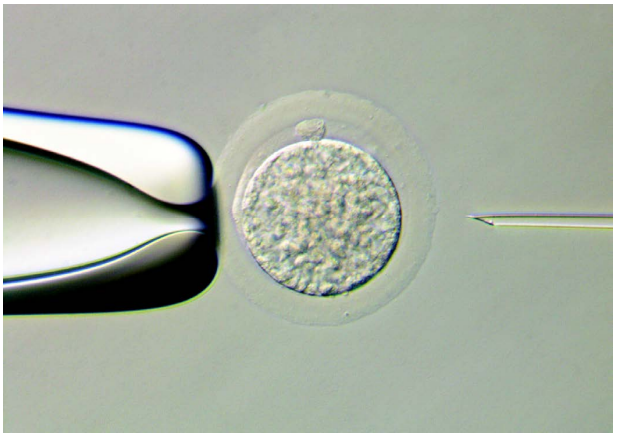

Fig. 6 Injection by ICSI

ing to colorless, transparent cells. Although the image quality is similar to that of differential interference contrast, which is described later (4.2.), it has the advantage of allowing observation even with plastic dishes.

The purpose of IMSI is to select the sperm with the highest likelihood of success in ICSI. In principle, it is the same as differential interference contrast observation [3], [6], allowing colorless and transparent cells to be visualized as three-dimensional images. Because it uses polarized light, observation cannot be performed with plastic dishes, as the polarization is disturbed. For this reason, sperm placed in a glass-bottom dish can be observed at high magnification, enabling the detection and selection of fine defects in organelles such as the sperm nucleus and vacuoles (Fig. 7). A 60× or 100× objective lens is used.

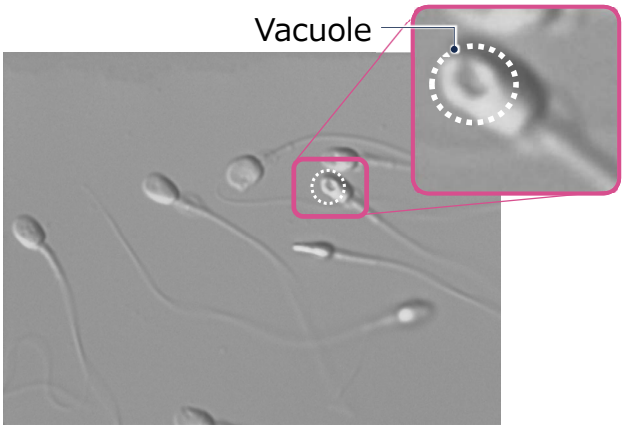

Fig. 7 IMSI with 100x objective lens
Image courtesy of Fujita Health University

The spindle plays a role in properly arranging chromosomes during cell division. Therefore, spindle observation is important for performing ICSI, as it allows determination of the spindle's position and shape within the egg. Because the spindle is a complex structure composed of microtubules, it exhibits optical anisotropy and birefringence, with refractive indices varying according to its orientation. This cannot be captured by phase contrast observation, modulation contrast observation, or differential interference contrast observation and can only be visualized using polarized light observation [6]. Furthermore, the spindle is not always present and typically appears near the first polar body of the egg (Fig. 8 (left)). In ICSI, to avoid damaging the spindle, the first polar body is positioned at the 12 or 6 o'clock orientation, and the injection is performed from the 3 o'clock direction. However, the spindle may sometimes appear away from the first polar body, making it important to confirm its location (Fig. 8 (right)).

Figure 9 shows an example configuration of an inverted

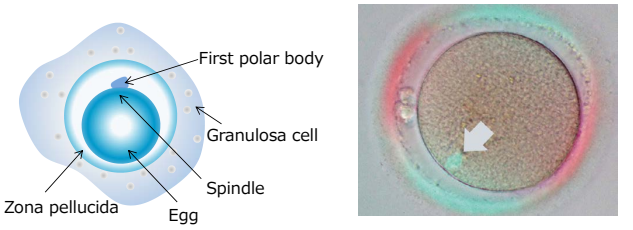

Image courtesy of: Reproduction Clinic Tokyo

Fig. 8 Schematic diagram of spindle and egg (left), example of spindle observation (right)

microscope set up inside a clean bench. In addition to the microscope, it is integrated with various equipment, including manipulators, injectors, a thermo plate for temperature control, and a laser hatching system for thinning the zona pellucida of embryos. Table 1 presents an example summarizing the objective lens magnifications on the objective revolver and corresponding tasks during operation of an inverted microscope. As summarized in Table 1, numerous microscope operations must be performed; however, because eggs experience stress once removed from the incubator, it is necessary to perform the procedures within a short period of time.

Fig. 9 Example setup of an inverted microscope

Table 1 Objective lens magnifications on the objective revolver and example tasks during operation of an inverted microscope

Objective	Example tasks
4x	Setting for injector, manipulator
10x	Oocyte selection and decoronation
20x	ICSI, Spindle observation
40x	ICSI, Spindle observation
60x or 100x	IMSI
Laser	Assisted hatching

4 Optical Principle of ICSI/IMSI and Spindle Observation

As shown in Fig. 10, the required optical components are

used in various combinations depending on the method used. This is because the properties of light used to achieve high-contrast observation of eggs and sperm differ for each method. The optical principles underlying each method are described in the following subsections.

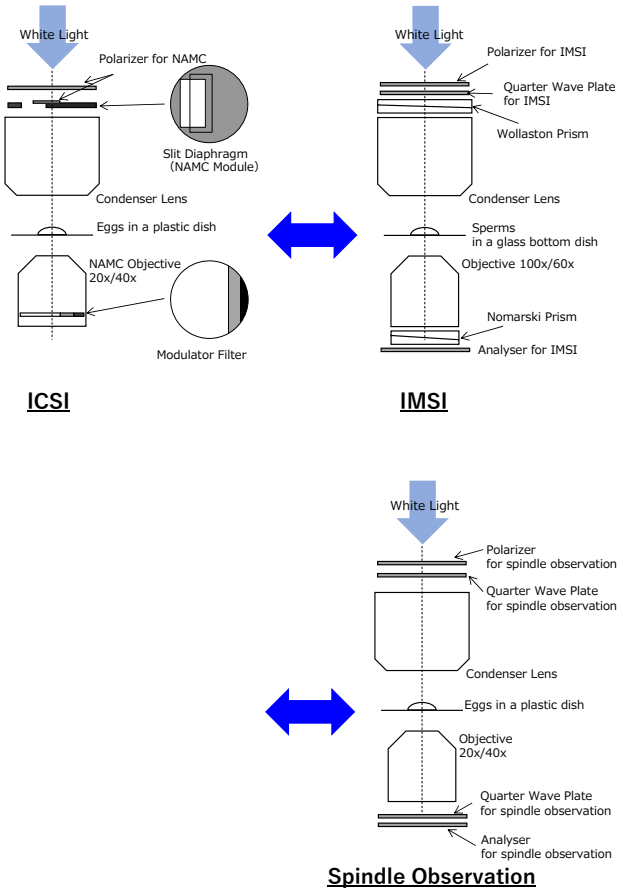

Fig. 10 Schematic diagram of the optical components required for each method

4.1. ICSI

Optically, this is a type of oblique illumination known as modulation contrast (referred to as NAMC by Nikon). The required optical components are a rotatable polarizer, slit aperture with an attached polarizer (NAMC module), and dedicated objective (NAMC objective) equipped with an internal modulation plate. The slit aperture is positioned at the front focal plane of the condenser, while the modulation plate is located at the rear focal plane of the dedicated objective (objective pupil; Fig. 11, left).

The outer edge of the slit in the NAMC module is adjusted to align with the boundary between regions a and b of the modulation plate in the NAMC objective. After passing through the NAMC module, the light rays enter the egg obliquely, are refracted, and then pass through regions a, b, and c of the modulation plate in the NAMC objective, which have different transmittances, thereby producing shading A, B, and C in the transmitted light (Fig. 11, right). Here, the transmittance of the modulation plate is 0% in region a, 100% in region c, and intermediate in region b. This shading gives the egg contrast, resulting in a three-dimensional image. By rotating the NAMC module, the orientation of the shading on the egg can be changed; however, the orientation of the modulation plate must also be aligned accordingly.

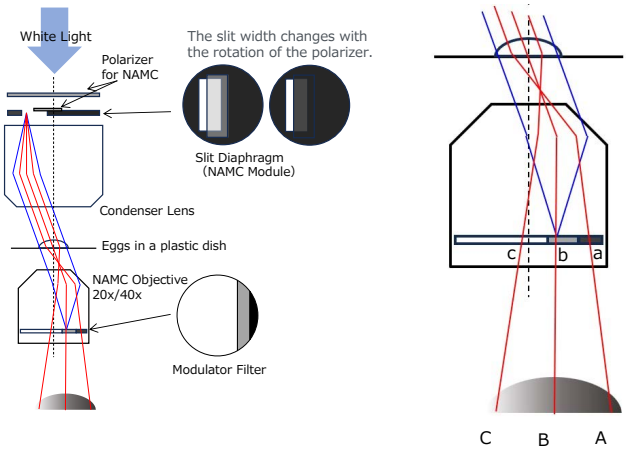

Fig. 11 Optical components and light path of NAMC (left) and reason for contrast formation (right)

By rotating the polarizer located above the condenser lens, the amount of transmitted light can be adjusted, and the slit width of the NAMC module can be changed. This changes the illumination angle of the light entering the egg obliquely, thereby allowing the contrast to be adjusted.

4.2. IMSI

Optically, this is differential interference contrast observation. On the condenser side of the optical path, a polarizer, $\lambda/4$ plate, and DIC prism are arranged in sequence, while on the objective side, a DIC prism and analyzer are positioned in that order.

As an initial adjustment step, only the polarizer and analyzer are placed in the optical path, and their transmission axes are set perpendicular to each other to achieve a crossed-Nicols condition. Subsequently, the DIC prisms corresponding to the condenser and objective lenses are inserted into the optical path (Fig. 12, left). The DIC prisms are positioned at the front focal plane of the condenser and rear focal plane of the objective lens (objective pupil). In Nikon systems, the polarizer and $\lambda/4$ plate are integrated, and the orientation of the polarizer's transmission axis is aligned with the fast axis of the $\lambda/4$ plate under the crossed-Nicols condition. Rotating the polarizer allows contrast adjustment for reasons described later.

When linearly polarized light enters the DIC prism on the condenser side, it is split into two linearly polarized beams

with orthogonal polarization directions, laterally displaced relative to each other in a direction perpendicular to the optical axis (Fig. 12, left). The lateral displacement between the two beams is called the shear amount and is designed to be smaller than the resolution of the objective lens. Figure 12 (upper right) shows the wavefronts of the two separated beams after passing through the sperm. Because a $\lambda/4$ plate is positioned on the condenser side, a retardation Δ_0 is imparted to the two beams. Figure 12 (lower right) shows the wavefronts of the two beams recombined after passing through the DIC prism on the objective side. It can be seen that retardations Δ_1 and Δ_2, corresponding to the surface profile of the sperm, are produced. From the shear amount and inclination of the sperm surface, the retardations Δ_1 and Δ_2 at each part of the sperm are determined and converted into interference colors corresponding to each retardation. This imparts shading to the sperm, thereby producing contrast. The background appears gray, corresponding to the interference color of the retardation Δ_0 produced by the $\lambda/4$ plate. By rotating the polarizer, the retardation Δ_0 can be finely adjusted, allowing the contrast to be varied.

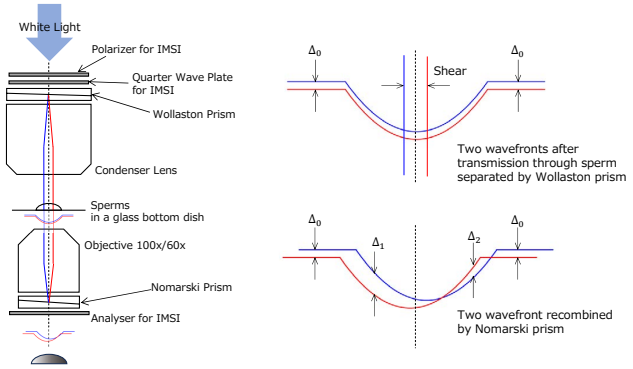

Fig. 12 Optical components and light path of DIC (left) and reason for contrast formation (right)

Because polarization must be maintained when light enters the DIC prism, observation cannot be performed using plastic containers. In addition, contrast can only be detected in the direction in which the shear is produced.

4.3. Spindle Observation

Optically, this observation is performed with polarized light, and Nikon employs circular polarization. The spindle, which exhibits optical anisotropy, is visualized with added coloration.

An optical element integrating a polarizer and $\lambda/4$ plate is placed on both the condenser side and objective side. The angle between the transmission axis of the polarizer and fast axis of the $\lambda/4$ plate is set to 45 degrees, producing circularly polarized illumination for the egg. After passing through the egg, the circularly polarized light is converted back into linearly polarized light by the $\lambda/4$ plate and polarizer on the objective side. At this point, the transmission axis of the polarizer is orthogonal to the linear polarization (Fig. 13, left).

Although the spindle can be observed with linear polarization, illumination with circular polarization offers the advantage of rendering the spindle in color (red or blue). The reason it appears red or blue is that the $\lambda/4$ plate does not function perfectly over the entire wavelength range of white light. In general, a $\lambda/4$ plate provides a retardation of one quarter of the wavelength at its reference wavelength (green in this case). However, at red and blue wavelengths, which deviate from the reference, the retardation differs from one quarter of the wavelength. As a result, at red and blue wavelengths, the light becomes elliptically polarized after passing through the $\lambda/4$ plate on the condenser side, and even after passing through the $\lambda/4$ plate on the objective side, it does not revert to perfectly linear polarization. Therefore, the light enters the final polarizer as elliptically polarized light, resulting in the residual presence of red and blue light (Fig. 13, right). In addition, by rotating the optical element on the condenser side, the major and minor axes of the elliptical polarization are interchanged, thereby changing the intensity of the red and blue light passing through the polarizer on the objective side and enabling adjustment of the coloration.

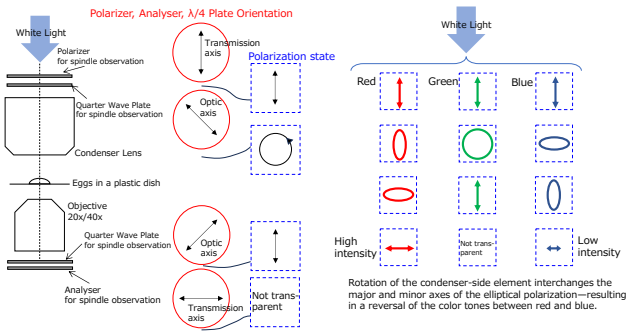

Fig. 13 Optical components and light path for spindle observation (left) and reason for red/blue coloration (right)

The use of circular polarization allows the spindle to be observed in red or blue, making it easier to locate even when the egg is rotated in the XY plane. With linear polarization, however, the spindle may appear white or black, or become invisible depending on the rotation of the egg, making it more time-consuming to locate and increasing the risk of overlooking it.

Because polarization must be maintained between the polarizer and $\lambda/4$ plate optical elements, observation cannot

be performed with plastic containers.

Table 2 summarizes the image characteristics, resolution, contrast, and applicable containers for each method described above.

Table 2 Optical characteristics of ICSI/IMSI and spindle observation

	ICSI	IMSI	Spindel observation
Microscopy	Modulation contrast (NAMC)	Differential interference contrast	Polarized light
Characteristics	Shading: 3D effect, direction adjustable	Shading: 3D effect	Birefringence: visible
Resolution	High (lower than DIC due to the slit diaphragm)	High	High
Contrast	High	High	High (Birefringence)
Contrast adjustment	Polarizer: rotation	Polarizer: rotation	N/A
Suitable sample	Sperm, Egg, Embryo	Sperm	Egg
Dish	Glass-bottom/Plastic	Glass-bottom (Plastic: not allowed)	Glass-bottom (Plastic: not allowed)

5 Conclusion

In Japan, where the declining birthrate is advancing, ART plays an important role. ART is a medical technology encompassing various processes, such as IVF and ICSI, that involve handling eggs and sperm to treat infertility and support pregnancy. Upright, stereo, and inverted microscopes essential to the ART cycle, along with their associated optical technologies, have been introduced. In particular, for ICSI/IMSI, which require precise manipulation with an inverted microscope, optical techniques such as modulation contrast (NAMC) and differential interference contrast are employed. In spindle observation, circular polarization is used to determine the spindle's position within the egg, and avoiding it during injection contributes to improved fertilization rates. We will continue to work toward advancing technological innovation in the medical field and provide new solutions to help address the societal issue of declining birthrates.

References

[1] Ministry of Health, Labour and Welfare, "VITAL STATISTICS OF JAPAN 2019," 2019. [Online]. Available: https://www.mhlw.go.jp/english/database/db-hw/dl/81-1a2en.pdf

[2] Nikon Instruments Inc. ECLIPS Ti2-I Product page. [Online]. Available: https://www.microscope.healthcare.nikon.com/products/inverted-microscopes/eclipse-ti2-i

[3] S. Bradbury and P. Evennett, *Contrast Techniques in Light Microscopy*, Oxford: Oxford University Press, 1996.

[4] R. Hoffman and L. Gross, "Modulation Contrast Microscope," *Applied Optics*, vol. 14, no. 5, pp. 1169–1176, 1975.

[5] K. Matsui, "Modulation Contrast Microscope," U.S. Patent 8 599 479, Dec. 3, 2013.

[6] P. C. Robinson and S. Bradbury, *Qualitative Polarized Light Microscopy*, Oxford: Oxford University Press, 1992.

三宅範夫 Norio MIYAKE
光学本部 第一設計部
1st Designing Department
Optical Engineering

三宅範夫
Norio MIYAKE

NIKKOR Z 28–135mm f/4 PZの開発

長岡弘仁，栗林知憲，高橋伸明

Development of the ‘NIKKOR Z 28–135mm f/4 PZ’

Koji NAGAOKA, Tomonori KURIBAYASHI and Nobuaki TAKAHASHI

2025年４月，「NIKKOR Z 28–135mm f/4 PZ」を発売した．ニコンの光学性能を継承しつつ動画パフォーマンスに特化したレンズであり，様々な映像制作のワンマン・オペレーション撮影においてビデオグラファーの快適な操作性を追求している．この提供価値のために詰め込んだ最新の要素技術を，ここに説明する．

The NIKKOR Z 28–135mm f/4 PZ was launched in April 2025. This lens inherits the optical performance of Nikon and is also specialized for video performance. It offers comfortable operability for videographers in one-man shootings for various video productions. In this paper, the latest elemental technologies packed into this lens are explained to elucidate its value.

Key words ニコン Z マウント，交換レンズ，パワーズーム，動画撮影
Nikon Z mount, interchangeable lens, power zoom, video shooting

1 Introduction

In April 2025, Nikon released the standard zoom lens “NIKKOR Z 28–135mm f/4 PZ” compatible with the Nikon Z mount system (Fig. 1).

Fig. 1　NIKKOR Z 28–135mm f/4 PZ

2 Background to the Development of a Standard Power Zoom Lens for Video Shooting

Nikon offers interchangeable lenses designed for video shooting; however, if asked whether they have been widely used as full-fledged video lenses, the answer would be “No.” Based on this understanding, we investigated the challenges encountered in video shooting and the needs of users. Further, we defined the product concept of this model as “a power zoom lens that, as a professional video production tool, can be used with confidence for event coverage, reporting, and live streaming.”

Building on this, we first clarified the extent to which existing NIKKOR Z lenses match the aforementioned concept and where their shortcomings lay. Then, we examined what Nikon, as a late entrant into the video industry, should and could offer.

As a result, we undertook the development with the following considerations in mind: a power zoom that, in one-person shooting, allows the lens to perform smooth zooming so the operator can concentrate on other shooting tasks; the construction of a shooting system optimal for event coverage, reporting, and live streaming—areas not fully addressed by existing lenses; and an optical design anticipating the era when 8K becomes the mainstream.

3 Operability and Functions that Support Videographers

3.1. “Easy-to-Use” Focal Length Range and Controls

In one-person shooting environments, the equipment selected is chosen with a strong emphasis on production efficiency due to the limited number of shooting staff. In addition, one-take documentary shooting or wedding filming should be possible without mistakes, even from a long distance. To accommodate a wide variety of event coverage,

achieving an extremely high zoom ratio from wide-angle to telephoto would be ideal; however, as with broadcast television lenses, this would result in an extremely large optical system, far removed from ease of use. Therefore, we investigated concrete anticipated use cases—such as the size of the subject to be captured and shooting distance—and determined a focal length range of 28–135 mm, which is compatible with a practical overall size (Fig. 2).

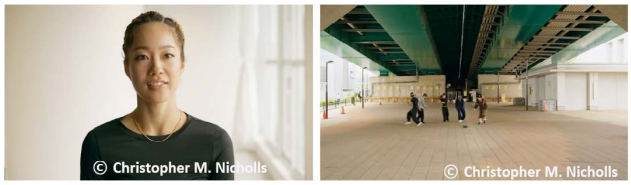

Fig. 2 Versatile focal length range: 28–135 mm

3.2. Power Zoom Capable of Ease-In and Ease-Out

The zoom lever allows for "ease-in/ease-out" of operation, in which the zooming speed is gradually varied at the start and end of zooming (Fig. 3). This enables smooth and natural-looking zoom-in and zoom-out transitions. This ease-in/ease-out of operation is achieved by imparting the zoom lever a suitable resistance and finely tuning the relationship between the operating stroke and zooming speed.

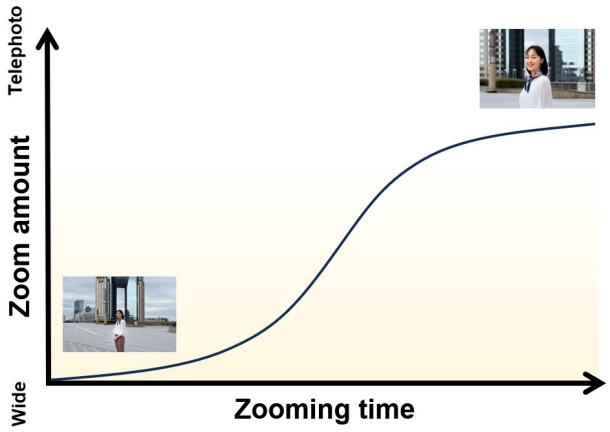

Fig. 3 Ease-in & ease-out

3.3. Internal Zoom Mechanism that Suppresses Shift in Center of Gravity

In general, standard zoom lenses often employ a variable overall length design in which the foremost lens group is extended, from the standpoint of reducing the size. In a variable overall length type, the foremost group also tends to have a large lens diameter, resulting in a substantial shift in the center of gravity when zooming from wide-angle to telephoto. A large shift in the center of gravity causes the balance to be disrupted when the camera is tripod-mounted or used on a gimbal, introducing unintended motion into the footage and making it visually unappealing. By adopting an internal zoom mechanism with the front group fixed, this model suppresses the shift in the center of gravity during zooming to approximately 2 mm. When mounted on the Z9, the shift in the center of gravity is further reduced to approximately 1 mm (Fig. 4). Furthermore, even when using a gimbal, there is no concern about balance being disrupted by a shift in the center of gravity, allowing comfortable zoom operation (Fig. 5).

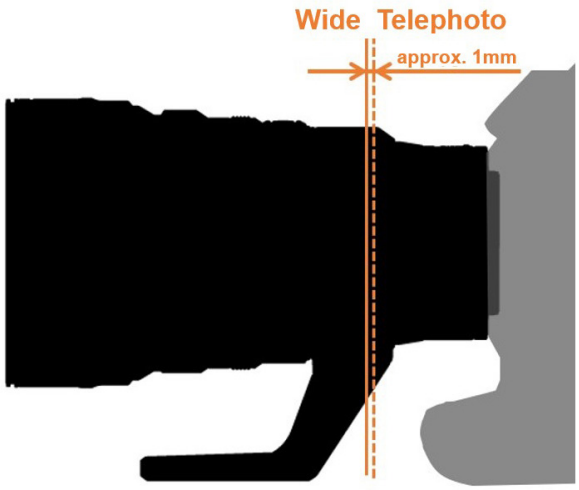

Fig. 4 Minimal shift in center of gravity

Fig. 5 Shooting with a gimbal

4 Accessories for Video Shooting and Remote Shooting System

4.1. Compatibility with Matte Boxes and Follow Focus Systems

The front-end diameter of the lens barrel is ϕ104 mm, accommodating diameter compatibility with multiple matte boxes. In addition, anticipating the use of a follow focus system for more precise and finer manual focusing, a gear profile compatible with gear module 0.8 has been incorporated into the operation ring. This is expected to provide high convenience in situations such as documentary shooting, where precise focus adjustment in accordance with

subject movement is required.

4.2. Square Lens Hood with Filter Adjustment Window

While lens hoods for still photography are often petal shaped, the hood supplied with this product adopts a square shape familiar in the video shooting industry (Fig. 6). In addition, by incorporating a filter adjustment window, it is possible to operate a circular polarizing filter or variable ND filter while the hood is attached, eliminating the need to remove and reattach the hood. The hood is designed to be attachable facing either up or down, allowing the position of the adjustment window to be selected according to the equipment setup.

Fig. 6 Square lens hood with filter adjustment window

4.3. Support for Remote Zoom Operation

The incorporation of a power zoom enables remote zoom operation from devices such as computers and smartphones. Applications tailored to each device are available: NX Tether for computers and SnapBridge or NX Field for smartphones and tablets. Remote operation, unlike manual operation, eliminates the risk of inadvertently moving the equipment and disturbing the composition, making it useful for situations such as interviews, where maintaining a fixed composition is important. One-person operations are also possible in setups utilizing multiple cameras.

5 Optical Performance Enabling Ultra-High-Definition 8K Resolution

5.1. Optical Performance Objectives Considering Video Viewing Environments

In recent years, the number of camera bodies capable of 8K recording has been increasing, and an infrastructure for 8K editing has also been progressively established. In addition, as there are use cases in which footage is recorded in 8K, cropped in post-production, and output in 4K without digital interpolation, it was necessary to consider optical performance with an eye towards a future era in which 8K recording becomes mainstream. Building upon the optical performance targeted by conventional NIKKOR Z lenses, this model redefined the required number of resolvable lines based on 8K monitor viewing environments and human visual characteristics, thereby determining the target optical performance from key shooting scenarios in event coverage and reporting applications. Furthermore, in video shooting, unintended and unnatural "movements" must not appear in the footage, making it necessary to suppress abrupt changes in aberrations across the zoom range. Specifically, these include spherical aberration, which determines the overall image contrast; coma and field curvature, which determine resolution in the peripheral areas of the image; and chromatic aberrations, such as color fringing in out-of-focus areas and purple fringing in high-luminance regions. By suppressing these aberrations and minimizing their variation across the zoom range, high-quality imaging performance has been achieved throughout the entire zoom range.

5.2. Optical Performance Enabling High-Quality Video Shooting

This model adopts a zoom type with a positive-lead structure. In a positive-lead structure, the front group converges the light, allowing the subsequent groups to have smaller diameters, which contributes to overall size reduction. This model was designed with a focus on driving the zoom group without relying on an external power source, leading to the adoption of the positive-lead structure, which is advantageous for reducing the weight of the zoom group.

A positive-lead structure standard zoom lens generally has a three-group structure of positive–negative–positive, with the second negative group serving as the main variator group and the third positive group functioning as the master lens.

In general, many standard zoom lenses have the first positive group extend during zooming; this is because varying the spacing between the first positive and second negative group significantly enables the change in angle of view during zooming while keeping the incident angle of light into the third positive master lens group as constant as possible, thereby making it easier to suppress changes in aberrations across focal lengths. This model can also be broadly divided into three groups—positive, negative, and positive—but differs from the aforementioned standard zooms in that it is of the fixed overall length type. Unlike the variable overall length type, the fixed overall length type has inherent factors

that increase size: ① the overall product length becomes longer, and ② the front element diameter becomes larger. The first factor exists because, in a variable overall length type, the telephoto end—i.e., the state with the greatest optical length—becomes the product length in a fixed overall length type. The second factor exists because, as a consequence of the first, the optical length at the wide-angle end inevitably becomes longer, requiring a larger front element diameter to maintain peripheral illumination.

In addition, because the front positive group cannot be moved for zooming, the burden on the subsequent negative group increases, resulting in a stronger power (optical refractive power). Because the power of the negative group corresponds to the amount of movement required for zooming, an excessively strong power reduces the required movement but imposes stricter demands on the group's driving precision while also increasing the amount of aberration variation across the zoom range. Conversely, if the power is too low, the required movement increases, extending the optical length and resulting in a larger product size. To achieve both high driving precision and suppression of aberrations, it is necessary to set an appropriate power. To reduce the burden on the negative group, the third-group master lens is separated, with part of it assigned the role of the variator group. In addition, by appropriately arranging Extra-low Dispersion (ED) lenses and aspherical lenses and taking advantage of the large-diameter Z mount, which allows large-diameter lenses to be positioned near the mount opening, the design contributes to improved contrast all the way to the edges of the image. Accordingly, an appropriate distribution of power among the groups, combined with specialized optical elements, balances optical length, aberration variation, and driving precision. Moreover, rather than relying solely on the design to achieve the desired optical performance, every unit undergoes inspection and adjustment during mass production to ensure that the optical performance targeted in the design is realized.

6 Development of Elemental Technologies Supporting Comfortable Power Zoom

6.1. Adoption of a Coupling Mechanism

This model also incorporates measures to address vibration and noise during operation. In existing NIKKOR Z lenses already on the market, the autofocus mechanism is designed with a silent structure; however, in the zoom mechanism of this product, the lens groups must be driven at even higher speeds and over longer strokes, necessitating more effective noise reduction measures than those in previous products. To address this, a coupling (shaft coupling) was adopted at the connection between the actuator—which tends to be a source of vibration—and the lead screw for driving the lens group, positioned in close proximity to the actuator, thereby absorbing even slight misalignments between the actuator shaft and lead screw and achieving quiet operation.

6.2. Highly Efficient Lens Drive System

The zoom group is often heavier than the focus group, and this model was no exception. Although increasing the actuator's driving force would make operation possible, it would come at the cost of increased noise; therefore, it was necessary to drive the heavy lens while keeping the driving force at the same level as in previous models. Therefore, the conventional drive efficiency was reconsidered from the ground up, with a focus on reducing friction during lens drive operation. From this perspective, multiple design solutions were proposed and repeatedly compared and evaluated, ultimately resulting in a configuration in which ball bearings are placed at numerous sliding interfaces. Compared with the conventional sliding-friction-based structure, to date, adopting a rolling-friction-based structure has enabled an exceptionally high drive efficiency among interchangeable lenses.

6.3. Control Tuning

In addition to mechanical refinements, careful consideration has also been given to the control method of the actuator. The acceleration and deceleration at the start and stop of driving have been tuned to achieve smooth operation while maintaining a balanced trade-off with drive response.

6.4. Thermal Design

As the multiple actuators used in this model tend to become sources of heat, consideration has also been given to the heat dissipation structure.

The fundamental design concept involves reducing the power consumption of heat sources, ensuring thermal conduction paths around heat sources, and distributing the placement of heat sources. Although the power required to drive the lens groups was optimized from the initial design stage, desk calculations predicted a significant temperature rise. Therefore, a design layout was adopted in which multiple actuators are distributed, and graphite sheets were utilized to connect the actuators to internal metal components, thereby securing efficient heat dissipation paths while also

taking assembly workability and product size into consideration. Finally, thermal simulations were conducted, confirming that even under demanding conditions, such as prolonged continuous zooming, effective heat dissipation is achieved without heat concentrating in specific areas (Fig. 7).

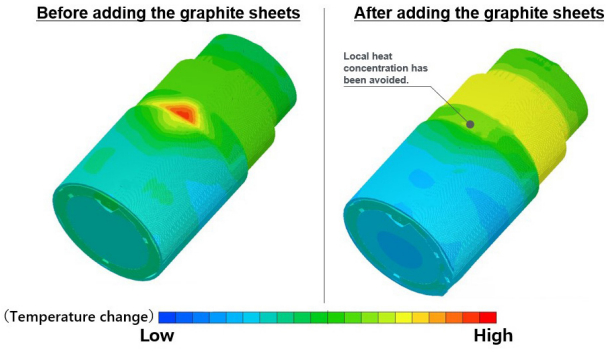

Fig. 7 Thermal dissipation simulation

7 High Mobility Achieved through Weight Reduction and Optical Specifications

7.1. Refining the Specifications through Trial and Error

When designing a lens with user mobility in mind, constraints on weight inevitably arise. For example, attempting to increase the zoom ratio beyond that of this model would, as shown in the translucent area of Fig. 8, enlarge both the maximum diameter and overall product length, thereby impairing handheld usability. In this lens, as mentioned above, we investigated the focal lengths in highest demand and repeatedly examined those that offer a good balance with mass, ultimately adopting the specifications of 28–135 mm and f/4.

Fig. 8 Specification optimization process

In addition, at the minimum shooting distance, it is possible to get close to the subject—0.34 m on the wide-angle side (reproduction ratio of 0.15 ×) and 0.57 m on the telephoto side (reproduction ratio of 0.25 ×)—making it possible to capture most scenes with this single lens without the need for lens changes, and, through the synergistic effect with weight reduction, resulting in a highly mobile lens.

7.2. Largest Number of Aspherical Lenses in the History of NIKKOR Z Lenses

For this lens, to drive the zoom group without relying on an external power supply, it was essential to reduce the weight of the moving group. To cover the wide angle-of-view range from 28 to 135 mm, the general optical design principle is to increase the number of lenses so that light is gradually refracted, thereby minimizing aberrations; however, in the case of this lens, this approach resulted in the zoom group becoming excessively heavy and thus impossible to drive. To address this, we employed a total of five aspherical lenses—four conventional and one ED aspherical lens produced by applying aspherical processing to an ED lens—thereby assigning to these few aspherical lenses the corrective functions that would otherwise require a considerably larger number of spherical lenses, achieving both aberration correction and group weight reduction (Fig. 9). As of April 2025, this lens uses the largest number of aspherical lenses in the history of NIKKOR Z lenses. The surface accuracy of aspherical lenses requires processing technologies at the submicron to nanometer level, as well as stable production. Although the design team has investigated shapes that balance aberration correction and manufacturability, the expertise of the engineering and manufacturing teams is indispensable for realizing them. Through close interdepartmental collaboration from the design stage onwards, we successfully adopted five high-precision aspherical lenses, making a significant contribution to weight reduction.

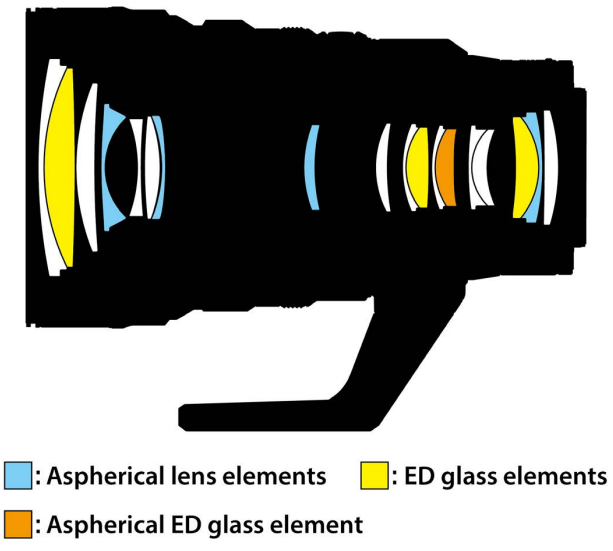

Fig. 9 Lens configuration diagram

7.3. Weight Reduction while Ensuring Reliability

While ensuring reliability in terms of strength and durability, we thoroughly pursued weight reduction by examining the thinning of metal parts and reducing the number of components.

In recent years, our in-house strength simulation technology has also improved, enabling efficient assurance of component strength and structural design, which has greatly contributed to weight reduction. As a result, the lens achieved a mass of 1,210 g while incorporating a tripod collar.

8 Hi-Res Zoom Extending the Telephoto Range

8.1. Hi-Res Zoom

In October 2022, the hi-res zoom function was added in firmware C:Ver.3.00 for the Z9. Even with a prime lens, it allows zooming up to 2 × without any degradation in image quality. Since its release on the Z9, this function has been deployed to multiple products, continuing to steadily evolve with features such as speed adjustment and power/hi-res zoom collab, and can be fully experienced with this lens as well.

8.2. Support for Power/Hi-Res Zoom Collab

Because the power zoom is electronically controlled, both power zoom and hi-res zoom can be operated during shooting with the manipulation of a single control. When linked, the focal length becomes twice as long (equivalent to 270 mm when shooting 4K video with the Z9/Z8). Furthermore, selecting the DX (APS-C) image area makes it possible to extend the magnification by an additional 1.5 × (equivalent to 405 mm in full-frame terms), although when the image size is set to DX, the resolution is limited to FHD.

8.3. Extended Mode and Synchronized Mode

Power/hi-res zoom collab can be selected from two modes. The extended mode performs hi-res zooming in the range beyond the focal length of the optical zoom, while the synchronized mode performs optical zoom and hi-res zoom simultaneously (Fig. 10). The extended mode is characterized by natural changes in perspective and depth of field within the optical zoom range according to the focal length while the telephoto-side state is maintained as is in the hi-res zoom range. The synchronized mode enables uninterrupted zooming without pauses in the zooming operation, allowing smooth zooming and is considered effective when actively zooming over a wide focal length range during video recording. Each mode can be selected according to its intended application.

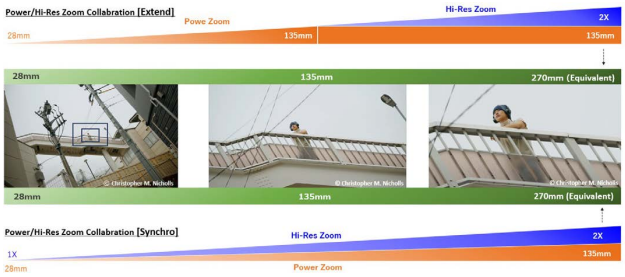

Fig. 10 Hi-res zoom collab

It should be noted that this function was made possible precisely because both the camera body and lens were developed in-house.

9 Excellent Backlight Resistance

9.1. Meso Amorphous Coat and Optimized Lens Shapes

This lens achieves excellent backlight resistance through optical and mechanical innovations, enabling the capture of clear, high-contrast images even in scenes with strong light sources. From an optical perspective, backlight resistance is controlled through appropriate lens shapes, arrangements, and coats. Because each lens element contributes to aberration correction but also becomes a potential surface for ghost generation, we have repeatedly conducted ray-tracing simulations to determine optimal lens shapes that prevent prominent ghosts from being focused on the image plane while still meeting the targeted optical performance. Another measure is to apply an extremely low-reflectance coat to the lens, thereby reducing the intensity of the light rays that cause ghosts. This lens employs the Meso Amorphous Coat, which offers the highest anti-reflective performance in the history of NIKKOR lenses. The Meso Amorphous Coat is formed by depositing a structure composed of particles with minute amorphous structures interconnected with each other onto an underlying coat, thereby creating particle gaps—called mesopores—throughout the entire film (Fig. 11). The presence of air within these numerous mesopores results in a film structure with a low refractive index and low

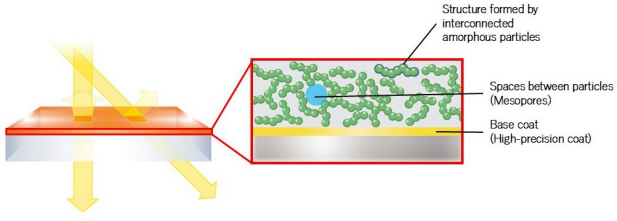

Fig. 11 Structure of the meso amorphous coat

scattering properties [1].

With a thorough understanding of the characteristics of the Meso Amorphous Coat and Super Integrated Coat, this lens achieves both high optical performance and excellent backlight resistance by arranging the lenses in optimal shapes and applying the most suitable coat to the appropriate locations.

9.2. Measures in Structural Components

In this lens, the space required to accommodate the zoom drive actuators has resulted in complex internal component shapes, making it extremely challenging to implement measures to reduce internal reflections while also taking manufacturing constraints into consideration. By repeatedly conducting ray-tracing simulations and effectively incorporating anti-reflective geometries and low-reflectance surface treatments, we have achieved a high level of backlight resistance.

10 Operability without Visual Cues

10.1. Knurled Patterns and Diameter Differences of the Operating Rings

From the front end of the lens barrel, the focus, zoom, and control rings are arranged in the order of assumed frequency of use (Fig. 12). The focus ring features a moderately contoured finger grip to enhance the sense of hold. The zoom ring has a special knurled pattern and is designed with a diameter difference from the focus ring. These features allow the two most frequently used rings to be distinguished and operated naturally using a fingertip. The control ring employs the common diamond knurling used in NIKKOR Z lenses, with its shape designed to be easily distinguishable by touch from the other rings.

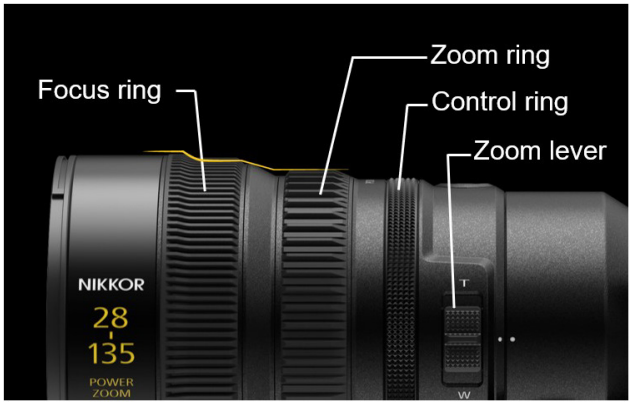

Fig. 12 Operability without relying on visual cues

10.2. Placement and Design Features of the Zoom Lever

The zoom lever is positioned on the side of the lens barrel for ease of use from waist to shoulder level, accommodating both vertical and horizontal shooting orientations (Fig. 12). The lever's protrusion is made relatively tall for a secure catch, and diamond knurling is applied near the protrusion, also serving as a non-slip surface to support precise ease-in/ease-out operations.

11 Conclusion

The NIKKOR Z 28–135mm f/4 PZ is, we believe, a lens that combines hi-res imaging, a shooting system, operability, and mobility suitable for professional video production. We hope that users will be able to concentrate on shooting with confidence and expand the possibilities for one-person operations in client work.

We will continue to develop products that exceed customer expectations, thereby contributing to the further evolution of the Nikon Z mount system and the advancement of imaging culture.

References

[1] R. Suzuki, "Fabrication of a porous SiO_2 thin film with an ultralow refractive index for anti-reflective coatings," *Journal of Sol-Gel Science and Technology*, vol. 106, no. 3, pp. 860–868, 2023.

長岡弘仁　Koji NAGAOKA
光学本部 第二開発部
2nd Development Department
Optical Engineering

栗林知憲　Tomonori KURIBAYASHI
光学本部 第三設計部
3rd Designing Department
Optical Engineering

高橋伸明　Nobuaki TAKAHASHI
光学本部 第二開発部
2nd Development Department
Optical Engineering

長岡弘仁
Koji NAGAOKA

栗林知憲
Tomonori KURIBAYASHI

高橋伸明
Nobuaki TAKAHASHI

ADAS/AD に向けた革新的な車載カメラシステム「Tele & Wide 同一光軸カメラ」の開発

金岡浩史，倉茂孝道，髙梨祐介，目黒明彦，築山大亮，和湯瑞葵

Innovative In-vehicle Camera System for ADAS/AD: Single-Lens System Integrating Telephoto and Wide-Angle Functions

Hiroshi KANAOKA, Takamichi KURASHIGE, Yusuke TAKANASHI,
Akihiko MEGURO, Daisuke TSUKIYAMA and Mizuki WAYU

自動車業界における先進運転支援システムや自動運転技術は日々進化している．また，ドライバーが標識や歩行者等を視認できないことで発生する重大事故を防止するため，視認性を向上させる手段へのニーズが高まっている．

ニコンと三菱ふそうトラック・バス株式会社は，未来のトラックやバスに新たな価値を創出することを目指し，2020年から共創活動を行ってきた．その成果として，望遠レンズと広角レンズを一体化し，遠方と周辺を確認することが可能となる革新的なカメラシステムを確立した．

この革新的なカメラは望遠レンズと広角レンズの一体化を実現し，遠方と周辺を同時に撮影することが可能である．遠方と周辺の光軸が同一のために視差が生じないことから車両周辺の情報を画像認識する際に，遠方で認識した標識や他車をトラッキングしても，対象を見失ったり二重に認識したりする問題を減らすことができる．また，効果的に車両に配置することによりカメラ台数を抑えながら全周囲360°を途切れなく見ることができ，従来の課題であったシステムコストや故障率などの低減が期待できる．

In the automotive industry, advanced driver-assistance systems (ADAS) and autonomous driving technology (AD) are evolving every day. Moreover, a growing demand exists for methods that enhance visibility to prevent serious driver-accidents related to unnoticed signs/pedestrians. Nikon and Mitsubishi Fuso have developed an innovative in-vehicle camera system to create new safety value for future trucks and buses.

The initiative resulted in the development of an innovative camera featuring a single-lens system integrating telephoto and wide-angle functions to facilitate both long-distance and peripheral visibility.

The optical axes of the far-away and periphery shots are the same, which prevents parallax. Therefore, the camera system reduces the risk of losing track of an object or detecting a double image when used as an in-vehicle camera with AI image recognition to collect road information with tracking signs or other vehicles in the distance.

Using this system requires fewer cameras to be installed in the vehicle owing to its effective positioning and integrated telephoto and wide-angle lens system. This innovation facilitates uninterrupted 360° coverage and addresses common challenges such as high system costs and failure rates.

Key words 車載カメラ，先進運転支援システム，自動運転，望遠，広角，同一光軸
in-vehicle camera, advanced driver-assistance systems, autonomous driving, telephoto, wide-angle, coaxial

1 Introduction

In the automotive industry, advanced driver-assistance systems (ADAS) and autonomous driving technology (AD) are evolving every day. Moreover, a growing demand exists for methods that enhance visibility to prevent serious driver-accidents related to unnoticed signs/pedestrians.

Nikon and Mitsubishi Fuso have developed an innovative in-vehicle camera system to create new safety value for future trucks and buses. The initiative resulted in the development of an innovative camera featuring a single-lens system integrating telephoto and wide-angle functions to facilitate both long-distance and peripheral visibility (Fig. 1).

The optical axes of the far-away and periphery shots are

Fig. 1 Tele & Wide coaxial camera integrating telephoto and wide-angle lenses

the same, which prevents parallax. Therefore, the camera system reduces the risk of losing track of an object or detecting a double image when used as an in-vehicle camera with AI image recognition to collect road information with tracking signs or other vehicles in the distance (Fig. 2). Using this system requires fewer cameras to be installed in the vehicle owing to its effective positioning and integrated telephoto and wide-angle lens system. This innovation facilitates uninterrupted 360° coverage and addresses common challenges such as high system costs and failure rates.

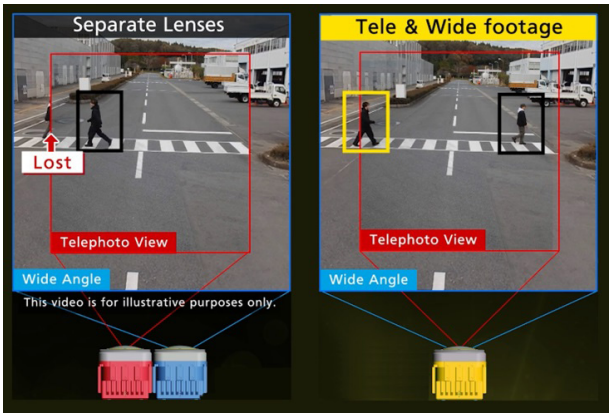

Fig. 2 Comparison between separated telephoto and wide-angle lenses (left) and coaxial configuration (right)
(coaxial configuration is free from parallax effects)

2 Tele & Wide Coaxial Camera

The wide-angle lens is designed with a FOV of 190° and the telephoto lens with a FOV of 20°. The light from each lens enters from the object side, passes through a common lens group, and is then split into separate optical paths by a beam splitter. The reflected and transmitted light from the beam splitter passes through subsequent lens groups and is then focused onto the image sensors (Fig. 3). This configuration enables the acquisition of parallax-free images for both the wide-angle and telephoto views. In addition, considering factors such as downsizing the housing and manufacturability of the lenses, the reflected path is assigned to the wide-angle lens and the transmitted path to the telephoto lens.

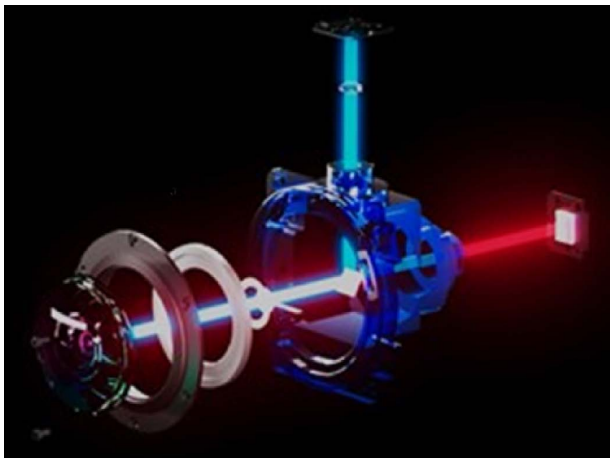

Fig. 3 Configuration of the Tele & Wide coaxial camera

Considering in-vehicle applications, the optical design was advanced with careful consideration of the following six points:

1) Projection Characteristics of the Fisheye Lens

As mentioned above, the wide-angle lens of this camera is a fisheye lens with a FOV of 190°. A fisheye lens can be designed to alter its projection characteristics, allowing it to enlarge the central area of the image while compressing the periphery, or achieve the opposite characteristics. Because this camera is configured to enlarge the central area of the image with the telephoto lens, it is desirable for the wide-angle lens to provide higher resolution in the peripheral areas than in the center. Based on this concept, the wide-angle lens was designed with projection characteristics that enhance resolution in the peripheral areas of the image.

2) Resolution Performance

To enable object detection across the entire image, the optical design ensures high resolution not only in the center but also in the peripheral areas. In particular, because it is necessary to satisfy the performance requirements of both the wide-angle and telephoto lenses, the common lens group located before the beam splitter was designed with an optimal lens power that balances the wide-angle and telephoto performance. Considering maintainability, the design has been implemented to make the front lens replaceable, while suppressing resolution degradation caused by mounting errors.

3) Optimal Sensor Placement

This camera is intended for installation outside the vehicle, where dust, dirt, water droplets, and similar contaminants are likely to adhere to the front surface of the lens. If the sensor is positioned to focus on nearby objects, any adhering contaminants become more conspicuous, whereas positioning the sensor to focus on distant objects reduces detection accuracy for nearby objects.

Based on these considerations, the sensors are positioned at locations optimized for the intended use cases.

4) Robustness to Temperature Variations

When the environmental temperature is high or low, focus shift may occur, resulting in image quality degradation. This camera employs a robust design that minimizes image quality degradation in high- and low-temperature environments by selecting materials and shapes for optical and mechanical components with consideration of their thermal deformation characteristics.

5) Ghost and Flare

We took measures to minimize the occurrence of ghosting and flare, which can be detrimental to object detection. In particular, because a fisheye lens has a wide FOV and is susceptible to strong light entering from various sources, we conducted ray-tracing simulations to examine the optimal shapes of optical and mechanical components and determine their placement.

6) Telephoto Lens Customization Capability

On the wide-angle side, an FOV exceeding 180° is required to detect surrounding objects, whereas on the telephoto side, the required FOV varies depending on the use case. To address this, the camera is designed such that the wide-angle configuration remains unchanged, while customization is enabled by replacing the entire set of lenses on the sensor side of the beam splitter for the telephoto path. This enables the FOV on the telephoto side to be changed at low cost, and we have actually conducted development and evaluation using multiple types of telephoto lenses.

Based on these six points, we have achieved an optical design optimized for in-vehicle cameras.

It is difficult to imagine how the images will appear when the camera is mounted on a vehicle without actually seeing them. By conducting real-image simulations of the camera mounted on a vehicle from the initial design stage, we examined optimal camera specifications suited to the intended use cases. In addition, real-image simulations make it possible to conduct various verifications without producing prototypes (Fig. 4).

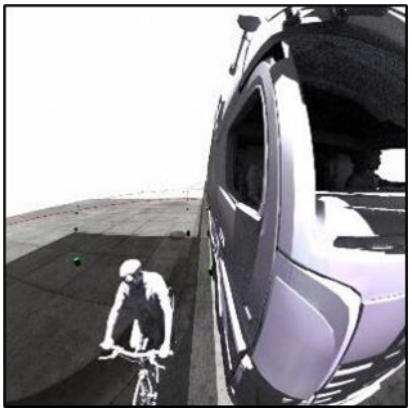

Fig. 4 Image obtained from real-world simulation

Using the developed camera, we conducted a comparative evaluation by photographing a STOP sign placed 150m away with both the wide-angle and telephoto lenses. When the sign portion of the image captured with the wide-angle lens was digitally zoomed in, the letters “STOP” appeared blurred and unreadable; however, in the image captured with the telephoto lens, the letters “STOP” were clear and could be distinctly recognized (Fig. 5).

Fig. 5 Real-world image captured with the Tele & Wide coaxial camera

3 Tele & Wide Image Composition Processing

We developed image processing technology for a camera that integrates a wide-angle lens and telephoto lens. This technology is designed to provide the driver with highly visible images by combining the wide FOV of the wide-angle image with the detailed information of the distant scene captured by the telephoto image. We implemented distortion correction for the wide-angle image, composition of the telephoto image, and a digital mirror display that allows the

driver to adjust the FOV, Roll (horizontal rotation), Pitch (vertical rotation), and Yaw (horizontal direction) (Figs. 6 and 7).

While the wide-angle lens offers a wide FOV, it produces characteristic image distortion. To accurately correct this distortion, we mathematically modeled the characteristics of wide-angle lenses, including fisheye lenses, using Scaramuzza's model [1]–[3]. This model represents the projection of a wide-angle lens and the distortion in its image as polynomial functions. Using this model, parameters are calculated (calibrated) based on feature points obtained from projecting a checkerboard. By applying the obtained parameters to correct distortion in the wide-angle image, straightness is restored, allowing the driver to perceive information in a visually natural manner.

Because it is difficult to discern detailed information at long distances using only the wide-angle image, the telephoto image was composited onto the wide-angle image. In principle, because the wide-angle and telephoto lenses are aligned on the same optical axis and no parallax occurs, aligning the two images is straightforward. However, to compensate for manufacturing tolerances, it is necessary to perform precise alignment for each unit using an optimal-homography matrix. This made it possible to reliably integrate the wide FOV of the wide-angle image with the detailed information from the telephoto image.

In the digital mirror display, a projection transformation matrix is calculated from the FOV, Roll, Pitch, and Yaw parameters set by the driver, enabling real-time conversion of the distortion-corrected wide-angle and telephoto composite image to any desired viewpoint. When the FOV is set wide, the broad view of the wide-angle image is displayed, and when it is set narrow, the detailed information from the telephoto image is displayed, allowing the driver to obtain optimal information according to the situation.

In addition to the aforementioned alignment, the composition of the wide-angle and telephoto images requires that the exposure timing of both images match and their brightness and color tone be consistent. If these differ significantly between the two images, unnatural discontinuities may appear at the boundary between the wide-angle and telephoto images, even when they have been precisely aligned. To address this issue, our camera system incorporates a mechanism that enables coordinated operation between the image sensors and image processing on the wide-angle and telephoto sides. First, the vertical synchronous (Vsync) signals of the two sensors are synchronized to match their exposure timing, thereby eliminating temporal misalignment.

Fig. 6 Example of digital mirror operation (left: FOV = 90°, right: FOV = 40°)

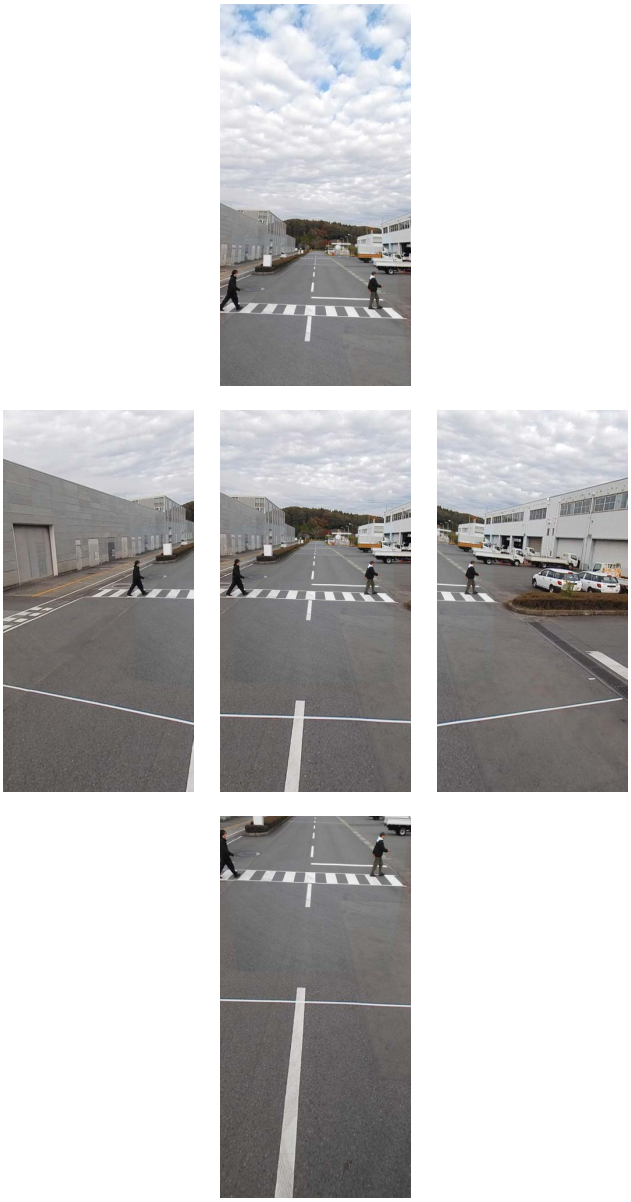

Fig. 7 Example of digital mirror Pitch and Yaw operation (center: Pitch and Yaw = 0°, top/bottom/left/right: Pitch or Yaw varied by 25° in each respective direction)

Next, luminance and color information are calculated from the exposure data of each sensor, and after coordinating the image processing, the two sensors are controlled again to match the brightness and color tone of the wide-angle and telephoto images. Figure 8 shows the composite results of the wide-angle and telephoto images with coordinated operation turned ON and OFF (the area inside the dashed line is the telephoto image). It was confirmed that the coordinated operation of the image sensors and image processing implemented in this camera system is effective in eliminating temporal misalignment and boundary discontinuities.

Coordinated operation ON / Coordinated operation OFF

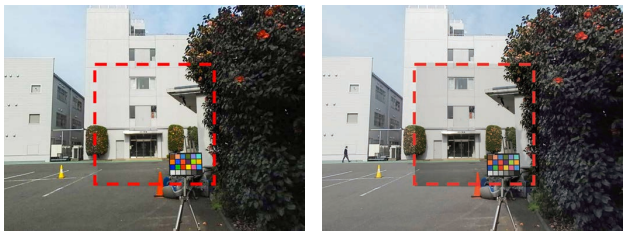

Fig. 8 Composite of wide-angle and telephoto images (coordinated operation ON/OFF: area inside the dashed line is the telephoto image)

4 Near-Infrared Compatibility

To enable shooting during both day and night, a filter that transmits only visible and near-infrared light (a multi-bandpass filter) is used. In general, the focal positions for visible and near-infrared light differ; therefore, if the sensor is positioned to focus on visible light, the focus will shift for near-infrared light. As a result, even if image quality is good for daytime shooting, it deteriorates during nighttime shooting. To mitigate this effect, the optical design incorporates axial chromatic aberration correction to minimize changes in focal position, thereby reducing image quality differences between daytime and nighttime shooting.

The advantage of near-infrared imaging with in-vehicle cameras is that it enables the acquisition of bright images, even at night in areas where light does not reach, such as in the shadows of vehicles or structures, without the need for additional visible illumination, thereby improving image recognition around the vehicle and enhancing safety. In addition, visible illumination can appear glaring to humans and may cause discomfort or impair visibility for pedestrians and drivers of surrounding vehicles, whereas near-infrared illumination does not adversely affect the vision of others and can further enhance their safety. Furthermore, because this camera system achieves near-infrared imaging using a multi-bandpass filter, it does not require switching between optical filters for visible and near-infrared light depending on bright or dark environments, eliminating the need for a filter drive mechanism and filter storage space, thereby contributing to camera miniaturization and cost reduction. Figure 9 shows the imaging results of this camera system and a conventional camera under dark conditions using near-infrared illumination.

This camera system / Conventional camera

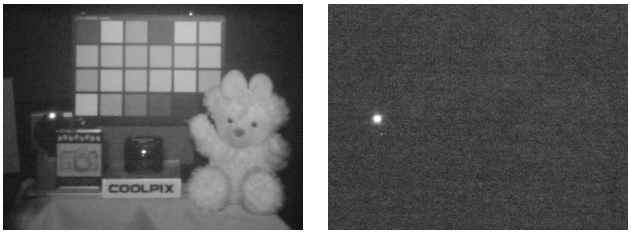

Fig. 9 Image comparison in a dark environment (illuminance: approx. 0.05 lux)
(with near-infrared illumination)

Meanwhile, because this camera system captures light containing a greater proportion of near-infrared components than conventional cameras (designed for visible light), maintaining conventional image processing results in images that appear visually poor to humans and reduce visibility. One of the intended applications of this camera system is an in-vehicle digital mirror, for which images must be rendered in a manner that humans can perceive naturally without discomfort. To address this issue, we optimized the multi-bandpass filter as well as the image processing, thereby achieving image quality comparable to that of conventional cameras, as shown in Fig. 10.

This camera system / Conventional camera

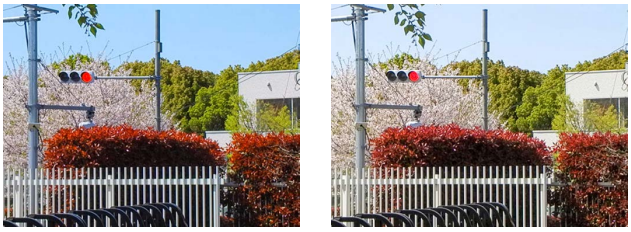

Fig. 10 Image comparison under daytime conditions

5 Other Considerations

The body of this unit employs a robust yet lightweight aluminum alloy and features a weather-resistant surface treatment, along with a sealed design with dustproof and waterproof protection applied to each component.

The shape was designed with mounting surfaces on the top, bottom, and sides to allow for various installation configurations, with a focus on robustness; however, because the

wide-angle side provides an ultra-wide FOV of 190°, minimizing the body size was an essential requirement to prevent the camera itself from appearing within the FOV.

In general camera development processes, the design of the lens unit—which requires a long development period—typically takes precedence, and the body is then designed to match it; however, this often leads to restrictions on the body shape. In particular, this unit required a more efficient body design, as it needed to accommodate a specially shaped lens unit with two image sensors arranged orthogonally, along with the interface boards for each sensor.

Therefore, in this unit, the lens unit and body were designed concurrently, with design information fed back between them to optimize their respective forms, and by leveraging high-density design expertise cultivated through the development of consumer cameras—where stringent miniaturization is required—we realized a body design that does not interfere with the ultra-wide FOV (Fig. 11).

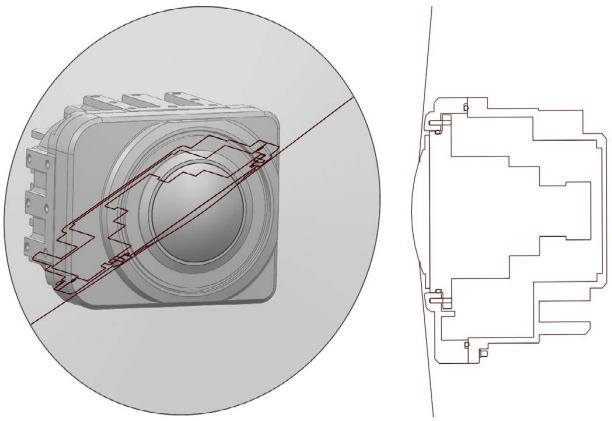

Fig. 11　Body design of the Tele & Wide coaxial camera

As mentioned above, although the focus position has been adjusted to account for reduced visibility caused by scratches or contamination, repair of the front lens may still be required depending on the extent of the damage. Regarding the repair method, the entire camera is often replaced with a new unit or disassembled to replace only the affected component; however, such approaches increase costs as well as the lead time and labor required for repair.

Therefore, in this unit, only the front lens was modularized to allow users to replace it themselves without the need for disassembling the body, thereby reducing repair costs and shortening lead time (Fig. 12). The replacement unit itself is also designed to ensure waterproofness, and its design maintains imaging performance even after replacement.

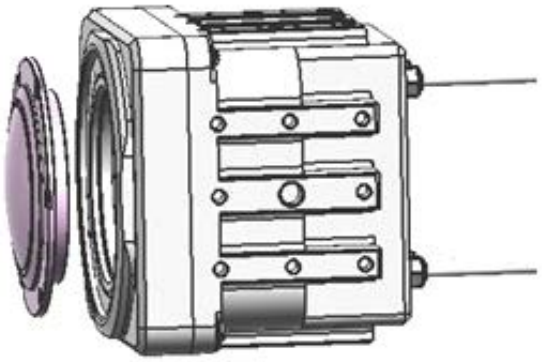

Fig. 12　Front lens replacement image

6 Conclusion

By contributing to advancing the driver-assistance systems and autonomous driving in the future automotive industry, Nikon aims to make broad contributions to society. These include reducing traffic accidents and improving safety, saving time and fuel and lowering CO_2 emissions through alleviation of traffic congestion, as well as enhancing delivery efficiency and addressing driver shortages in the logistics industry.

Finally, we would like to take this opportunity to express our sincere gratitude to the many individuals who devoted their efforts to the planning and development of this product.

References

[1] D. Scaramuzza, A. Martinelli, and R. Siegwart, “A Flexible Technique for Accurate Omnidirectional Camera Calibration and Structure from Motion,” *IEEE International Conference on Computer Vision Systems* (*ICVS 2006*), pp. 45–45, 2006.

[2] D. Scaramuzza, A. Martinelli, and R. Siegwart, “A Toolbox for Easily Calibrating Omnidirectional Cameras”, *IEEE/RSJ International Conference on Intelligent Robots and Systems* (*IROS 2006*), pp. 5695–5701, 2006.

[3] D. Scaramuzza, “Omnidirectional Vision: from Calibration to Robot Motion Estimation,” *PhD thesis, ETH Zurich, Thesis no. 17635*, 2008.

金岡浩史　Hiroshi KANAOKA
映像ソリューション推進室
Imaging Solution Development Department

倉茂孝道　Takamichi KURASHIGE
光学本部 開発戦略部
Strategic Technology Development Department
Optical Engineering

髙梨祐介　Yusuke TAKANASHI
株式会社ニコンシステム
Nikon systems Inc.

目黒明彦　Akihiko MEGURO
映像ソリューション推進室
Imaging Solution Development Department

築山大亮　Daisuke TSUKIYAMA
映像ソリューション推進室
Imaging Solution Development Department

和湯瑞葵　Mizuki WAYU
光学本部 シナジー推進部
Technical Synergy Promotion Department
Optical Engineering


金岡浩史
Hiroshi KANAOKA


倉茂孝道
Takamichi KURASHIGE


髙梨祐介
Yusuke TAKANASHI


目黒明彦
Akihiko MEGURO


築山大亮
Daisuke TSUKIYAMA


和湯瑞葵
Mizuki WAYU

衛星通信用空間光通信機器の光学設計

作田博伸，村上宏輔，島　直究

Optical Design of Free Space Optical Communication Devices for Satellite Communications

Hironobu SAKUTA, Kousuke MURAKAMI and Naoki SHIMA

カスタムプロダクツ事業部では，宇宙を利用した空間光通信用の光学系開発に携わっている．
フライト品は，開発後打上げて運用に至るまで長い期間を要する．2025年１月に，先進レーダ衛星「だいち４号」（ALOS-4）の大容量画像が静止軌道の光データ中継衛星を経由してダウンリンクに成功している．これら２つの衛星には，弊社で設計製作した光アンテナ（望遠鏡）が搭載されている．
一方，量子暗号通信の地上局について光通信機器の開発にも協力させていただいている．光通信では送信局・受信局で追尾が必要になるが，今回，衛星－地上局間通信における地上局の精追尾光学系を設計製造した．
本報告は，空間光通信の概要と開発した光学系の設計について解説する．

The Customized Products Business Unit is involved in the development of optical systems for space-based optical communications.
Flight products require a long time to be launched and operated after their development. In January 2025, large-volume images from the advanced radar satellite “Daichi-4” (ALOS-4) were successfully downlinked via an optical-data relay satellite in geostationary orbit. These two satellites are equipped with optical antennas (telescopes) designed and manufactured by our company.
Additionally, we are developing optical-communication equipment for the ground stations of quantum cryptography communications through a collaborative effort. Optical communications require tracking at the transmitting and receiving stations. Thus, we have designed and manufactured an optical system for precise acquisition and tracking at the ground station for satellite-to-ground station communications.
This report provides an overview of free-space optical communications and the design of the optical system developed.

Key words 空間光通信，光アンテナ，３枚鏡，精追尾，ファイバー結合
free-space optical communication, optical antenna, three mirrors, fine tracking, fiber coupling

1 Introduction

In recent years, various projects have been planned and implemented toward the practical use of space communications employing light. In space communications, the major challenges comprise ① transmitting large volumes of data in real time and ② ensuring secure information transfer.

One example of a solution to issue 1 is the LUCAS optical inter-satellite communications system, which is already in operation. When large-volume data are directly downlinked from low Earth orbit (LEO) to the ground, the communication time becomes short because the satellite is visible from the ground station only for a limited duration. By relaying the data once from LEO through a geostationary orbit (GEO) relay satellite, the communication time can be extended, and because the ground station can communicate continuously with the relay satellite, the real-time performance of communication can be improved. Communication between LEO and GEO is conducted using laser light in the 1.5 μm band, while communication between GEO and the ground is conducted by radio waves.

Research on optical communications for LEO satellite constellations is also being advanced through national projects. The construction of a network is ongoing in which data from Earth observation constellations are continuously relayed through optical inter-LEO constellation communications and rapidly downlinked to ground stations. Downlinking to ground stations faces the problem that communication cannot be established under adverse weather conditions due to the limited transmittance of light, and studies are being conducted on methods such as selecting a favorable site from multiple ground stations for communication (i.e., site

diversity) or employing transportable ground stations (hereafter, transportable stations) that can be moved to locations with good weather for downlinking.

To address the challenge of achieving secure information transfer, research on key distribution employing quantum cryptography via satellites is being conducted under the initiative of the Ministry of Internal Affairs and Communications, with the National Institute of Information and Communications Technology (NICT) playing a central role. In this study, transportable stations are employed to secure the communication link.

Thus, various efforts are being made toward the practical use of space optical communications, and the demand for optical communication equipment to realize such systems is likely on the rise.

The Customized Products Business Unit has performed design and manufacturing based on custom specifications provided by customers. We have long been engaged in products related to space and astronomy, developing optical systems for satellites and optical instruments for astronomical observation. Building on such experience, we now provide optical products related to optical communications to government agencies and companies.

In this paper, we describe the optical design and implementation of optical communication equipment undertaken by our company.

2 Configuration of Optical Communication Equipment and Optical System Specifications

As in radio communications, optical communications propagate optical signals spatially from the transmitting station to the counterpart optical communication station (hereafter, counterpart station), where the counterpart receiving station receives the optical signals. Figure 1 shows a schematic diagram of the link between the transmitting and receiving stations. The light source used is a laser, and for communication to be established, the emitted laser must be detectable by the detector of the receiving station. Therefore, a link budget is performed for the transmitted laser light to ensure that the link from transmission to reception is established, calculating the power gains and losses up to the receiving station, and the parameters are designed to secure sufficient margin relative to the sensitivity of the detector. The transmitted laser is expanded by the antenna within the transmitter and directed toward the receiving station. The larger the antenna aperture, the smaller the beam divergence becomes, and the greater the gain that can be obtained. The longer the propagation distance, the greater the diffraction loss becomes, and pointing errors also cause losses due to the intensity profile. The larger the aperture of the receiving antenna, the more light it can collect, resulting in higher gain. The parameters of each element, including the sensor employed, laser power, and antenna gain, are optimally designed as a system, taking feasibility into account [1].

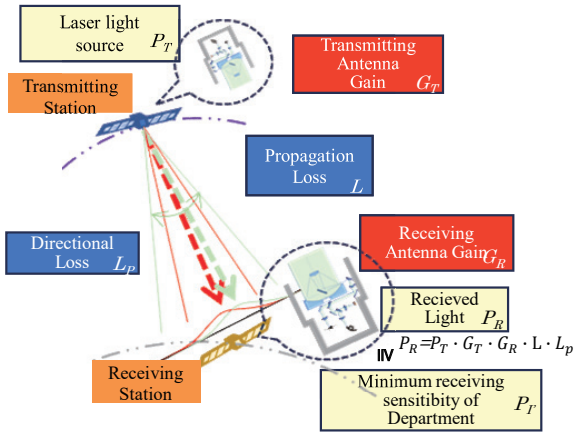

Fig. 1 Conceptual diagram of the link between the transmitting and receiving stations

Figure 2 shows an example of a conceptual diagram of the optical components of an optical communication equipment. The receiving system supports the optical antenna, which serves as the aperture for the transmitted and received light, and, through coarse pointing control by the coarse pointing mechanism and the coarse pointing sensor (CPS), together with fine pointing control by the fine pointing sensor (FPS) and fine pointing mirror (FPM), transmits the received laser light to the receiver (RX), whose axis is aligned with the center of the FPS field of view. Figure 3 shows the relationship between the fields of view observed by the sensors in coarse pointing and fine pointing.

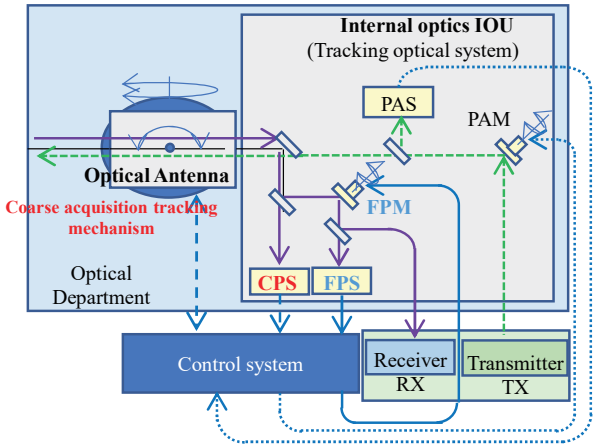

Fig. 2 Conceptual block diagram of the optical components of the optical communication equipment

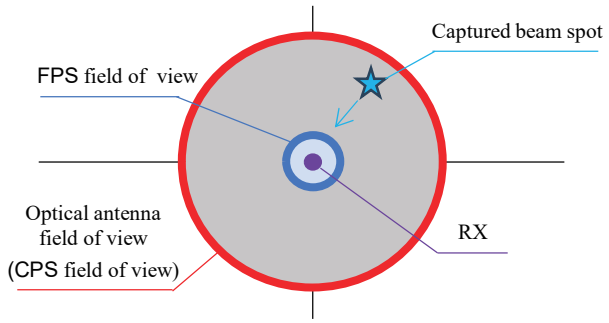

Fig. 3 Conceptual diagram of sensor fields of view and beam spot control

Meanwhile, in the transmitting system, because the counterpart station moves relative to the local station during the propagation of the laser light emitted from the transmitter (TX) until it reaches the counterpart station, the transmission is performed through the point-ahead mirror (PAM) to compensate for this effect (Fig. 4). The figure shows an example of satellite-to-satellite communication, but the same applies to satellite-to-ground communication.

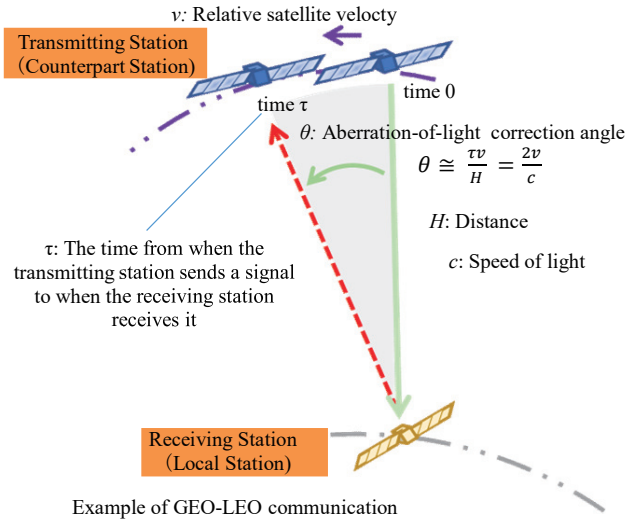

Fig. 4 Aberration-of-light correction

The optical system of the optical communication equipment must efficiently deliver the communication light to the counterpart station without attenuation. The antenna gain shown in Fig. 1 is determined by the wavelength λ, aperture area A, and efficiency η, as expressed by the following equation:

$$G = \frac{4\pi}{\lambda^2} A \cdot \eta$$

Factors related to the efficiency η attenuate the gain, and specifications of the optical system include obscuration ratio, transmittance, polarization loss, and wavefront aberration. In addition, the noise characteristics (stray light) of the transmitted and received beams are also important factors related to η.

Because the optical antenna and internal optical unit (IOU) may be handled by different teams, their specifications are reallocated, and each optical system is designed accordingly.

3 Optical Antenna of the LUCAS Optical Inter-Satellite Communication System

Here, we describe the optical antenna system that constitutes the LUCAS optical inter-satellite communication equipment.

The optical antennas of the optical inter-satellite communication equipment mounted on the optical data relay satellite and Earth observation satellite employ a common architecture, with the aperture diameters determined according to the allocations of each system. While NEC was responsible for the development of the optical inter-satellite communication system, Nikon was in charge of the optical design, optical component fabrication, and optical system assembly of the optical antenna. In this section, we introduce Nikon's responsibilities.

3.1. Optical System Design

The main specifications of the optical antenna system are listed in Table 1. These items were determined based on the system allocation values and Nikon's optical system study. The optical antenna is an afocal telescope system with an angular magnification of 20x. During reception, light enters the aperture of the optical antenna, and the beam is reduced in size and guided to the subsequent IOU.

Table 1 Main Specifications of the Optical Antenna

	GEO	LEO
Aperture diameter	ϕ150	ϕ100
Angular magnification	20x	20x
Wavefront error	λ/30	λ/30
Field of view	± 0.1 deg	± 0.2 deg
Polarization preservation	2 %	2 %
Transmission loss	0.3 dB	0.3 dB
Back reflection	65 dB	65 dB

During transmission, the beam from the IOU is expanded by the optical antenna and emitted. The received and transmitted beams have different wavelengths but pass through the common optical path of the optical antenna. Figure 5 shows the optical path diagram of the GEO optical antenna. As shown in the figure, the antenna is composed of three off-

axis mirrors and a flat folding mirror that directs the beam to the subsequent IOU, and it is designed to be compact. The three-mirror system has a concave–convex–concave configuration, with the respective surfaces being parabolic, hyperbolic, and elliptical. This configuration suppresses field curvature, reduces wavefront error, and accommodates a wide field of view. The advantages of the optical system are that, with no central obscuration and the use of high-reflectivity coatings on the mirror surfaces, it achieves high transmittance with extremely low loss, and the return light from the transmission beam emitted by the IOU does not pose a problem. Meanwhile, it is not a configuration that can correct distortion aberration, and it has the drawback of a magnification distribution within the field of view due to distortion. Therefore, to align the incoming light with the center of the field of view, it is necessary to perform pointing by nonlinear control of the angular adjustment of the pointing mechanism.

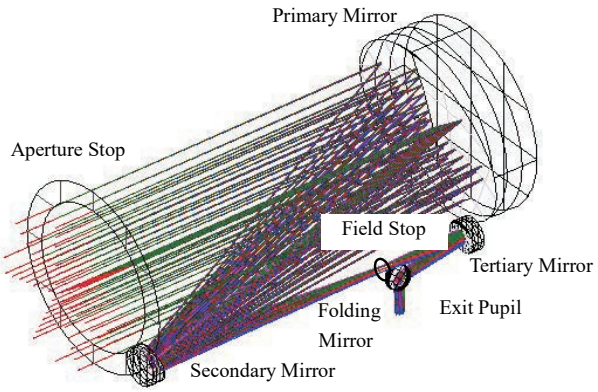

Fig. 5 Optical path diagram of the optical antenna section

During reception, the transmitted light enters the IOU with power P_R, attenuated to a weak level by the loss factors described in Section 2, as shown in Fig. 6. Meanwhile, during transmission, a strong laser power $P_{R'}$ is emitted, and in this optical system, a scattered light power $P_{N'}$ enters the receiver optical path within the IOU. This light noise can be addressed by the design and fabrication of each mirror component. In addition, there are strong stray light sources, such as sunlight, from outside the field of view. Gaps that exist in the optical design are filled with a mechanical structure, field stop, and stray light cover to prevent this from mixing into the IOU. Fig. 7 shows the fabricated mirrors. Weight reduction is required for components of satellite-mounted hardware, and because the primary mirror of the optical antenna has a larger aperture than the other parts, its backside is hollowed out to reduce weight.

The mirror surfaces were processed into aspheric shapes by grinding and polishing. The wavefront accuracy of the

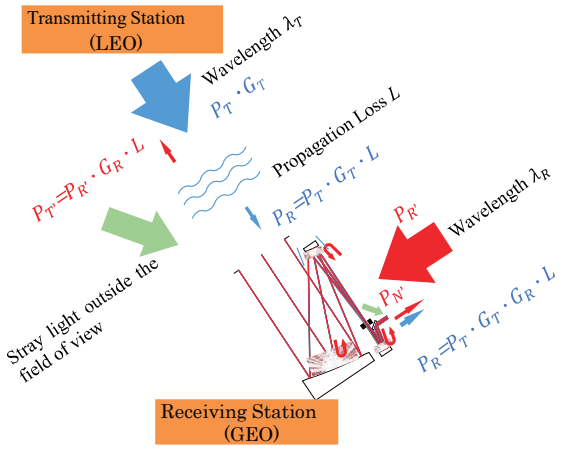

Fig. 6 Received light and scattered light noise

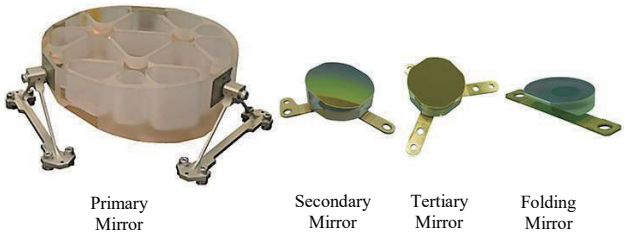

Fig. 7 Fabricated mirrors of the optical antenna

optical antenna in orbit is specified as λ/30 at a wavelength of λ = 1530 nm. Because the surface accuracy requirements for the mirrors are also stringent, the desired accuracy was achieved through polishing based on null testing using CGHs and other methods with an interferometer.

3.2. Coating

The transmission loss and polarization dependence of the optical system depend on the performance of the reflective coatings of the optical components. From the perspective of transmission loss, each component required coatings with high reflectance and low polarization dependence. To meet both requirements in the design, aspheric mirrors with small incident angles were coated with metal plus dielectric films, while the folding mirrors with large incident angles were coated with dielectric films. The design was made to ensure high manufacturability. The reflectance measurement results obtained with test pieces are shown in Fig. 8.

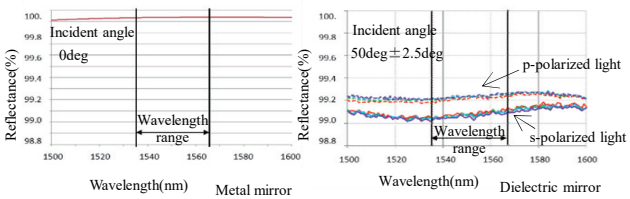

Fig. 8 Mirror reflectance

As shown in the optical path diagram of Fig. 5, the clearance between the beam from the field stop to tertiary and

folding mirrors is narrow, and the folding mirror is shaped, as illustrated in Fig. 7, with its disk sides flattened and back-side tapered. During the fabrication of the folding mirror, the reflective coating was a multilayer film, and the surface deformation due to film stress was significant, making it difficult to achieve the required surface accuracy despite it being a flat mirror. Therefore, the mirror shape was corrected in anticipation of deformation by film stress, thereby improving the transmitted wavefront accuracy.

Because relatively high-power lasers are used in LUCAS, it is necessary for the reflective coatings to have laser resistance. The maximum incident laser power was specified as 5 W, requiring resistance at a maximum power density of 0.3 W/mm^2 for the LEO optical antenna with its smaller beam. Before fabricating the components, irradiation tests were conducted using test pieces. The appearance and reflectance were measured before and after irradiation, and because no significant changes were observed in either evaluation item, the components were confirmed to be problem-free and installed in the product.

3.3. Assembly

The primary mirror is supported by a structure in which Super Invar pads are placed at three points on its side and held by flexures. The secondary, tertiary, and folding mirrors were bonded at their back-center areas to holders to minimize distortion in the mirrors, and these units were mounted onto the support structure provided by NEC to assemble the entire optical antenna. To measure the wavefront accuracy of the optical antenna, an interferometer was placed in the direction of the exit pupil, and a flat mirror was positioned on the aperture-stop side of the antenna to configure the measurement system. The required wavefront accuracy was achieved by adjusting the decentering and spacing errors, mainly between the primary and secondary mirrors, to the micrometer level.

After assembly, vibration tests and other evaluations were conducted to verify that performance could be maintained during flight and operation, and the optical antennas for both GEO and LEO applications were delivered to NEC.

4 Optical Design of Ground Stations for Satellite Quantum Cryptography Communications

To ensure security through the use of space, the development of satellite quantum cryptography communications is ongoing. As shown in Fig. 9, quantum keys are delivered as signal light from the satellite to the ground station, but the signal itself is extremely weak. For acquisition and tracking, beacon light stronger than the signal light is transmitted from the satellite, and the signal is received while tracking the beacon light. Nikon also contributed to this development through design and manufacturing.

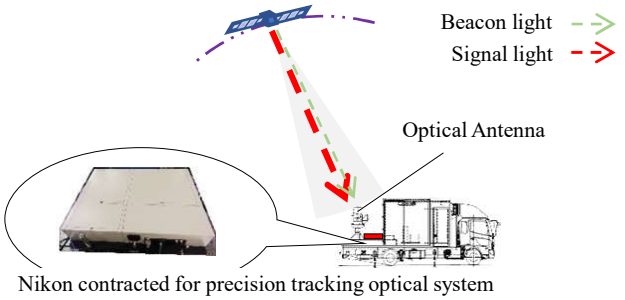

Fig. 9 Conceptual diagram of optical communication between a satellite and transportable ground station

The configuration of the optical system consists of, as mentioned above, the optical antenna and IOU. The optical antenna is a Cassegrain telescope with a central obstruction, and the IOU is the precise acquisition and tracking optical system, which was designed with only a receiving function for a downlink-only experiment. Therefore, laser transmission was not conducted.

4.1. Optical Interface with the Transportable Ground-Station Optical Antenna

Table 2 shows the specifications and optical interface of the transportable ground-station optical antenna. Light is collected by a 355-mm aperture Cassegrain telescope, and after being relayed through a Coudé optical path, it is directed to the precise acquisition and tracking optical system. The exit pupil position of the Coudé path was defined as the optical interface, and the end face of the optical bench on which the precise acquisition and tracking optical system is mounted was defined as the mechanical interface.

Table 2 Optical Interface between the Transportable Ground-Station Optical Antenna and Precise Acquisition and Tracking Optical System

Item	Specification
Telescope format	Cassegrain/Coude type
Effective aperture diameter	ϕ355 mm
Magnification	17.75x
Field of view	ϕ1 mrad
Exit pupil diameter	ϕ20 mm
Telescope exit pupil position	1774 mm from the edge of the optical surface table

4.2. Functional Configuration of the Precise Acquisition and Tracking Optical System

The functional configuration of the precise acquisition and tracking optical system is explained with reference to Fig. 10.

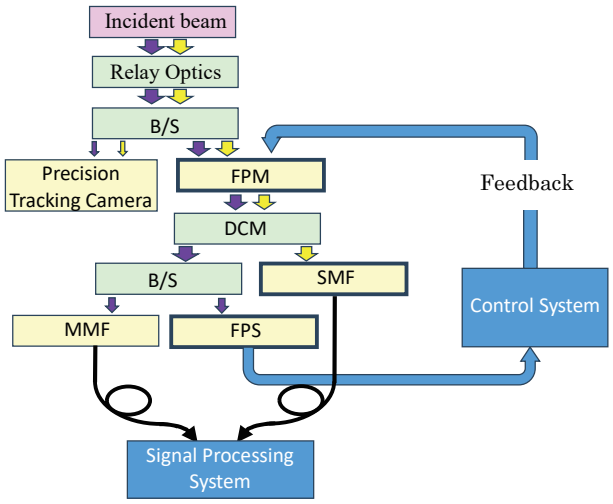

Fig. 10 Functional configuration of the precise acquisition and tracking optical system

The beam incident from the optical antenna is divided by a beam splitter (B/S) into a coarse tracking path and precise tracking path. The role of observing the CPS field of view in Fig. 3 corresponds to the precise tracking camera.

An FPM is placed in the precise tracking path, which serves to suppress seeing effects, i.e., tilts of the beacon light caused by disturbances.

Because the beacon and signal light are at different wavelengths in the 1.5-μm band, a dichroic mirror (DCM) is placed behind the FPM to separate them.

The beacon light is split by the B/S into the multimode fiber (MMF) and FPS. The MMF receives the beacon light and is used for synchronization of signal detection.

The signal and beacon light are transmitted coaxially. The FPS, a sensor for detecting beam spot fluctuations caused by seeing effect, and a quadrant detector (QD) were used. The beacon light is directed to the QD, forming a beam spot on the QD. The centroid is calculated from the QD output of the beam spot, and based on this, feedback is applied to the FPM to control the tilt.

As shown in Fig. 11, when disturbances are suppressed by the FPM and the beam spot is held at the center of the FPS, the signal light coaxial with the beacon light is stably focused onto the end face of the single-mode fiber (SMF), enabling efficient fiber coupling.

The design requires the selection of devices, such as the FPM, FPS, SMF, and MMF, from commercially available

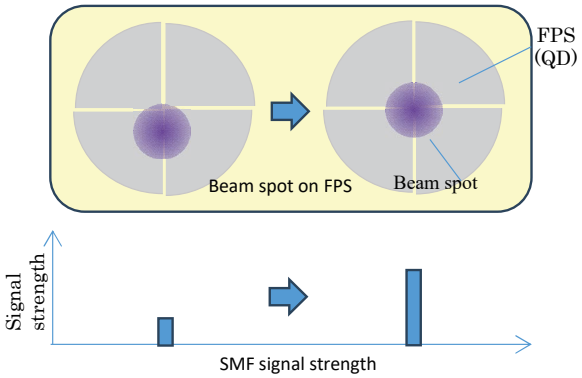

Fig. 11 Conceptual diagram of beam spot control and signal intensity effect in the feedback system

products. Based on the system specifications of the precise acquisition and tracking optical system, appropriate devices are selected, and the specifications of the optical elements are determined accordingly.

As a design requirement for the optical layout of the FPM, the exit pupil of the optical antenna is relayed and imaged onto the FPM. The FPM must control tilt at high speed; therefore, it is desirable for it to be compact and lightweight. In addition, the driving range of tip-tilt in commercial FPMs is specified and therefore cannot be exceeded. Meanwhile, as a design requirement for the relay system, the overall length had to be shortened to make the entire apparatus compact while still allowing the placement of optical elements, such as the previously mentioned B/S for beam-path division and filters.

Fig. 12 shows an optical model of the precise acquisition and tracking system. In the most basic configuration (Configuration 1), as the distance from the optical antenna exit pupil to the f1 lens becomes longer, the image position of the pupil where the FPM is placed approaches closer to the f2 lens. To solve this problem, as in Configuration 2, a concave field lens is placed at the focal position to change the direction of the off-axis rays, and by increasing the ray height incident on the f2 lens, the position (pupil) where the rays refracted by the f2 lens intersect the optical axis shifts farther back. In principle, this concept was aimed at miniaturizing the relay system. As a result, it became possible to place the FPM at the pupil position while securing space for the B/S and filters, achieving low loss and reduced aberrations with a minimal lens configuration. Fig. 13 shows the configuration, including the holding structure of the lens system.

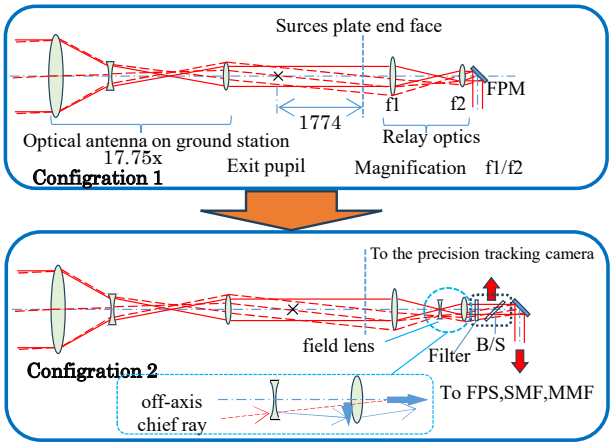

Fig. 12 Optical model of the precise acquisition and tracking system

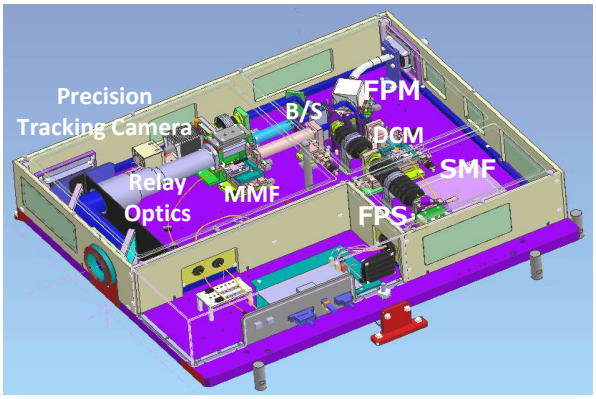

Fig. 13 Configuration diagram of the precise acquisition and tracking optical system

5 Conclusion

Among our recent products for space optical communications, we have introduced the optical antenna for the LUCAS inter-satellite optical communication equipment, along with the design and fabrication of the precise acquisition and tracking optical system for quantum cryptography communications.

LUCAS has been operated for optical communications between GEO and LEO, to which the optical systems manufactured by our company were able to contribute.

A demonstration of key transmission by optical means between the ISS and a ground station was conducted with the aim of social implementation of the quantum cryptography communication system. The precise acquisition and tracking optical system of the transportable ground station, manufactured by our company, also contributed to the demonstration.

The development of the optical antenna for the LUCAS inter-satellite optical communication device was performed under the guidance of JAXA and NEC. In addition, the development of the precise acquisition and tracking optical system for the transportable ground station was conducted in collaboration with NICT and SKY Perfect JSAT. We would like to express our gratitude to all those involved for their cooperation.

References

[1] J. Liang, A. U. Chaudhry, E. Erdogan, and H. Yanikomeroglu, “Link budget analysis for free-space optical satellite networks,” 2022, *arXiv:2204.13177*.

作田博伸　Hironobu SAKUTA
カスタムプロダクツ事業部 開発部
Development Department
Customized Products Business Unit

村上宏輔　Kousuke MURAKAMI
光学本部第一設計部
1st Designing Department
Optical Engineering

島　直究　Naoki SHIMA
光学本部第一設計部
1st Designing Department
Optical Engineering

作田博伸
Hironobu SAKUTA

村上宏輔
Kousuke MURAKAMI

島　直究
Naoki SHIMA

多回転バッテリレスアブソリュートエンコーダ「MAR-M700MFA」の開発

後藤雅彦，阿部　桂，千代晋平，山本拓巳，常盤圭佑

Development of a Multi-Turn Battery-Free Absolute Encoder「MAR-M700MFA」

Masahiko GOTO, Kei ABE, Shimpei SENDAI, Takumi YAMAMOTO and Keisuke TOKIWA

アブソリュートエンコーダは，自動車製造ラインの産業用ロボットや工作機械など，産業機械に幅広く利用され，ロボットアーム等の回転変位を絶対値で検出することができるセンサである．2023年11月にリリースした多回転アブソリュートエンコーダ「MAR-M700MFA」は，世界で初めて全固体電池を搭載し，保証温度の向上及びメンテナンスフリー化を実現した．新たに予知保全機能や角度精度自己補正機能を搭載し，産業用ロボット等の利用環境拡大，稼働安定性向上，モーション制御の高精度化に貢献する．本稿では，「MAR-M700MFA」が持つ技術的特徴について解説する．

An absolute encoder is a type of sensor device commonly used in industrial robots in automobile manufacturing lines, machine tools, and various other applications. It detects absolute values for robot-arm rotational displacement and similar measurements. MAR-M700MFA, a multi-turn absolute encoder released in November 2023, offers an increased guaranteed operational temperature range compared to the previous multi-turn external battery-free absolute encoder of the company. This is because of the utilization of an all-solid-state battery, which renders this model maintenance-free. Furthermore, this model is equipped with new features including predictive maintenance and angular accuracy self-correction functions, which enable an expanded range of possible usage environments for industrial robots, improved operational consistency, and greater precision in motion control. This article explains the technical features of “MAR-M700MFA”.

Key words アブソリュートエンコーダ，バッテリレス，メンテナンスフリー，予知保全，角度精度自己補正，全固体電池
absolute encoder, battery-free, maintenance-free, predictive maintenance, angular accuracy self-correction, all-solid-state battery

1 Introduction

An absolute encoder is a sensor widely used in various industrial machines, such as industrial robots in automobile manufacturing lines and machine tools, and it is capable of detecting the absolute rotational displacement of components such as robot arms. In response to diversification of requirements in recent years, functionality of sensors has advanced, and the “MAR-M700MFA” (Fig. 1) is the first in the world to incorporate an all-solid-state battery, thereby achieving an increased guaranteed temperature range and maintenance-free operation. Furthermore, it is equipped with newly developed functions for predictive maintenance and angular accuracy self-correction functions, contributing to an expanded range of operating environments for industrial robots, improved operational stability, and enhanced precision in motion control [1]. In this paper, the technical features of the “MAR-M700MFA” are described.

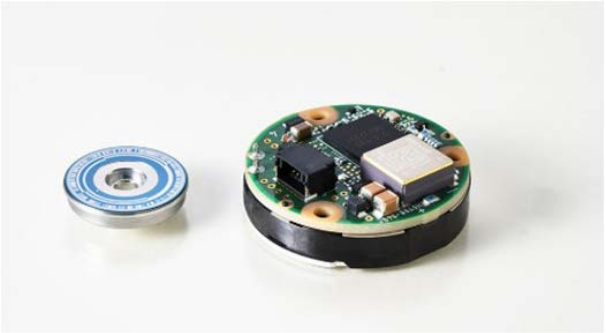

Fig. 1　Multi-turn absolute encoder “MAR-M700MFA”

2 Configuration

Encoder detection methods generally include optical, magnetic, and electromagnetic induction types, and the optical type is often adopted for absolute encoders that require high accuracy and high resolution. The principle of the optical

encoder (Fig. 2) is briefly explained below. When positional displacement (shaft rotation) occurs in an optical encoder, variations in light and dark are generated in the light transmitted through the rotating disk. This variation in light is captured by a photodetector, which is subjected to photoelectric conversion and amplification, and then processed through interpolation (subdivision reading), after which it is output to the host device as positional data [2].

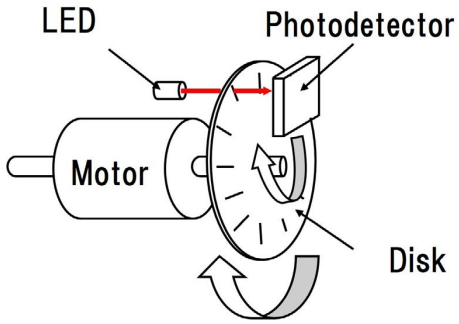

Fig. 2 Principle of the encoder

In recent years, from the perspectives of robot miniaturization and design flexibility, smaller and thinner absolute encoders have been required. A comparison between the conventional transmissive optical system and reflective optical system is shown in Fig. 3.

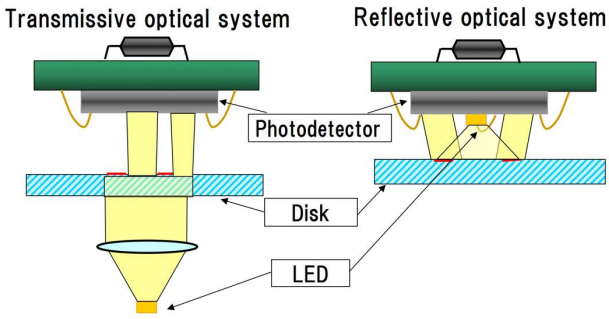

Fig. 3 Comparison of transmissive optical system and reflective optical system

In the reflective optical system, the light source LED and photodetector are arranged on the same plane. In the conventional transmissive optical system, a distance was required between the LED and photodetector, whereas in the reflective optical system, the optical path lengths for projection and reception are shorter, enabling a more compact design. By adopting the reflective optical system, the product height is approximately halved, thereby achieving a lower profile [2], [3]. In addition, while conventional disks were generally made of glass, the reflective type employs a metal disk, thereby improving reliability. In recent years, reflective optical system absolute encoders have become the mainstream, and our company has been employing the reflective optical system for more than ten years. This has enabled us to build a substantial track record and provide an extensive product lineup.

The product introduced here inherits the reflective optical system and has been further evolved with additional functions. In the conventional configuration, position detection was performed with a single optical system, whereas in this product, the optical system is configured with two systems (Fig. 4).

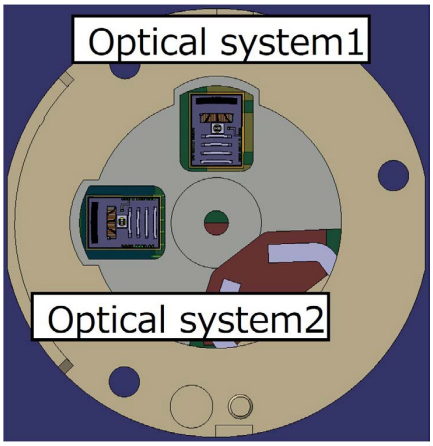

Fig. 4 Arrangement of the two optical systems

By performing position detection with these two independent optical systems, the product is able to provide two sets of positional data. This has made it possible to add predictive maintenance and angular accuracy self-correction functions.

The predictive maintenance function can detect signs of failure in advance and notify the host equipment of the timing for component replacement or maintenance of industrial robots beforehand via the communication protocol (A-format®). As a result, it becomes possible to suppress the risk of sudden stoppages of equipment or production lines due to failures. In addition, the angular accuracy self-correction function enables accuracy correction without the use of a reference encoder, contributing to improved operational stability and enhanced motion accuracy.

Furthermore, in an absolute encoder, in addition to angular absolute position detection, a multi-turn detection function is essential to count the number of rotations. This multi-turn detection function must operate even when the main power supply is turned off; however, in conventional products, an external battery had to be provided on the host equipment side, and the function operated on the external battery power when the main power was off. Therefore, replacement of the external battery is indispensable during maintenance. Moreover, because absolute encoders are combined with AC servo motors, they are often used in high-

temperature environments, making high-temperature tolerance essential for the encoder.

To address these issues, this product incorporates a highly safe all-solid-state battery capable of operating in high-temperature environments, thereby extending the operating temperature range up to 105°C. In addition, by employing a switching element so that power from the all-solid-state battery is supplied to the multi-turn detection unit only when positional displacement occurs, more than ten years of backup is ensured at the time of shipment. Further, depending on the operating temperature, more than ten additional years of backup may be achieved even after ten years of continuous use, thereby realizing long service life. The main specifications are listed in Table 1 [4].

Table 1　Specifications List

External diameter	Φ35 mm
Height	12.48 mm (TYP)
Single-turn Resolution	Max 27 bit
Multi-turn signal Resolution	16 bit
Responsive revolution speed	8,000 min^{-1}
Power source voltage	5 V ± 10%
Current used	120 mA (TYP)
Operating temperature range	−20～+105°C
Communication protocol	A-format®

The product height is 12.48 mm, achieving the same height as that of conventional products. In addition, because it has been designed with compatibility with conventional products in mind, it can be mounted on the motor side without requiring any design modifications.

Next, the details of each function are described.

3 Predictive Maintenance Function

Conventional encoders were equipped only with a function that outputs an error when an abnormality occurs, forcing the equipment to shut down suddenly at the moment the error occurs. A sudden stoppages of a production line not only causes deterioration in product quality and delays in production schedules but also requires time for equipment restart, significantly affecting the overall productivity of the factory.

In contrast, this product incorporates a predictive maintenance function that detects signal degradation in advance and notifies the host equipment. When a degradation in signal quality caused by factors such as LED deterioration is detected, a predictive maintenance alarm is output to the host equipment via A-format®. With this predictive maintenance function, planned maintenance can be carried out before equipment shutdown, making it possible to significantly reduce the risk of sudden stoppages in production lines. Through planned maintenance, component replacement can be carried out at the optimal timing in accordance with the production schedule, thereby minimizing downtime. In addition, because replacement parts can be arranged and maintenance personnel secured in advance, efficiency in maintenance operations can also be achieved. The predictive maintenance alarm is output without affecting equipment operation, making it possible to conduct these preparations while maintaining productivity.

Furthermore, to achieve even higher reliability, the product also provides measures to address random failures. In a product, due to slight variations during manufacturing or potential latent defects, there is a low probability that unexpected failures may occur during its service life. Such random failures are difficult to detect through pre-shipment inspections, and even with countermeasures such as aging, complete prevention is challenging and requires significant cost and time. Even such random failures can be detected at an early stage by means of the predictive maintenance function. However, in the case of random failures, the period from the occurrence of a predictive maintenance alarm to the actual failure tends to be shorter than that for ordinary degradation. Therefore, in this product, the switching function employing two independent optical systems—one for position detection and the other for signal quality monitoring—is used to provide a solution. In the event that a predictive maintenance alarm is triggered in one optical system due to a random failure, the system automatically switches to the other optical system, which is still less affected by degradation and maintains reliability (Fig. 5). This makes it possible to detect and notify signs of random failures in advance while continuing operation in a highly reliable state until maintenance can be performed. In this way, the combination of the predictive maintenance function and dual optical systems ensures stable operation of the equipment.

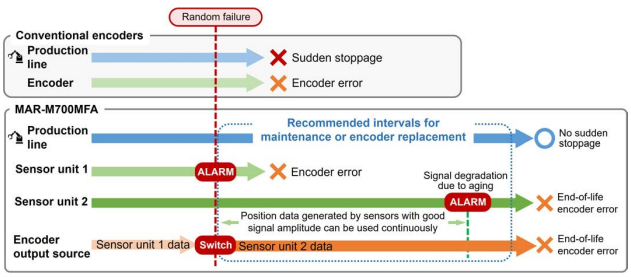

Fig. 5　Image of the switching function

4 A-format®

A-format® is a proprietary communication format for encoders developed by our company. It can output fundamental encoder information, such as position data and temperature data from the temperature sensor built into the encoder, to the host equipment.

In developing this product, the following three functions were added:

- Output of predictive maintenance alarms and status information from each optical system
- Output of velocity information computed within the encoder
- Expansion of the non-volatile memory area for user data

(Output of predictive maintenance alarms and status information from each optical system)

The aforementioned predictive maintenance alarms and status information of each of the two independent optical systems are realized by utilizing previously unused areas, without modifying the data frame structure. As a result, it was possible to add functions while maintaining consistency with the basic specifications and minimizing the impact on the system.

(Output of velocity information computed within the encoder)

Regarding the output of velocity information computed within the encoder, conventionally, it was necessary for the host equipment to calculate the velocity from position data at each communication cycle. In this product, however, velocity is computed internally within the encoder, enabling measurement at shorter intervals and providing more accurate velocity information. The combination of this position data and high-precision velocity data contributes to realizing smoother motion control.

(Expansion of the non-volatile memory area for user data)

Regarding the expansion of the non-volatile memory area for user data, it was previously possible to store information such as the device serial number, operating parameters, and motor-side parameters. With the increased capacity, however, it has become possible to retain a larger amount of information, including various correction data and maintenance records.

In this way, by extending the communication format while maintaining compatibility with the conventional specifications, the product achieves both the addition of new functions—such as the implementation of predictive maintenance function, improved control performance, and expanded storage capacity—and compatibility with existing systems.

5 Angular Accuracy Self-Correction Function

One type of error present in an encoder is repeatable error once per revolution. These errors typically arise from the following factors:

- Errors in the disk pattern caused by manufacturing
- Eccentricity during encoder disk installation
- Runout or angular misalignment of the motor shaft

Errors caused by these factors present a challenge in motor control using encoders, as they lead to issues such as rotational speed fluctuations in the motor itself and, as a consequence, abnormal noise and vibration throughout the entire robot system.

Approaches taken by encoder manufacturers to address errors generally include eliminating fundamental errors through adjustments known as eccentricity correction—aligning the rotational center with the disk pattern center—and improving component precision to the micrometer order. In addition to these, electrical correction within the encoder is also employed.

Several corresponding methods of electrical correction are publicly known, with the representative ones listed below [5]:

- Correction by comparative measurement with a high-precision reference encoder
- Correction by comparative measurement with a reference instrument using the equal divided average method
- Self-correction by incorporating the equal-division averaging method into the product itself

Although many other correction methods exist, conventional electrical correction has faced the following challenges:

- Investment in expensive reference instruments
- Increased working time due to correction procedures
- Enlargement of the product due to self-error detection and self-correction mechanisms

This product incorporates a new correction function that addresses these challenges. Through a proprietary process utilizing dual optical systems, the challenges inherent in conventional methods have been resolved.

In this product, the correction process is executed simultaneously with automatic signal adjustment (Auto Tuning) during product integration. Conventionally, correction work required several minutes, but it has been shortened to less than 15 seconds. The experimental results obtained with a prototype are shown in Fig. 6.

Although it is a relatively small-diameter encoder, which is

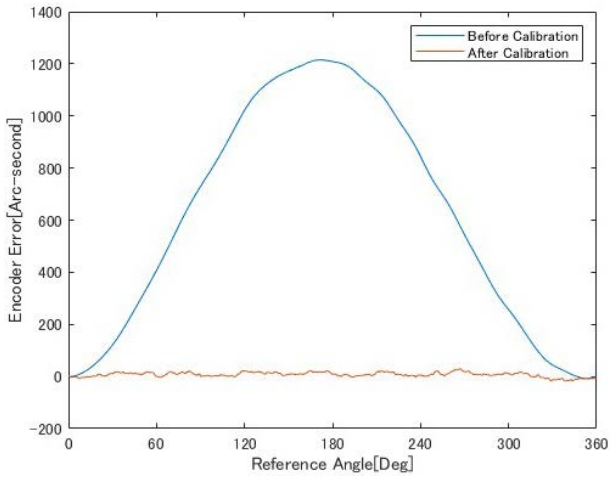

Fig. 6 Accuracy measurement results: comparison before and after correction

known to have larger errors compared to large-diameter encoders, this product achieved a After-self-correction accuracy of 39 counts full width (≈0.0136°) in terms of 20-bit representation, thereby attaining a high-level balance between workability and accuracy. This product is expected to provide new benefits through improved accuracy by means of the angular accuracy self-correction function, not only for users who have long required high accuracy but also for those who previously did not place emphasis on accuracy.

6 Multi-Turn Detection using an All-Solid-State Battery

This product adopts the proprietary multi-turn detection method established in previous models. The built-in battery mounted on the encoder board has been changed from a lithium primary battery to an all-solid-state battery. Because the all-solid-state battery is a secondary battery, a dedicated charging circuit was designed to ensure sufficient backup retention time in actual operating environments—that is, the duration during which multi-turn position information can be retained by the battery mounted on the board when the encoder's main power supply is turned off. Charging of the all-solid-state battery is automatically controlled internally when the encoder's main power supply is turned on. Therefore, in actual operating environments, users do not need to be concerned with charging or discharging, and from the user's perspective, the encoder can be treated as battery-free.

In addition, by adopting the proprietary multi-turn detection method established in previous models, the product inherits the reliability of multi-turn detection and mounting compatibility from previous models, with an equivalent product height. In conventional technologies for battery-free encoders, the mainstream approaches have been either mounting a power generation element on the circuit board and using its output signal for both power supply and position detection, or the gear-based method, both of which result in an increased product height. By employing a proprietary detection method and configuring a magnetic circuit, our battery-free encoder is able to retain a thin, easily mountable mechanism that also includes the method of attaching the encoder disk.

A key feature of the multi-turn detection method of this product is that the output of the power generation element is not used for power supply or position detection but solely for switching to perform multi-turn position detection and its retention (Fig. 7).

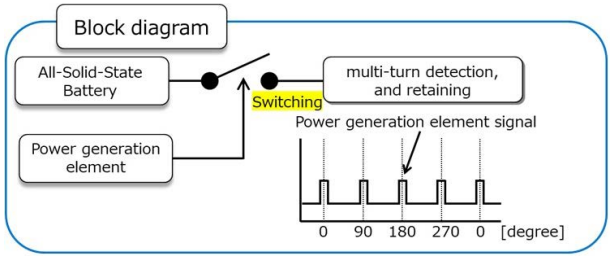

Fig. 7 Block diagram of the multi-turn detection method

When the motor shaft rotates while the encoder is not supplied with its main power, an output signal from the power generation element is generated in the magnetic circuit. As a result, the switching shown in Fig. 7 changes from OFF to ON, power is supplied from the all-solid-state battery, multi-turn position detection and its retention are performed, and once the process is completed, the switching changes back from ON to OFF. Multi-turn position detection in the state where the switching is ON adopts a configuration that momentarily activates the optical detection circuit to read the encoder disk pattern. This detection method is a configuration that combines two different detection systems: a magnetic system that operates the power generation element to switch the circuit and an optical system that actually detects the position of the encoder disk. As a result, even if the encoder is subjected to an external magnetic field in its actual operating environment while the motor shaft is at rest and an unintended power generation element signal is produced, it does not affect the multi-turn position detection, thereby providing an advantage in terms of resistance to external magnetic field disturbances. This has been translated according to the original source text. However, please check if a more suitable alternative would be "the multi-turn

position detection remains robust to external magnetic field disturbances."

7 Conclusion

"MAR-M700MFA" is an absolute encoder widely used in industrial robots and machine tools, incorporating the latest technologies such as precise position detection and enhanced environmental resistance.

This product, while inheriting conventional technologies, significantly enhances performance and reliability compared to previous models through the addition of new functions. As a result, it not only meets the diverse needs of industrial machinery but also achieves greater design flexibility for miniaturization and modularization, as well as stable operation even in high-temperature environments. With its introduction, the product is expected to improve production efficiency (*e.g.*, shortening operating time of manufacturing lines) and reduce maintenance costs (e.g., lowering the frequency of component replacement), and it is also expected to contribute to the advancement of next-generation industrial machinery (e.g., realization of automation and smart factories).

In the future, we will expand the product lineup equipped with these functions and advance the development of products that meet a wider range of applications and diverse needs.

References

[1] Nikon corporation, 2023, "Release of World's first, Multi-turn battery-free Absolute Encoder「MAR-M700MFA」mounted with All-Solid-State Battery," (in Japanese), [Online]. Available: https://www.nikon.com/company/news/2023/1120_encoder_01.html

[2] M. Goto, "Latest developments in absolute encoders for AC servomotors," (in Japanese), in *Proc. Motor Technology Symposium*, 36th ed, 2016.

[3] T. Morita, "Introduction to absolute encorder sensor and future trends," (in Japanese), *Journal of the Japan Society of Precision Engineering*, vol. 9, no. 82, pp. 797–802, 2016.

[4] Nikon corporation, "World's first, Multi-turn battery-free Absolute Encoder mounted with All-Solid-State Battery," (in Japanese), [Online]. Available: https://www.nikon.com/business/encoder/mar-m700mfa/

[5] T. Masuda, "Ultra-high precision angle measurement technology," (in Japanese), *Journal of the Society of Instrument and Control Engineers*, vol. 47, no. 9, pp. 720–725, 2008.

後藤雅彦　Masahiko GOTO
インダストリアルソリューションズ事業部
開発・技術統括部 第三開発・技術部
3rd Development & Engineering Department
Development & Engineering Sector
Industrial Solutions Business Unit

阿部　桂　Kei ABE
インダストリアルソリューションズ事業部
開発・技術統括部 第三開発・技術部
3rd Development & Engineering Department
Development & Engineering Sector
Industrial Solutions Business Unit

千代晋平　Shimpei SENDAI
インダストリアルソリューションズ事業部
開発・技術統括部 第三開発・技術部
3rd Development & Engineering Department
Development & Engineering Sector
Industrial Solutions Business Unit

山本拓巳　Takumi YAMAMOTO
インダストリアルソリューションズ事業部
開発・技術統括部 第三開発・技術部
3rd Development & Engineering Department
Development & Engineering Sector
Industrial Solutions Business Unit

常盤圭佑　Keisuke TOKIWA
インダストリアルソリューションズ事業部
開発・技術統括部 第三開発・技術部
3rd Development & Engineering Department
Development & Engineering Sector
Industrial Solutions Business Unit


後藤雅彦
Masahiko GOTO


阿部　桂
Kei ABE


千代晋平
Shimpei SENDAI


山本拓巳
Takumi YAMAMOTO


常盤圭佑
Keisuke TOKIWA

研究開発論文

Research and Development Reports

指向性エネルギー堆積法による Ni625合金の造形プロセスウィンドウ

恵久春佑寿夫，中林拓頌，藤原朋春，Behrang Poorganji

Processing Windows of Ni625 Alloy Fabricated using Direct Energy Deposition†

Yusufu EKUBARU, Takuya NAKABAYASHI, Tomoharu FUJIWARA and Behrang POORGANJI

本研究では，ニコン製 Lasermeister レーザー粉末指向性エネルギー堆積（LP-DED）装置を用いた Ni625合金の造形プロセスウィンドウを確立した．プロセスマップは，微細構造と機械的特性の間の相関関係を調べることによって確立された，レーザー出力，スキャン速度，および有効エネルギー密度の関係を示す．全てのサンプルは等軸および柱状デンドライト粒からなる二峰性の微細構造を示し，デンドライトアーム間隔は走査速度の増加に伴い減少した．各サンプルの引張特性はわずかな変動を示し，その値は過去の報告値と同等であった．引張強度および降伏強度は，それぞれ1008 ± 2から 941 ± 9 MPa，682 ± 11から 640 ± 7 MPa の範囲であった．本研究は，様々なパラメータセットにわたる Ni625合金の優れた造形性を実証し，各材料および装置に対して単一の理想的なプロセス条件は存在せず，代わりに同様の結果を得るために複数の「レシピ」を使用できることを示している．

Herein, a process window is developed for Ni625 alloy fabricated using a Nikon Lasermeister laser powder direct energy deposition (LP-DED) unit.

The process map illustrates the relationship between the laser power, scan speed, and effective energy density, established by examining the correlation between the microstructure and mechanical properties. All samples exhibit a bimodal microstructure comprising equiaxed and columnar dendrite grains, and the dendrite arm spacing decreases with increasing scan speed. The tensile behavior of each sample demonstrates minimal variation, and the values are comparable to those reported previously. The ultimate tensile and yield strengths range from 1008 ± 2 to 941 ± 9 and 682 ± 11 to 640 ± 7 MPa, respectively. This study highlights the remarkable manufacturability of Ni625 alloy for additive manufacturing across diverse parameter sets, demonstrating that a single ideal process set does not exist for each material and machine. Instead, multiple “recipes” may be employed to achieve similar outcomes.

Key words 積層造形，レーザー粉末指向性エネルギー堆積法，インコネル625，シミュレーション，微細構造
additive manufacturing, laser powder direct energy deposition, Inconel 625, simulation, microstructure

1 Introduction

Metal additive manufacturing (AM) is an excellent technology for part fabrication, offering distinct advantages over conventional manufacturing methods. With significant cost and lead-time reductions and the capability to develop complex geometrical features [1]–[3], metal AM has rapidly garnered interest from key industries such as aerospace, automotive, military, and biomedical sectors [3]–[5]. Metal AM entails various techniques, including material jetting, sheet lamination, laser powder bed fusion, binder jetting, and direct energy deposition.

Laser powder direct energy deposition (LP-DED) presents unique advantages over other AM processes, including alloy design, repair capabilities, surface modifications, and the synthesis of large-scale components with adequate dimensional accuracy [6]. These capabilities have been increasingly demonstrated and recognized in various fields, particu-

† This paper uses the following copyrighted work with modifications (*).
Yusufu EKUBARU, Takuya NAKABAYASHI, Tomoharu FUJIWARA, and Behrang POORGANJI, “Processing Windows of Ni625 Alloy Fabricated Using Direct Energy Deposition” Adv. Eng. Mater. 2024, 2400962. (https://doi.org/10.1002/adem.202400962)
© 2024 EKUBARU *et al*. This is an open-access article under the terms of the Creative Commons Attribution License, which permits use, distribution and reproduction in any medium, provided the original work is properly cited.
* Main content of the modifications
The title, abstract, and author are translated into Japanese, and both English and Japanese are printed.

larly in the aerospace industry [4]. The in-situ alloying of elemental powders offers an effective alternative to the use of pre-alloyed powders, which are cost- and time-intensive to produce using traditional atomization methods. By mixing pure elemental powders of Ni, Cr, Mo, Nb, and Fe, Wang *et al.* [7] demonstrated the high-quality fabrication of Ni625 alloy components using LP-DED and in situ alloying. Wilson *et al.* [8], [9] repaired defective voids in turbine blades, illustrating the effectiveness of LP-DED in repair. These studies highlight the adaptability of DED to a wide range of defective parts, as well as its capabilities in repair and maintenance. Balla *et al.* [10] applied a tantalum coating onto titanium using LP-DED, a notable achievement considering the extremely high melting point (>3000°C) of Ta, which poses challenges for traditional melt-cast methods. Ta-coated Ti exhibits favorable interactions with bone cells, indicating promising biocompatibility. Gradl *et al.* [1], [2], [11] utilized LP-DED to manufacture a large-scale rocket nozzle for aerospace applications. The growing recognition of LP-DED is reflected in the significant increase in the number of patents and scientific publications dedicated to this technology, highlighting its importance in academia and industry [5], [12].

Furthermore, the anticipation of an expanding market for AM has spurred intense competition among AM machine manufacturers, resulting in the development of various AM systems [4]. In this context, Nikon Advanced Manufacturing Business Unit in Japan developed an LP-DED system named Lasermeister. Extensive empirical testing has been conducted on this machine with common AM materials, including Fe-, Ni-, and Ti-based alloys. Herein, we present our latest research findings, particularly focusing on the Ni625 alloy, also referred to as Alloy 625 or Inconel 625.

The Ni625 alloy has been utilized in various industries, including petrochemical, aerospace, chemical, marine, and nuclear sectors, due to its excellent strength and high corrosion and fatigue resistance [12], [13]. Moreover, its remarkable weldability has attracted considerable attention in AM, where it has been successfully produced using various process parameters in LP-DED, including laser power (P) (220–1500 W) and scan speed (V) (8.3–33.3 mm/s), with the corresponding effective energy density (E_D) ranging from 14 to 66 J/mm^2 [7], [13]–[20].

The solidification microstructure of AM-produced Ni625 alloy is complex, featuring fine dendrites, micro-segregated elements, and various solidification phases [21]. The nickel-based superalloy, primarily strengthened by the solid hardening effects of refractory elements including niobium and molybdenum within a nickel-chromium matrix exhibits a face-centered cubic (FCC) structure [14]. These alloys are sensitive to the precipitation of strengthening intermetallic phases, including stable ordered FCC ($L1_2$) γ'-Ni_3Al; metastable body-centered tetragonal γ''-Ni_3Nb; stable orthorhombic d-Ni_3Nb; carbides (MC, M_6C); and intergranular brittle Laves phases ((Nb, Mo)(NiCrFe)$_2$) in the interdendritic region [1], [12]–[14]. The formation of these phases, particularly the Laves phases, consumes significant amounts of Nb and Mo, thereby reducing their content in the matrix, which diminishes solid solution and precipitation strengthening effects [19]. Further, the Laves phase induces crack nucleation and propagation, significantly deteriorating creep rupture properties and ductility [19]. Consequently, manufacturing components with reduced elemental segregation and fewer Laves phases has become critical.

The mechanical properties of materials are primarily influenced by factors such as porosity, grain size, the behavior of precipitates, and dendrite spacing [25]. Generally, the mechanical properties can be improved by reducing their size, which essentially means creating a finer microstructure. Reducing porosity can enhance the material's strength and durability as fewer pores mean less space for cracks to initiate. Smaller grain sizes often lead to increased hardness and strength due to the Hall-Petch relationship. Controlling the behavior of precipitates, such as reducing their size, can increase the material's strength as smaller precipitates more effectively hinder dislocation movement [25], [26]. Lastly, smaller dendrite spacing can contribute to a more homogeneous microstructure, reducing segregation and enhancing various mechanical properties [25], [26]. One fundamental approach to achieving a finer microstructure is to increase the cooling rate, and it can be accomplished by using a smaller P, a higher V, or a combination of both [27].

Based on this background, this study aimed to a) develop the process windows for Ni625 alloy using the Lasermeister system and b) establish a process window that expresses the relationship between P, V, and E_D based on a series of simulations and experiments focusing on microstructural properties and mechanical performance.

This research demonstrated for the first time that using lower P values and smaller hatch spacings can significantly enhance the strength of Ni625 alloys by promoting substantial microstructure miniaturization. Additionally, DED process "recipes" for Ni625 in the lower P region were developed. These results are expected to significantly contribute to the DED fabrication of components such as precise, large, thin-walled structures that are vulnerable to thermal deformation, as well as the automation of gas turbine blade

repairs, among other applications.

Table 1 Chemical composition (wt%) of Ni625 alloy

Powder	Ni	Cr	Mo	Nb + Ta	Fe	Al	Ti	C	Mn
Inconel625	Bal.	20–23	8–10	3.15–4.15	≤ 5	≤ 0.4	≤ 0.4	≤ 0.03	≤ 0.01

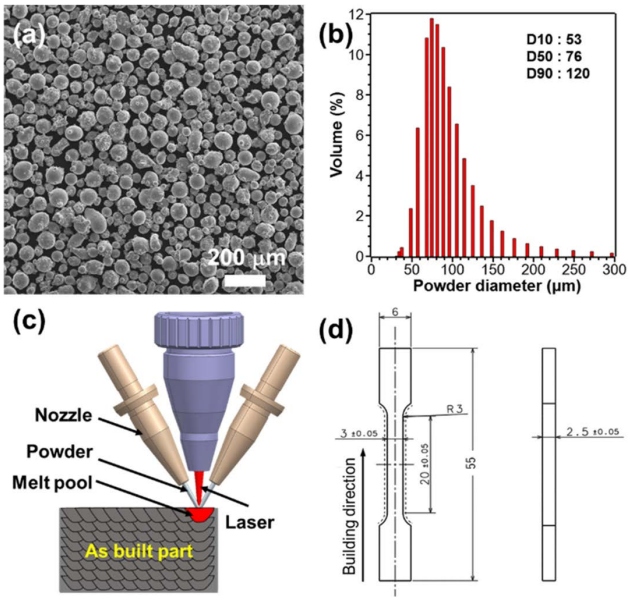

Fig. 1 (a) Morphology and (b) powder size distribution of the Ni625 alloy powders used in LP-DED (c) Schematic of LP-DED and (d) dimensions of the tensile test sample

2 Experimental Section

2.1. Ni625 Alloy Fabrication

Ni625 alloy powders were procured from Carpenter Additive Inc.; and their compositions and morphologies are summarized in Table 1 and Fig. 1, respectively. An LP-DED unit (Lasermeister 100A) with a 915 nm 200 W laser diode module and a beam diameter (d) of 0.5 mm was utilized to fabricate the Ni625 alloy samples (Fig. 1 (c)). Two samples, namely, a 10 mm × 10 mm × 10 mm cube and a 10 mm × 10 mm × 55 mm rectangle, were fabricated along the x-, y-, and z-axes on a SUS304 substrate via the XY scanning strategy. Cubic samples were used for microstructural analysis, whereas rectangular samples were employed for tensile property testing (Fig. 1 (d)) [7], [20]. The parameter values used for the experiment are listed in Table 3, where the laser hatch spacing was maintained at 0.2 mm.

2.2. Microstructure Characterization and Mechanical Properties

Samples were cut from the substrate via electrical discharge machining to analyze their microstructures and mechanical properties. The YZ cross sections were first mechanically polished using emery paper up to a 4000 grade and subsequently chemically polished with colloidal silica to achieve mirror-polished sections for microstructural examination.

Optical microscopy (VHX8000, KEYENCE, Osaka, Japan) and scanning electron microscopy (SEM; SU1500, Hitachi High-Tech Corporation, Tokyo, Japan) were conducted to examine the microstructures. The bulk samples fabricated by the LP-DED Lasermeister were characterized via X-ray diffraction (XRD; RINT2500,Rigaku Corporation, Tokyo, Japan) with Cu-Kα radiation at room temperature (RT). Crystallographic texture and elemental segregation were investigated using electron backscattered diffraction (EBSD) and energy-dispersive X-ray spectroscopy (EDS), respectively, with a scanning electron microscope (JSM-7900F,JEOL Ltd., Tokyo, Japan). A tensile test (TGI-50KN, MinebeaMitsumi Inc., Nagano, Japan) was conducted at RT, where the loading axis was parallel to the build direction (BD). The test was conducted thrice for each sample, and the results were averaged.

2.3. Simulations

The formation mechanism of the microstructure induced by LP-DED was explored through simulations focusing on thermal behavior and solidification characteristics. The thermal behavior calculations provided insights into the temperature distribution and the shape and size of the melt pool (MP). Conversely, analyzing the solidification characteristics aided in understanding the development of grains, which could manifest as either equiaxed dendrites (ED) or columnar dendrites (CD).

These simulations were performed using the commercial software FLOW-3D v12.0 for a region measuring 10 mm × 7 mm × 3 mm in the X, Y, and Z directions. The region was discretized into a structural Eulerian mesh with a size of 0.025 mm.

2.3.1. Heat Source Model

$$q_{in} = \left(\frac{P_0}{\pi r_b^2}\right)\exp\left\{-\left(\frac{r}{r_b}\right)^2\right\} - h_c\left(T - T_0\right) \quad (1)$$

where P_0 is the laser power (100/120/160 W), r is the distance from the beam center, r is the laser radius (0.25 mm), r_b is the effective laser radius (0.1 mm), h_c is the heat transfer coefficient (9.5 W/m^2 K) [28], T is the temperature, and T_0 is the ambient temperature (298 K).

2.3.2. Powder Model

We employed the Lagrangian particle tracking method to model the powder particles. Particles entering the melt pool

transformed into liquid cells upon surpassing the melting point. The amount of powder injected was calculated from the predetermined powder utilization efficiency. The powder was injected at a constant velocity from the vertical direction of the melt pool to ensure the melting of all particles.

2.3.3. MP Flow Governing Equations

The governing equations, which include mass, momentum, and energy conservation, are expressed in (2), (3), and (4), respectively.

$$\frac{\partial \rho}{\partial t} + \nabla \cdot \rho v = R_{SOR} \tag{2}$$

$$\frac{\partial \boldsymbol{v}}{\partial t} + (\boldsymbol{v} \cdot \nabla) v = -\frac{1}{\rho}\nabla p + \frac{\mu}{\rho}\nabla^2 v + g - \frac{R_{SOR}}{\rho}(\boldsymbol{v} - \boldsymbol{v}_p) \tag{3}$$

$$\frac{\partial (\rho I)}{\partial t} + \nabla \cdot (\rho I \boldsymbol{v}) = -p\nabla \cdot v + k\nabla^2 T + I_{SOR} \tag{4}$$

$$I = C_v T + (1 - f_s) L \tag{5}$$

where ρ is density, t is time, v is flow velocity, R_{SOR} is the amount of mass source due to powder particles, p is pressure, m is viscosity, v_p is particle velocity, Cv is specific heat, fs is the solidus rate, I_{SOR} is the discharge of energy, and L is latent heat. The thermophysical parameters were calculated using the thermodynamic database of JmatPro (Sente Software) considering their temperature dependencies (Table 2).

2.3.4. Solidification Parameter

The temperature gradient G and solidification velocity R represent spatial temperature variations and are expressed as:

$$\varepsilon = \left| \frac{T_s - T_L}{t_s - t_L} \right| \tag{6}$$

$$G = \nabla T \tag{7}$$

$$R = \frac{\varepsilon}{|\boldsymbol{G}|} \tag{8}$$

where e is the cooling rate, T_S is the solidus line temperature (1398 K), T_L is the liquidus line temperature (1613 K), t_S is the time below the solidus line temperature, t_L is the time below the liquidus line temperature, and ∇ is the differential operator.

3 Results

3.1. Simulated Data

The aspect ratio (D/W), indicating the depth (D) to width (W) ratio of the MP, was assessed in both the experimental and simulated scenarios to verify the simulation model. Fig. 2 displays the results of the single-track experiments and simulations at V values of 5 and 10 mm/s, with constant P and powder feeding rate (Q) values of 120 W and 3 g/min, respectively. The experimental dimensions of the MP were measured from the optical images, whereas the simulated sizes of the MP were determined by identifying a black solidus line on the temperature contour map. The aspect ratios decreased with increasing V, and the experimental aspect ratios were slightly higher than the simulated ones, with differences of < 10%. It is considered that one possible reason for this difference is the thermal boundary conditions of the

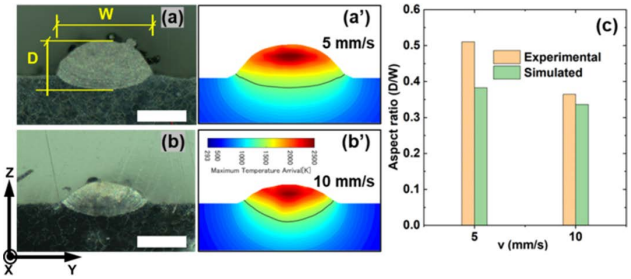

Fig. 2 Comparison of the experimental and simulated MP: (a) and (b) experimental optical images, (a') and (b') simulated temperature contours, and (c) aspect ratio
Scale bars: 200 mm

Table 2 Thermophysical properties of Ni625 calculated using JmatPro

Temperature intervals T (K)	Thermal conductivity k (W/(m K))	Specific heat Cv (J/(kg K))	Density r (kg/m^3)	Viscosity m (kg/(m s))	Surface tension s (N/m)	Latent heat of fusion L (kJ/kg)
298	10.8	406	8474	-	-	210
600	15.9	456	8373	-	-	
900	20.9	504	8253	-	-	
1200	25.8	559	8117	-	-	
1500	30.1	713	7931	1.39×10^{-2}	1.84	
1800	31.4	737	7499	0.62×10^{-2}	1.74	
2100	35.8	745	7235	0.38×10^{-2}	1.62	
2400	40.2	748	6952	0.26×10^{-2}	1.52	

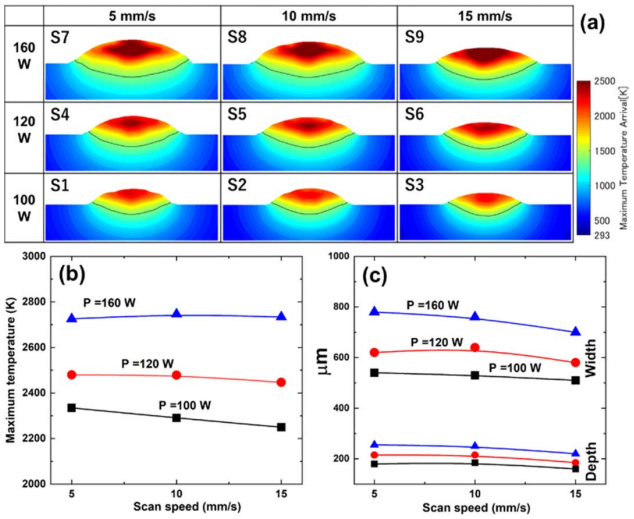

Fig. 3 Simulated MP of (a) temperature contour plot, (b) maximum temperature, and (c) dimensions at varying process parameters

substrate in the simulation. Hence, this model was employed for additional simulations to generate a process map for the Ni625 alloy.

Various conditions were simulated to assess fabrication feasibility using these process parameters. Fig. 3 illustrates the simulated temperature contour plots and the maximum temperature of the MPs under nine different conditions, accompanied by their respective sizes. As shown in Figs. 3(b) and 3(c), with an increase in P from 100 to 160 W (while V is constant at 5 mm/s), the maximum temperature increases from 2335 to 2725 K, and the width of the MPs increases from 540 to 780 mm; by contrast, increasing V when P is constant causes both the maximum temperature and the width and depth of the MPs to remain almost constant. The highest temperatures and dimensions of the MPs indicated a significant dependence on P but less dependence on V. Consequently, MPs were formed under all conditions, and the maximum temperature exceeded the melting point of the Ni625 alloy at 1623 K [29], which allowed us to proceed with the experiments.

3.2. Microstructural Analysis

The fabricated state, porosity, and cracks of the samples produced under the nine simulated conditions were investigated via cross-sectional image analysis using an optical microscope. All samples, except S7, were successfully manufactured, as shown in Fig. 4(a); however, S7 could not be completed because the powder adhered to the nozzle owing to the highest energy density input. The optical density shown in Fig. 4(b) was measured from optical images of the polished surfaces of the samples. Five images were taken

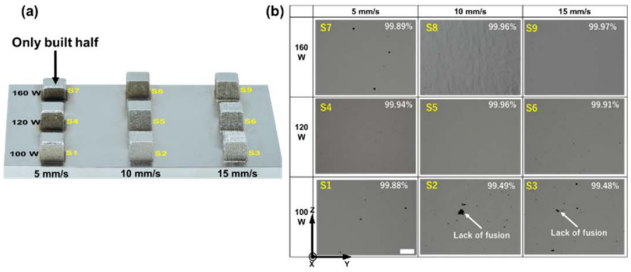

Fig. 4 (a) Appearance of the LP-DED fabricated samples and (b) optical density

from different locations on the polished surface of each sample at 200X magnification. The optical density of these images was then measured using ImageJ software, and the average was calculated. As shown in Fig. 4(b), most samples, excluding S2 and S3, exhibited a dense structure without any visible cracks; this resulted in a satisfactory industrial density of over 99.5% [3], [30], [31]. However, samples S2 and S3 showed noticeably lower density values with irregularly shaped pores caused by the lack of fusion owing to the lower energy density input. It can be generally observed that densification increases with increasing P and decreases with increasing V. This behavior is more significant in samples S1 to S3 at 100 W, while it is less pronounced in samples S4 to S9 at 120 W and 160 W. This suggests that at lower P settings, the impact of V on densification is more pronounced, whereas at higher P settings, the effect of V becomes less significant. Consequently, optimizing P and V parameters is crucial for achieving desired densification levels in different samples.

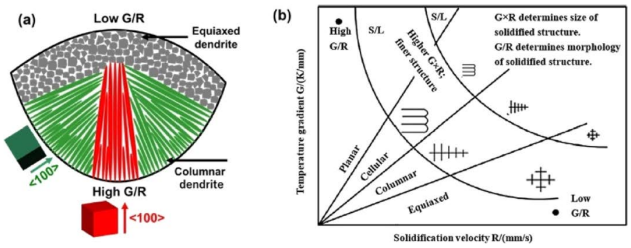

Fig. 5 (a) Schematic of the MP microstructure and (b) columnar-equiaxed transition criteria, adapted from [27] with permission [27], [32], [33]

The microstructure of AM materials can be explained by the MP microstructure using Hunt's columnar-equiaxed transition criteria [27], [32], [33]. As shown in Fig. 5(a), MPs typically exhibit a bimodal microstructure comprising two types of grains: ED at the top with no preferential crystallographic orientation and CD at the bottom that show a preference for growing from the bottom part to the center along the direction of the thermal gradient [21], [33]–[35]. This is attributed to the higher G/R ratio at the bottom part of the MP and the lower G/R ratio at the top, as illustrated in Fig. 5(b), where

G/R is the grain morphology factor determining either ED or CD, and G × R is the cooling rate that determines the size of the grain. Typically, the extremely high G and G × R values in the AM process foster directional solidification, and enhance the textures of the microstructures of alloys [36], [37].

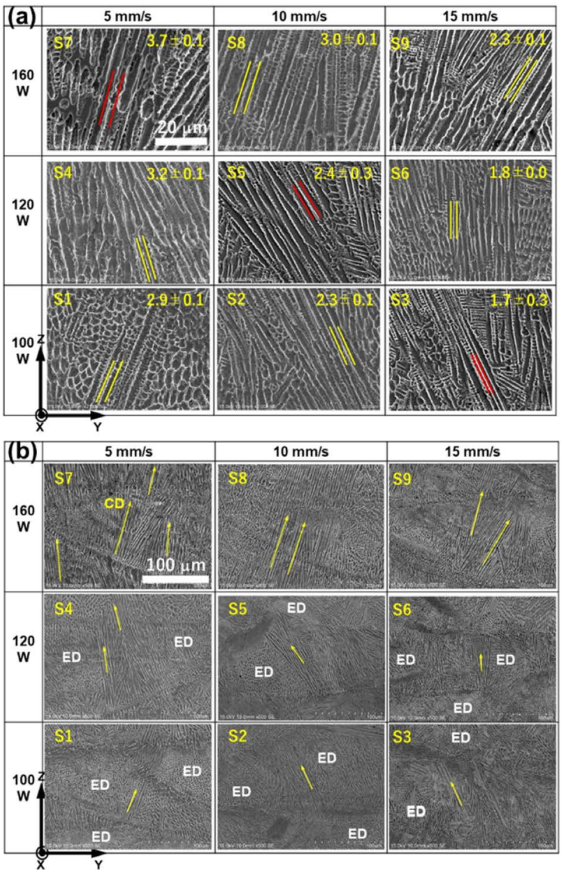

Fig. 6 SEM images of the YZ plane of the samples with (a) higher magnitudes containing PDAS and (b) lower magnitudes containing CD and ED regions

The dendrite microstructural features, including the PDAS size and shape of the grains of the samples, were characterized by observing the SEM images of the aqua regia-etched YZ cross-section. PDAS is one of the factors in influencing mechanical properties and it was known that smaller PDAS increases various mechanical properties [25], [26]. As shown in Fig. 6(a), among the samples, S7 yielded the highest PDAS with a value of 3.7 ± 0.1 mm, while S3 yielded the lowest PDAS with a value of 1.7 ± 0.3 mm; consequently, the PDAS increased as the P increased and V decreased. In contrast, as shown in Fig. 6(b), all samples exhibited a bimodal grain microstructure consisting of CD and ED regions. Samples S7 to S9, fabricated with the highest P of 160 W, exhibited a predominance of CD, while samples S1 to S3, fabricated with the lowest P of 100 W, displayed an almost exclusive ED presence, and resulted in a trend that shifted from an ED-dominant to CD-dominant microstructure with increasing P and decreasing V, respectively; namely, high P values increased the dendrite structure, which is consistent with other research [14].

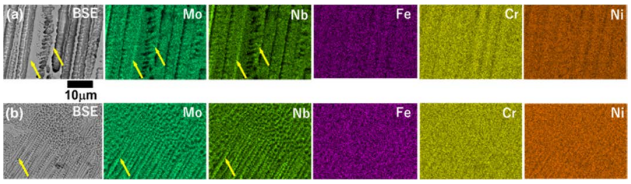

Fig. 7 EDS maps of samples of (a) S7 and (b) S3

The elemental microsegregation of the samples was analyzed using EDS mapping. Figs. 7(a) and 7(b) illustrate the distributions of the main elements (Ni, Cr, Fe, Nb, and Mo) in samples S7 (with the highest energy density) and S3, respectively. The Mo and Nb contents in the interdendritic regions were higher than those in the dendritic regions, as indicated by the yellow arrow. Both samples exhibited significant Mo and Nb segregation with no clear differences in their segregation behaviors. Based on the obtained results and previous reports, it can be concluded that the observed phase corresponds to the Laves phase [7], [16], [19]

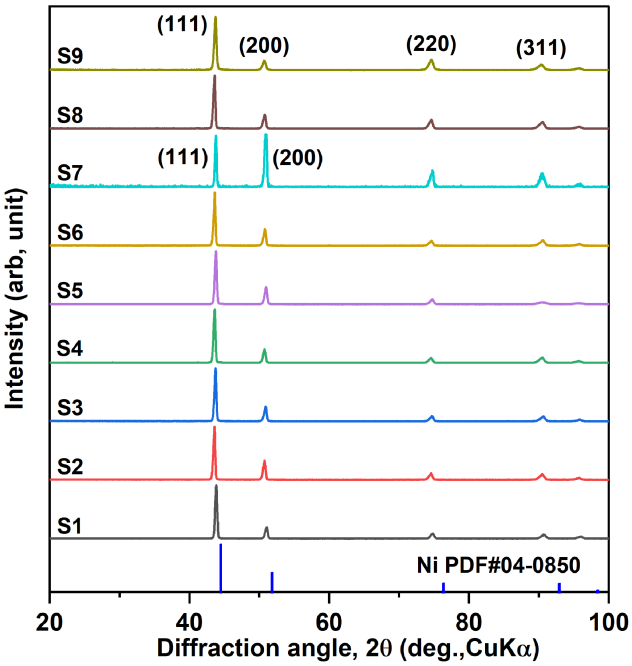

Fig. 8 XRD patterns of the LP-DED fabricated samples

XRD analysis was conducted on the polished YZ cross-section of the samples to confirm the phase states. As shown in Fig. 8, all the samples exhibited peaks corresponding to the reference Ni (PDF #04-0850) in the XRD analysis. Interestingly, in sample S7, the relative intensities of the (111) and (200) peaks were similar, even though (111) has the highest-intensity peak, indicating that (100) tends to be oriented in the BD (z-direction), which is in agreement with

other studies [3], [7], [38], [39]. However, all samples exhibited a minor peak shift to a lower diffraction angle compared with Ni (PDF #04-0850), implying the presence of residual stress in the samples [3], [38].

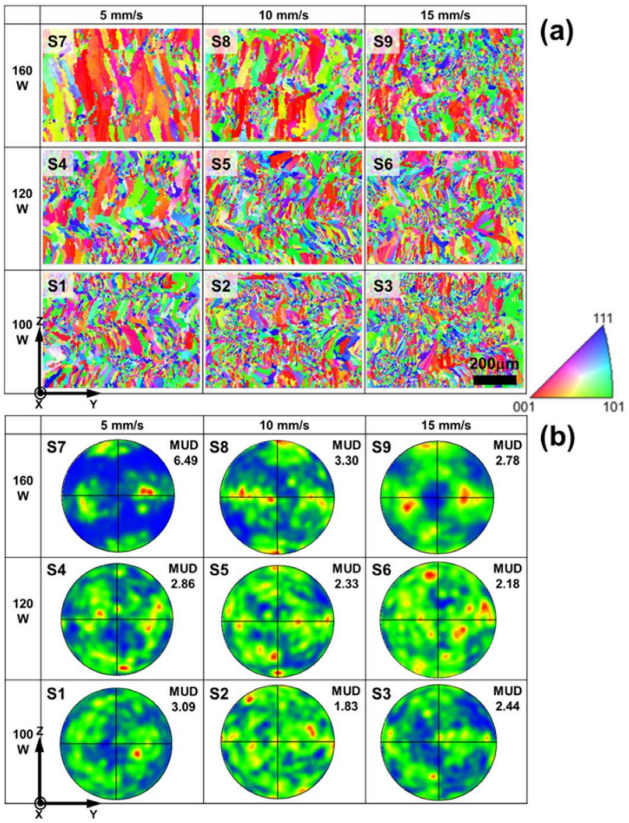

Fig. 9 EBSD (a) inverse pole figure maps and (b) the corresponding {001} pole figures with multiples of uniform distribution (MUD) values of the YZ plane

One of the key features of AM that influences the mechanical properties is the crystallographic texture [36], which was investigated using EBSD. As shown in Fig. 9 (a), by increasing P and decreasing V, directional grain growth occurs along the z-direction with a {100} crystallographic orientation, which is an easy growth direction for the FCC crystal structure [3], [36], which was observed in the samples. The values of the texture strength measure, MUD, increased as P increased and V decreased; however, apart from sample S7, no distinguishable crystallographic textures were observed for the samples, and S7 exhibited the highest texture with most grains aligned in the {100} crystallographic orientation; this finding is consistent with the XRD results shown in Fig. 8.

3.3. Tensile Properties

A tensile test was performed at RT, and the results showed trends corresponding to the features of the microstructure. As shown in the optical images in Fig. 4, the porosity

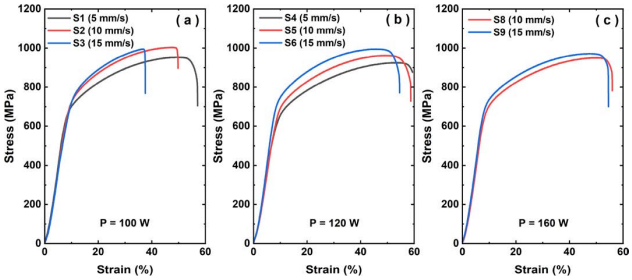

Fig. 10 Tensile stress-strain curves of the samples

increased with V in the sample fabricated at the lowest P of 100 W, whereas the elongation (El) of these samples decreased, as shown in Fig. 10(a). However, with an increase in V, the minor decreases in the PDAS and grain size shown in Figs. 6 and 9 led to a minor monotonic increase in the ultimate tensile strength (UTS) for the samples produced at P = 120 W and 160 W. Consequently, the tensile properties exhibited negligible variations because fewer changes were observed in the microstructure.

3.4. Process Window

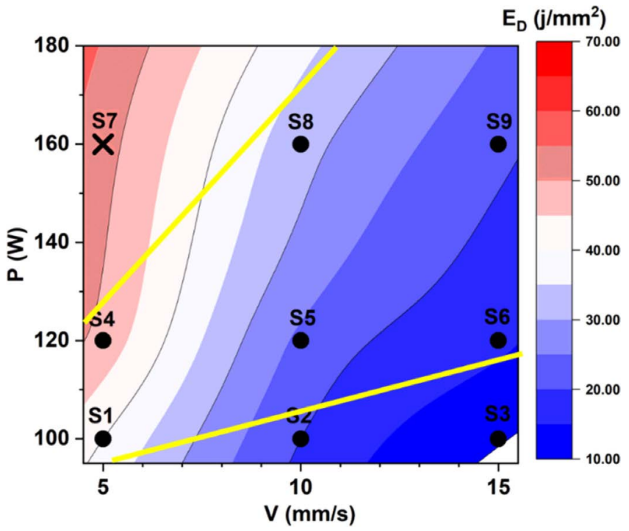

Fig. 11 P–V process map with E_D contour

A process map illustrating the relationship between P, V, E_D and the feasibility of sample fabrication was established based on the experimental data obtained in this study. Fig. 11 illustrates that the pink region represents high E_D, while the blue region represents low E_D. Additionally, samples S2 and S3, located in the low E_D area, exhibited higher porosity owing to insufficient fusion. Conversely, sample S7, situated in the high E_D area, was not fully produced because of powder adhesion in the nozzle. Consequently, the approximate optimal region is indicated by a yellow line.

4 Discussion

4.1. Pore Formation and Mechanical Property Impact

Pores are one of the major defects that significantly affect the mechanical properties of parts; which can primarily occur owing to both high- or low-energy input, as well as the insufficient overlap of laser tracks [40].

High-energy input during the melting process can result in the formation of an unstable MP at extremely high temperatures and severe Marangoni convection, which in turn leads to the generation of spherical pores either by trapping the protective gas (Ar) or metallic vapor [3], [40]. As shown in Fig. 4(b), samples S7 and S1 fabricated with a higher energy density showed spherical pores with a maximum diameter of 40 mm. These pores were primarily formed owing to the trapping of Ar gas and were unlikely attributed to metallic vapor because of the high melting points of all the main elements of the Ni625 alloy. It is known that spherical pores with diameters < 130 μm have negligible detrimental effects on the mechanical properties of the material [3]. Moreover, as illustrated in Fig. 10(a), sample S1 displayed satisfactory tensile properties, despite the presence of spherical pores.

Low-energy input cannot completely melt the metallic powder in the previously deposited layer, thus leading to irregularly shaped lack of fusion pores, as shown in Fig. 4(b). Samples S2 and S3 produced with lower energy input contained irregularly shaped pores with sizes over 100 mm; these samples exhibited lower elongation tensile properties, as shown in Fig. 10(a).

Insufficient overlap among laser tracks can also cause a lack of fusion pores, which may be attributed to a large hatch distance and/or layer thickness [40]. However, in this study, the primary cause of the lack of fusion pores was identified as low-energy input, predominantly due to low P.

4.2. Effects of P and V on Grain Size and Morphology

P and V are the primary process parameters used to adjust the energy density to tailor the microstructure, and they significantly affect the MP solidification process parameters G and R [27], [32], [33]. Therefore, a comprehensive understanding of G and R is crucial for predicting or explaining the microstructural features observed in experimental samples, and simulations are an effective tool for their calculation [27], [41], [42].

As shown in the solidification map in Fig. 5(b), G × R is the cooling rate that determines the size of the grain, whereas (G/R) is the morphology factor that determines the shapes of the grains. In this study, a maximum cooling rate of 3.5×10^4 K/s was achieved for sample S3, which is close to the intrinsic cooling rate of LP-DED, which ranges from 10^3 to 10^4 K/s [21].

At increasing P and decreasing V values, the PDAS increased while the grain shapes shifted from being predominantly ED-dominant to CD-dominant, as shown in Fig. 6(b). It is believed that these behaviors can be attributed to the changes in G × R and G/R, as illustrated in Fig. 12.

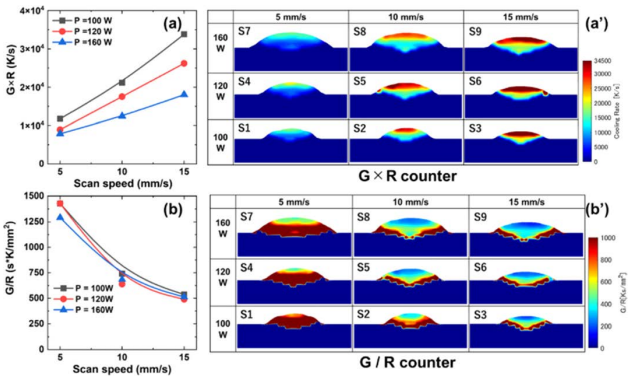

Fig. 12 Simulated (a) average G × R and (a') G × R contours, and (b) average G/R and (b') G/R contours

As shown in Fig. 12(a), the impact of P on G × R is minor at low V values but becomes significant at high V. Therefore, the G × R values of the samples are almost the same at V = 5 mm/s, and the PDASs of these samples do not change significantly, as shown in Fig. 6(a). Conversely, G × R increased as a function of V as also proven by other researchers [27], [41], [42], and the highest and lowest G × R values were obtained for S3 and S7, respectively; accordingly, S3 and S7 respectively exhibited the lowest and highest PDAS values equal to 1.7 ± 0.3 mm and 3.7 ± 0.1 mm, as shown Fig. 6(a).

As shown in Fig. 12(b), G/R is less affected by P but is significantly affected by V; additionally, G/R decreases as V increases, thus suggesting that CD increases with decreasing V. Correspondingly, the directional grain growth along the z-direction with the {100} crystallographic orientation is most significant in the samples with the lowest V of 5 mm/s, as shown in Fig. 9.

As shown in Figs. 12(a') and 12(b'), higher G/R and lower G × R values are observed at the bottom of the MP; in contrast, lower G/R and higher G × R were obtained at the top of the MP [27], [41], [42] and these behaviors are most significant at low V, thus indicating that the morphology of the microstructure is prone to CD. Correspondingly, the texture strength measure MUDs were higher in fabricated samples with the lowest V, as shown in Fig. 9.

4.3. Verification of Tensile Properties

Although there were no dramatic differences in the tensile behavior of each sample in this study, the results were still comparable to the tensile results from other existing studies. As illustrated in Fig. 13 and as listed in Table 3, the UTS and yield strengths (YS) of samples exhibited minor changes, with UTS changing from 1008 ± 2 to 941 ± 9 MPa and YS changing from 682 ± 11 to 640 ± 7 MPa. However, in the samples fabricated with the lowest P of 100 W, the elongation noticeably decreased as V increased owing to the higher porosity caused by the lack of fusion, as shown in Fig. 4. Conversely, according to the reference data in Table 3, it is known that the Ni625 alloy can be fabricated using a broad range of process parameters (for example, P may change from 220 to 1500 W and V from 8.3 to 33.3 mm/s) yielding higher tensile properties than casting.

In addition, based on the literature data listed in Table 3, the UTS decreases at increasing P. A higher P not only increases the evaporation [21] of Al, Cr, Fe, and Co in the Ni625 alloy by increasing the MP temperature, but also accelerates precipitation growth owing to a lower cooling rate, thus leading to a degradation of mechanical properties. Therefore, using P values as small as possible is advantageous for the microstructure and mechanical properties of the material and machine maintenance. In this study, tensile properties similar to those reported in other research studies [7],[13],[14],[18] were obtained by using a lower P combination with a small hatch space, as shown in Fig. 13. A small hatch space increases remelting, which reduces the lack of fusion [43] and increases the ED grains [3].

This study is believed to be the first report on the optimization of the strength and ductility of Ni625 alloys using a relatively low P value, thus demonstrating that high-performance Ni625 alloys can also be fabricated with lower P.

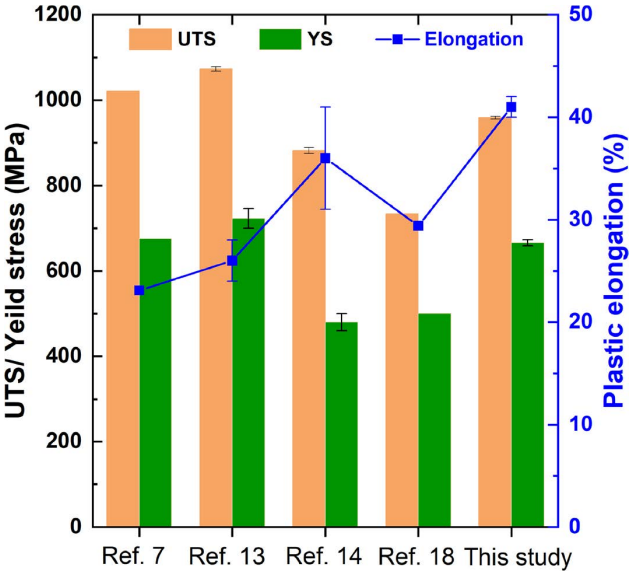

Fig. 13 Comparison of tensile properties in this study with those obtained in other research studies

5 Conclusion

Extensive empirical testing on the Lasermeister was performed with common AM materials, including Fe-, Ni-, and Ti-based alloys. Herein, to develop process maps for the Ni625 alloy specific to this machine, the processability, microstructure, and mechanical properties of the alloy were experimentally and numerically investigated under various

Table 3 Comparison of process parameters and tensile properties in this study with those obtained in references

Label	*P* (W)	*V* (mm/s)	*Q* (g/min)	*d* (mm)	$E_D = P/(Vd)$ (J/mm^2)	UTS (MPa)	YS (MPa)	El (%)
S1	100	5.0	2.0	0.5	40.0	951 ± 7	655 ± 15	42 ± 2
S2	100	10.0	4.0	0.5	20.0	1008 ± 2	682 ± 11	36 ± 1
S3	100	15.0	4.0	0.5	13.3	1005 ± 7	674 ± 13	28 ± 4
S4	120	5.0	2.0	0.5	48.0	941 ± 9	640 ± 7	42 ± 2
S5	120	10.0	4.0	0.5	24.0	959 ± 3	666 ± 7	41 ± 1
S6	120	15.0	4.0	0.5	16.0	989 ± 4	669 ± 12	37 ± 1
S7	160	5.0	2.0	0.5	64.0	-	-	-
S8	160	10.0	4.0	0.5	32.0	944 ± 4	670 ± 10	42 ± 1
S9	160	15.0	4.0	0.5	21.3	960 ± 6	672 ± 9	40 ± 1
[7]	220	8.3	2.3	0.4	66.0	1020.9	675.8	23.1
[14]	330	33.3	7.0	0.4	14.1	1073 ± 5	723 ± 23	26 ± 2
[15]	500	12.5	2.5	1.2	33.3	882 ± 7	480 ± 20	36 ± 5
[19]	1500	15.0	7.5	5	20.0	733.7	500.4	29.4
[29]	Casting	485.0	275.0	25.0				

fabrication parameters. Key findings include:

1. A simulation model was established to predict the MP thermal history, including the dimensions and G and R rates.
2. The dimensions and highest temperatures of the MP were considerably affected by P but less affected by V, leading to high P values and increased size and maximum temperature of the MP.
3. Fully dense Ni625 alloy parts (> 99.5%) were fabricated under conditions where P was > 100 W and V was in the range of 5–15 mm/s.
4. As P increased and V decreased, a corresponding increase in the dendritic structure and texture was observed. Notably, the sample synthesized with the highest P value of 160 W and lowest V value of 5 mm/s exhibited the most pronounced dendritic structure and texture.
5. A positive correlation was observed between the microstructure and tensile properties with lower elongations for finer microstructures. In particular, sample S3, which had the finest microstructure and highest porosity, exhibited the lowest elongation.
6. P ranged from 100 to 160 W, V varied between 5 and 15 mm/s, and a corresponding process map for E_D was established.
7. The samples showed tensile strength values comparable to those in other research studies, with UTS and YS ranging from 1008 ± 2 to 941 ± 9 MPa and from 682 ± 11 to 640 ± 7 MPa, respectively.

This study demonstrated that a combination of lower P values and smaller hatch spacings can effectively strengthen Ni625 alloys. It was also found that there several parameters can be set to achieve similar outcomes. Indeed, these findings pave the way for the formulation of various "recipes" in the future tailored to the shape and complexity of different parts, thus opening new avenues for part development.

Acknowledgment. The experimental assistance and invaluable discussions with Takashi Sugizaki (Nikon Corp. Advanced Technology Research & Development Materials & Advanced Research Laboratory) and Daizo Saito (Hikari Glass Co.,Ltd.) are highly appreciated.

References

[1] P. R. Gradl, T. Teasley, C. Protz, C. Katsarelis, and P. Chen, "Process Development and Hot-fire Testing of Additively Manufactured NASA HR-1 for Liquid Rocket Engine Applications," in *Proc. 2021 AIAA Propuls. Energy Forum*, Aug. 2021.

[2] P. R. Gradl, C. Protz, and T. Wammen, "Additive manufacturing development and hot-fire testing of liquid rocket channel wall nozzles using blown powder directed energy deposition inconel 625 and jbk-75 alloys," in *Proc. 2019 AIAA Propuls. Energy Forum Expo.*, Aug. 2019.

[3] Y. Ekubaru *et al.*, "Excellent strength-ductility balance of Sc-Zr-modified Al-Mg alloy by tuning bimodal microstructure via hatch spacing in laser powder bed fusion," *Mater. Des.*, vol. 221, 110976, 2022.

[4] D. Svetlizky *et al.*, "Directed energy deposition (DED) additive manufacturing: Physical characteristics, defects, challenges and applications," *Mater. Today*, vol. 49, pp. 271–295, 2021.

[5] D. Svetlizky *et al.*, "Laser-based directed energy deposition (DED-LB) of advanced materials," *Mater. Sci. Eng. A*, vol. 840, 142967, 2022.

[6] A. Bandyopadhyay, K. D. Traxel, M. Lang, M. Juhasz, N. Eliaz, and S. Bose, "Alloy design via additive manufacturing: Advantages, challenges, applications and perspectives," *Mater. Today*, vol. 52, pp. 207–224, 2022.

[7] J. Wang, Y. Wang, Y. Su, and J. Shi, "Evaluation of in-situ alloyed Inconel 625 from elemental powders by laser directed energy deposition," *Mater. Sci. Eng. A*, vol. 830, 142296, 2022.

[8] T. Ünal-Saewe, L. Gahn, J. Kittel, A. Gasser, and J. H. Schleifenbaum, "Process development for tip repair of complex shaped turbine blades with IN718," *Procedia Manuf.*, vol. 47, pp. 1050–1057, 2020.

[9] J. M. Wilson, C. Piya, Y. C. Shin, F. Zhao, and K. Ramani, "Remanufacturing of turbine blades by laser direct deposition with its energy and environmental impact analysis," *J. Clean. Prod.*, vol. 80, pp. 170–178, 2014.

[10] V. K. Balla, S. Banerjee, S. Bose, and A. Bandyopadhyay, "Direct laser processing of a tantalum coating on titanium for bone replacement structures," *Acta Biomater.*, vol. 6, no. 6, pp. 2329–2334, 2010.

[11] P. R. Gradl and C. S. Protz, "Technology advancements for channel wall nozzle manufacturing in liquid rocket engines," *Acta Astronaut.*, vol. 174, pp. 148–158, 2020.

[12] S. P. Kumar, S. Elangovan, R. Mohanraj, and J. R. Ramakrishna, "A review on properties of Inconel 625 and Inconel 718 fabricated using direct energy deposition," *Mater. Today Proc.*, vol. 46, pp. 7892–7906, 2021.

[13] A. Poudel, P. R. Gradl, S. Shao, and N. Shamsaei, "Tensile deformation behavior of laser powder direct energy deposited Inconel 625: Cryogenic to elevated temperatures," *Mater. Sci. Eng. A*, vol. 889, 145826, 2024.

[14] J. Nguejio, F. Szmytka, S. Hallais, A. Tanguy, S. Nardone, and M. G. Martinez, "Comparison of microstructure features and mechanical properties for additive manufactured and wrought nickel alloys 625," *Mater. Sci. Eng. A*, vol.

764, 138214, 2019.

[15] M. Rombouts, G. Maes, M. Mertens, and W. Hendrix, "Laser metal deposition of Inconel 625: Microstructure and mechanical properties," *J. Laser Appl.*, vol. 24, no. 5, 052007, 2012.

[16] Y. L. Hu, Y. L. Li, S. Y. Zhang, X. Lin, Z. H. Wang, and W. D. Huang, "Effect of solution temperature on static recrystallization and ductility of Inconel 625 superalloy fabricated by directed energy deposition," *Mater. Sci. Eng. A*, vol. 772, 138711, 2020.

[17] G. Marchese *et al.*, "Characterization and Comparison of Inconel 625 Processed by Selective Laser Melting and Laser Metal Deposition," *Adv. Eng. Mater.*, vol. 19, no. 3, 1600635, 2017.

[18] Y. L. Hu, X. Lin, X. B. Yu, J. J. Xu, M. Lei, and W. D. Huang, "Effect of Ti addition on cracking and microhardness of Inconel 625 during the laser solid forming processing," *J. Alloys Compd.*, vol. 711, pp. 267–277, 2017.

[19] Y. L. Hu *et al.*, "Effect of solution heat treatment on the microstructure and mechanical properties of Inconel 625 superalloy fabricated by laser solid forming," *J. Alloys Compd.*, vol. 767, pp. 330–344, 2018.

[20] R. Savinov, Y. Wang, and J. Shi, "Evaluation of microstructure, mechanical properties, and corrosion resistance for Ti-doped inconel 625 alloy produced by laser directed energy deposition," *Mater. Sci. Eng. A*, vol. 884, 145542, 2023.

[21] N. K. Adomako, N. Haghdadi, and S. Primig, "Electron and laser-based additive manufacturing of Ni-based superalloys: A review of heterogeneities in microstructure and mechanical properties," *Mater. Des.*, vol. 223, 111245, 2022.

[22] G. P. Dinda, A. K. Dasgupta, and J. Mazumder, "Laser aided direct metal deposition of Inconel 625 superalloy: Microstructural evolution and thermal stability," *Mater. Sci. Eng. A*, vol. 509, no. 1–2, pp. 98–104, 2009.

[23] Z. Tian *et al.*, "A review on laser powder bed fusion of inconel 625 nickel-based alloy," *Appl. Sci.*, vol. 10, no. 1, 81, 2020.

[24] D. K. Gorai and T. K. Kundu, "Density Functional Theory Study of Structural and Electronic Properties of γ'-Ni3Al and γ-Ni3Nb," *IOP Conf. Ser. Mater. Sci. Eng.*, vol. 338, no. 1, 012041, 2018.

[25] J. M. V. Quaresma, A. Carlos, and A. Garcia, "Correlation between unsteady-state solidification conditions, dendrite spacings, and mechanical properties of Al-Cu alloys," *Metall. Mater. Trans. A Phys. Metall. Mater. Sci.*, vol. 31, no. 12, pp. 3167–3178, 2000.

[26] K. S. Cruz, E. S. Meza, F. A. P. Fernandes, J. M. V. Quaresma, L. C. Casteletti, and A. Garcia, "Dendritic arm spacing affecting mechanical properties and wear behavior of Al-Sn and Al-Si alloys directionally solidified under unsteady-state conditions," *Metall. Mater. Trans. A Phys. Metall. Mater. Sci.*, vol. 41, no. 4, pp. 972–984, 2010.

[27] J. Shao, G. Yu, X. He, S. Li, R. Chen, and Y. Zhao, "Grain size evolution under different cooling rate in laser additive manufacturing of superalloy," *Opt. Laser Technol.*, vol. 119, 105662, 2019.

[28] Y. Chen, Y. Yan, and B. Li, "Thermal Analyses of Power Electronics Integrated with Vapour Chamber Cooling," *Automot. Innov.*, vol. 3, no. 4, pp. 328–335, 2020.

[29] B. K. A. Kumar, M. G. Ananthaprasad, and K. Gopalakrishna, "Action of Cryogenic chill on Mechanical properties of Nickel alloy Metal Matrix Composites," *IOP Conf. Ser. Mater. Sci. Eng.*, vol. 149, no. 1, 012116, 2016.

[30] O. Gokcekaya *et al.*, "Effect of scan length on densification and crystallographic texture formation of pure chromium fabricated by laser powder bed fusion," *Crystals*, vol. 11, no. 1, pp. 1–14, 2021.

[31] Y. Ekubaru, O. Gokcekaya, and T. Nakano, "Effects of Scanning Strategy on the Microstructure and Mechanical Properties of Sc-Zr-Modified Al-Mg Alloy Manufactured by Laser Powder Bed Fusion," *Crystals*, vol. 12, no. 10, 1348, 2022.

[32] T. DebRoy *et al.*, "Additive manufacturing of metallic components-Process, structure and properties," *Prog. Mater. Sci.*, vol. 92, pp. 112–224, 2018.

[33] W. Zhao *et al.*, "The columnar to equiaxed transition of CoCrNi medium-entropy alloy fabricated by laser directed energy deposition," *Mater. Des.*, vol. 237, 112538, 2024.

[34] Z. Zhou, L. Huang, Y. Shang, Y. Li, L. Jiang, and Q. Lei, "Causes analysis on cracks in nickel-based single crystal superalloy fabricated by laser powder deposition additive manufacturing," *Mater. Des.*, vol. 160, pp. 1238–1249, 2018.

[35] Z. Tong *et al.*, "Laser additive manufacturing of FeCrCoMnNi high-entropy alloy: Effect of heat treatment on microstructure, residual stress and mechanical property," *J. Alloys Compd.*, vol. 785, pp. 1144–1159, 2019.

[36] O. Gokcekaya, T. Ishimoto, S. Hibino, J. Yasutomi, T. Narushima, and T. Nakano, "Unique crystallographic texture formation in Inconel 718 by laser powder bed fusion and its effect on mechanical anisotropy," *Acta Mater.*, vol. 212, 116876, 2021.

[37] S. H. Sun, K. Hagihara, T. Ishimoto, R. Suganuma, Y. F. Xue, and T. Nakano, "Comparison of microstructure, crystallographic texture, and mechanical properties in Ti-15Mo-5Zr-3Al alloys fabricated via electron and laser beam powder bed fusion technologies," *Addit. Manuf.*, vol. 47, 102329, 2021.

[38] Y. L. Hu *et al.*, "Plastic deformation behavior and dynamic recrystallization of Inconel 625 superalloy fabricated by directed energy deposition," *Mater. Des.*, vol. 186, 108359,

2020.

[39] R. J. Vikram, A. Singh, and S. Suwas, “Effect of heat treatment on the modification of microstructure of selective laser melted (SLM) IN718 and its consequences on mechanical behavior,” *J. Mater. Res.*, vol. 35, no. 15, pp. 1949–1962, 2020.

[40] J. N. Zhu, E. Borisov, X. Liang, E. Farber, M. J. M. Hermans, and V. A. Popovich, “Predictive analytical modelling and experimental validation of processing maps in additive manufacturing of nitinol alloys,” *Addit. Manuf.*, vol. 38, 101802, 2021.

[41] M. S. Pham, B. Dovgyy, P. A. Hooper, C. M. Gourlay, and A. Piglione, “The role of side-branching in microstructure development in laser powder-bed fusion,” *Nat. Commun.*, vol. 11, no. 1, 749, 2020.

[42] Z. Gan, G. Yu, X. He, and S. Li, “Numerical simulation of thermal behavior and multicomponent mass transfer in direct laser deposition of Co-base alloy on steel,” *Int. J. Heat Mass Transf.*, vol. 104, pp. 28–38, 2017.

[43] L. E. dos Santos Paes, M. Pereira, F. A. Xavier, W. L. Weingaertner, and L. O. Vilarinho, “Lack of fusion mitigation in directed energy deposition with laser (DED-L) additive manufacturing through laser remelting,” *J. Manuf. Process.*, vol. 73, pp. 67–77, 2022.

恵久春佑寿夫　Yusufu EKUBARU
アドバンストマニュファクチャリング事業部 第二開発部
2nd Development Department
Advanced Manufacturing Business Unit

中林拓頌　Takuya NAKABAYASHI
先進技術開発本部 数理技術研究所
Mathematical Sciences Research Laboratory
Advanced Technology Research & Development

藤原朋春　Tomoharu FUJIWARA
アドバンストマニュファクチャリング事業部 第二開発部
2nd Development Department
Advanced Manufacturing Business Unit

Behrang POORGANJI
Morf3D Inc.

均質および不均質な細胞における幾何学的手法による力推定の適用可能性の数値評価

宮坂　翔，和泉啓太，奥田　覚，三木裕一朗

Numerical Assessment of the Applicability of Geometry-based Force Inference on Homogeneous and Heterogeneous Cells†

Shou MIYASAKA, Keita IZUMI, Satoru OKUDA and Yuichiro MIKI

細胞に作用する力は，細胞の形態，増殖，分子発現解析など，さまざまな重要な生物学的特性に影響を及ぼすことが知られている．その力を測定することは，従来の細胞評価手法に代わる可能性を秘めており，医学的細胞診断や細胞培養研究において重要な役割を果たすことが期待されている．特に医学的細胞評価においては，非侵襲的で特殊な装置を必要としない力推定手法が注目を集めている．その中でも石原らが提案した，細胞の幾何学的形状のみに基づいて密集した細胞に作用する力を推定する手法は有望な方法として注目されている．しかしながら，その手法の適用範囲は現時点で十分には解明されていない．そこで本研究では，シミュレーションモデルである 2 次元バーテックスモデルを用いて，均質および不均質な細胞系に対するこの推定手法の適用可能性を数値的に評価した．数値シミュレーションから得られた真値と推定手法による推定値を比較した結果，均質な細胞系において推定精度と細胞の真円度との間に有意な相関が認められた．さらに，不均質な細胞系においても，この手法が十分に適用可能であることを確認した．本研究の結果は，力推定手法を医学的細胞評価に適用する際に有用な知見を提供するものであり，今後の細胞診断や細胞培養研究の発展に寄与するものと考えている．

The measurement of cellular forces, which reflect crucial biological attributes, has the potential to replace conventional cell assessment methods, such as morphology, proliferation, and molecular expression analysis, in medical cell diagnosis and cell culture studies. In medical cell evaluations, force inference techniques have gained prominence due to their non-invasiveness and lack of requirement for specialized equipment. Among those techniques, the method proposed by Ishihara *et al.*, which estimates forces in densely packed cells based only on cell geometry, is a promising method. However, its applicability range of this method has not been fully established. In this study, we employed a two-dimensional vertex model to numerically assess the applicability of this method on homogeneous and heterogeneous cells. Our comparisons between the true values from numerical simulations and the estimated values from the inference method revealed a significant correlation between estimation accuracy and cell roundness in systems of homogeneous cell. Moreover, the method demonstrated efficient force estimations in heterogeneous-cell systems. These findings may be useful when the force inference method is employed to evaluate medical cells.

Key words 力推定，細胞評価，バーテックスモデル，医療応用，細胞組織力学
force estimation, cell assessment, vertex model, medical application, tissue mechanics

1 Introduction

In medical cell diagnosis and cell culture studies, intracellular forces, which reflect biological properties, have the potential to replace conventional cell assessment methods, such as morphology, proliferation, and molecular expression analysis. For instance, the mechanical properties of cells can be used to identify senescent cells, which are characterized

† This paper uses the following copyrighted work with modifications (*).
Miyasaka S, Izumi K, Okuda S, Miki Y (2024) Numerical assessment of the applicability of geometry-based force inference on homogeneous and heterogeneous cells. PLoS ONE 19(4): e0299016. https://doi.org/10.1371/journal.pone.0299016
Copyright: © 2024 Miyasaka *et al.* This is an open access article distributed under the terms of the Creative Commons Attribution License, which permits unrestricted use, distribution, and reproduction in any medium, provided the original author and source are credited.
* Main content of the modifications
The title, abstract, and author are translated into Japanese, and both English and Japanese are printed.

by a stable cell cycle arrest induced in response to stress [1]. This chronic inflammatory state fosters a pro-tumorigenic microenvironment, promoting cancer initiation, migration, and metastasis. The in vivo detection of senescence necessitates the examination of fixed or deep-frozen tissues, as in the immunohistochemical analysis of frozen samples [2]. However, there is considerable clinical demand for real-time bioimaging techniques. Senescent cells exhibit enhanced mechanical maturity at adhesion points, leading to the transmission of greater traction forces to the substrate. Consequently, the detection of senescent cells can be achieved by observing alterations to their cell morphology [3] or quantifying the mechanical forces they generate. There are numerous other instances where the state of a cell and the mechanical stress exerted on it are closely related [4], [5].

Many approaches have been proposed for investigating the mechanical properties of cells. These approaches can be divided into two types: one involves applying force directly to cells and measuring the amount of cell deformation as an equivalent of the force on a cell [5], [6], while the other involves non-invasive measuring physical or chemical indices that are indirectly related to cellular forces [7], [8]. Despite the efficacy of these methods, their invasiveness, expense associated with the preparation of specialized platforms, and limited throughput pose substantial challenges for practical applications, such as cell assessment [9].

In order to address these challenges, numerical inference methods have attracted attention. Such methods estimate tension at cell-cell boundaries and intracellular pressure under the assumption of force equilibrium among cells [9] – [12]. Specifically, the approach proposed by Ishihara *et al.* [9] uses Bayesian statistics to deal with the indeterminacy inherent in the estimation process [9], [10], [13], [14]. This non-invasive technique does not require specialized equipment and can be readily integrated with a conventional microscope. However, its applicability to actual cell evaluation has limitations. The validation of this method has focused on a limited set of parameters for homogeneous cells using Drosophila wing cells as a model. Thus, to expand its application to cells utilized in medical cell evaluation, such as human cells, it is essential to widen the scope of validation.

In this study, we investigate the applicability of the force inference method proposed by Ishihara *et al.* [9]. To achieve this, we apply the method to the cell morphologies derived from numerical simulations using a two-dimensional (2D) vertex model and assess the dependence of estimation accuracy on cell behavior by comparing simulated and estimated forces. Furthermore, by analyzing the correlation between estimation accuracy and cell morphology, we identify the conditions under which the inference method has high accuracy. Based on these results, we discuss the applicability of the inference method for homogeneous and heterogeneous cells.

2 Methods

To assess the applicability of the force inference method proposed by Ishihara *et al.* [9], we conducted numerical simulations utilizing a 2D vertex model and then applied the inference method to the cell morphologies derived from the model. In this approach and model, cells are presumed to be densely packed and are represented as simplified polygonal shapes with straight edges. An overview of the force inference method and a description of the 2D vertex model are given in the following sections.

2.1. Force Inference

The force inference method estimates the tension at cell-cell boundaries and intracellular pressure by solving the force balance equation at each vertex (Fig. 1(a)). The position vector of the i-th vertex is denoted by $\boldsymbol{r}_i$. If there are n_i vertices connected to the i-th vertex through edges, the forces acting on the i-th vertex in the x and y directions are given by

$$\begin{aligned} f_i^x &= \sum_{j=1}^{n_i} \frac{x_j - x_i}{|\boldsymbol{r}_j - \boldsymbol{r}_i|} T_j + \sum_{j=1}^{n_i} \frac{y_{(j \bmod n_i)+1} - y_j}{2} P_j, \\ f_i^y &= \sum_{j=1}^{n_i} \frac{y_j - y_i}{|\boldsymbol{r}_j - \boldsymbol{r}_i|} T_j + \sum_{j=1}^{n_i} \frac{x_{(j \bmod n_i)+1} - x_j}{2} P_j, \end{aligned} \tag{1}$$

where i identifies the vertex, T_j is the tension on the j-th edge, and P_j is the pressure of the j-th cell adjacent to both the j-th and $(j + 1)$-th edges. Considering Eq. (1) for all vertices in the system, the vector $\mathbf{F}\left(=\left(f_1^x, f_1^y, f_2^x, f_2^y, \ldots\right)\right)$ containing all xy elements of the forces can be written as

$$\mathbf{F} = \mathbf{AS}, \tag{2}$$

where $\mathbf{S}$ $(= (T_1, T_2, \ldots, P_1, P_2, \ldots))$ is the matrix that summarizes the edge tension and cell pressure to be estimated and $\mathbf{A}$ is the matrix that summarizes the coefficients that reflect cell morphologies. Since the cell deformation process is quasi-static under the low Reynolds number assumption, the tensions and pressures are balanced at each vertex. Thus, the force balance equation can be formulated as

$$\mathbf{AS} = \mathbf{0}. \tag{3}$$

A Bayesian estimation technique is used to solve Eq. (3). Specifically, the prior function is assumed to be a Gaussian

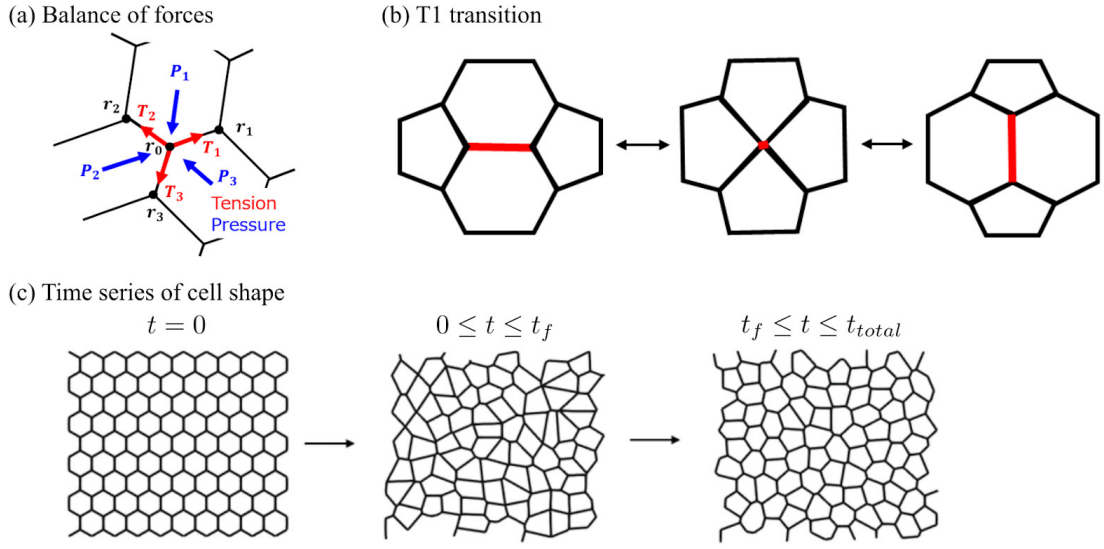

Fig. 1 Numerical simulation using a 2D vertex model

(a) Diagram of forces around vertex in 2D vertex model: Blue arrows represent intracellular pressure toward the vertex and red arrows represent tension at cell-cell boundaries. (b) Illustration of T1 transition implemented in 2D vertex model: The left and right cells approach each other. When the length of the edge shown in red becomes shorter than a certain threshold, the cells acquire a common edge and top and bottom cells separate. (c) Flow of 2D vertex model: In the period $0 \le t \le t_f$ the system is relaxed by adding a fluctuation term to the line tension. In the period $t_f \le t \le t_{total}$, the system is transformed to a steady state to minimize energy by removing the fluctuation term.

distributed around some positive tension value. The hyper-parameter, which represents the ratio of the variance of the prior function to that of the likelihood, is calculated by maximizing the marginal likelihood. The estimation of **S** is then accomplished by maximizing the posterior distribution. Further details regarding this inference method are described in previous studies [9], [10].

2.2. Acquisition of Stress Field using 2D Vertex Model

To evaluate the accuracy of the force inference method, numerical simulations were conducted using a 2D vertex model [15]. The simulations were performed on a system that contained 100 cells confined within a box measuring 10 units in the x and y directions. Periodic boundary conditions were applied to all boundaries. The motion of each cell was expressed through vertex movements under quasi-static conditions and rearrangements between cells were expressed through the T1 transition (Fig. 1(b)) by reconnecting edge connections based on vertex movements [16]. The reconnection was performed when the edge length became shorter than the threshold, $l_{T1} = 0.05$, a value chosen to be small enough to affect the calculation of cell morphology. In the vertex model, the cell morphologies were determined by minimizing the potential energy of the system. The cellular network was sufficiently relaxed before the calculation to avoid local minima. In this section, the validation of the force inference method using the simulation results and details of the simulation procedure are discussed first, and the applied parameter settings are presented later.

In the static state, the mechanical force balance of cell configurations can be represented by a potential energy function [17]. The potential energy is defined as

$$U \equiv \sum_i^{\text{cell}} \frac{K}{2}\left(s_i - s_{\text{eq}}\right)^2 + \sum_i^{\text{cell}} \frac{\Gamma_i}{2} p_i^2 + \sum_j^{\text{edge}} \Lambda_j l_j, \tag{4}$$

where s_i is the area of the i-th cell, p_i is the perimeter of the i-th cell, l_j is the length of the j-th edge, the first term represents the area elasticity, the second term represents the perimeter elasticity, and the third term represents the line tension. The area elastic modulus K, the preferred area s_{eq}, and the perimeter elasticity Γ_i are parameters that determine the mechanical behavior of the system. The perimeter elasticity Γ_i is randomly assigned to each cell according to a Gaussian distribution with mean μ_Γ and standard deviation σ_Γ. The line tension Λ_j is affected by the actin-myosin contractile force at cell-cell boundaries. The pressure of the i-th cell and the tension at the j-th edge in the static state are calculated as

$$\begin{aligned} P_i &= -\frac{\partial U}{\partial \mathrm{s}} = -K\left(s_i - s_{eq}\right) \\ T_j &= -\frac{\partial U}{\partial l} = \Gamma_i p_i + \Gamma_{i+1} p_{i+1} + \Lambda_j, \end{aligned} \tag{5}$$

where p_i and p_{i+1} are the perimeters of the i-th and $(i + 1)$-th cells, including the j-th edge, respectively.

To compare the estimated values with the true values, the true and estimated tension values were scaled by their respective scaling factors in accordance with a previous study [9]. For example, for the estimated values, the scaling factor, denoted by c, was determined as $c = 1/\overline{T_{\mathrm{est}}}$, where $\overline{T_{\mathrm{est}}}$ is the mean value of the estimated tension. The scaling factors were chosen such that the average tension values were equal to 1. The true and estimated pressures were scaled using the same factor c to ensure that the average pressure values were 0; that is, $\tilde{P}_{\mathrm{est}} = cP_{\mathrm{est}} + \Delta p$, where $\Delta p = -c\overline{P_{\mathrm{est}}}$ and $\overline{P_{\mathrm{est}}}$ is the mean value of the estimated pressure. Using the scaled true and estimated values, we calculated the estimation accuracy in terms of the root-mean-squared error (RMSE) σ_{est} as

$$\sigma_{\mathrm{est}} \equiv \sqrt{\frac{\sum_i^{n_{\mathrm{cell}}} \left(\tilde{P}_{\mathrm{est}\,i} - \tilde{P}_{\mathrm{true}\,i}\right)^2 + \sum_j^{n_{\mathrm{edge}}} \left(\tilde{T}_{\mathrm{est}\,j} - \tilde{T}_{\mathrm{true}\,j}\right)^2}{n_{\mathrm{cell}} + n_{\mathrm{edge}}}}, \tag{6}$$

where $\tilde{P}_{\mathrm{est}\,i}$ and $\tilde{P}_{\mathrm{true}\,i}$ are the scaled estimated and true pressures, respectively, for the i-th cell, n_{cell} is the number of cells, $\tilde{T}_{\mathrm{est}\,j}$ and $\tilde{T}_{\mathrm{true}\,j}$ are the scaled estimated and true tensions, respectively, for the j-th edge, and n_{edge} is the number of edges.

The cell morphology and force in the static state were obtained by calculating vertex movements:

$$\eta \frac{d\mathbf{r}_i}{dt} = -\nabla U, \tag{7}$$

where η is the friction coefficient. The numerical integration of Eq. (7) was conducted using the first-order Euler method with time step Δt. Topological reconnection of edges was carried out when the edge length was less than the threshold value, l_{T1}.

To obtain a system state with potential energy near the global minimum, simulations using the annealing method were performed. Two distinct processes were carried out in sequence. First, a fluctuation process was calculated, in which the fluctuation of the line tension Λ_j in Eq. (8) was incorporated during the period $0 \le t \le t_f$. Second, a relaxation process was calculated, in which the fluctuation was gradually reduced during the period $t_f < t \le t_{total}$ (Fig. 1(c)). The line tension Λ_j is written as

$$\Lambda_j = \begin{cases} \Lambda_j^c + \omega_j & \text{if } \ 0 \le t \le t_f \\ \Lambda_j^c + \omega_j \exp(-t) & \text{if } \ t_f < t \le t_{\mathrm{total}} \end{cases}, \tag{8}$$

where the constant Λ_j^c represents the actin-myosin contractile force. Its value varied across cell-cell boundaries according to a Gaussian distribution, $\Lambda_j^c \sim N(\mu_\Lambda, \sigma_\Lambda^2)$, where μ_Λ and σ_Λ denote the mean and standard deviation, respectively. The variable ω_j is colored noise with time correlation. Its time evolution is given by

Table 1 List of constants and variables used in 2D vertex model

Parameter	Description	Set value	Unit
dt	Time step	0.01	η/K
t_{total}	Total simulation time	2000	η/K
t_{in}	Time interval for intercalation	50	η/K
s_{eq}	Ideal area	1.0	1
l_0	Length of one side of initial cell	0.62	$\sqrt{s_{eq}}$
p_{eq}	Ideal perimeter	3.7	$\sqrt{s_{eq}}$
l_{T1}	Limit length for T1 transition	0.05	$\sqrt{s_{eq}}$
C_{T1}	Correlation factor of length after T1 transition	1.5	−
η	Friction coefficient of vertex	1.0	1
K	Area elastic modulus	1.0	1
Γ	Perimeter elasticity	Control	Ks_{eq}
μ_Γ	Mean of perimeter elasticity	Control	Ks_{eq}
σ_Γ	Standard deviation of perimeter elasticity	Control	Ks_{eq}
Λ	Line tension	Control	$K(s_{eq})^{3/2}$
μ_Λ	Mean of constant tension term Λ^c	Control	$K(s_{eq})^{3/2}$
σ_Λ	Standard deviation of constant tension term Λ^c	0.05	$K(s_{eq})^{3/2}$
t_f	Term used to set thermal fluctuation	1000	η/K
τ_f	Relaxation time of tension fluctuation term ω	20.0	η/K
σ_f	Coefficient in fluctuation term	10.0	$K(s_{eq})^{3/2}$

Table 2 Typical ranges of parameters with "Control" as set value in Table 1

Parameter	Range
Γ	0.05–0.20
μ_Γ	0.05–0.20
μ_Λ	−1.4–0.5
σ_Λ	0.01–0.04

$$\frac{d\omega_j(t)}{dt} = -\frac{1}{\tau_j}\omega_j(t) + \xi_j. \tag{9}$$

where ξ_j is white noise according to a Gaussian distribution, $\xi_j \sim N\left(0, \sigma_f^2 / \tau_f^2\right)$, where σ_f and τ_f denote the amplitude and correlation time of ω_j, respectively [18], [19].

Table 1 presents the physical and numerical parameters utilized in the simulations using the 2D vertex model. The unit length was set to $\sqrt{s_{\mathrm{eq}}}$, the unit energy was set to Ks_{eq}^2, and the unit time was set to η/K. The parameters Γ, μ_Γ, σ_Γ, and μ_Λ are control parameters that reflect a heterogeneous cellular system; their respective ranges are shown in Table 2.

3 Results

To comprehensively investigate the applicability of the force inference method, we conducted two distinct analyses. First, we assessed the accuracy of the estimated cell behavior in a system with homogeneous cells. Numerical simulations using the 2D vertex model were performed to obtain cell morphologies, as well as the tension at cell-cell boundaries and cell pressure, within a wide range of parameter values. The force inference method was then applied to the simulated cell morphologies to estimate the tension and cell pressure. In addition, estimation accuracy was calculated for each parameter set by comparing the forces obtained from the simulations and estimations. Second, we examined the applicability of the inference method to a system with heterogeneous cells.

3.1. Dependence of Estimation Accuracy on Cell Behaviors

First, the inference method was applied to the cell morphologies obtained from numerical simulations of homogeneous cells. Figure 2(a) shows the parameter dependence of estimation accuracy in terms of the RMSE defined in Eq. (6), where a smaller value indicates higher accuracy. The heat map in the figure shows that the accuracy increases with increasing perimeter elasticity and line tension. The RMSE as a function of Λ and Γ is plotted in Fig. 2(b1, b2), respectively; the RMSE increases nonlinearly with decreasing either Λ or Γ. We define the condition with an RMSE of 0.2 or less as the high-accuracy condition, corresponding to the parameter region above the solid line in Fig. 2(a). The threshold of RMSE is defined as the result of two-segmented linear regression applied to the plots in Fig. 2(b1, b2) as follows. The points within each of those plots are divided into two groups based on a specific value of Λ or Γ. For each group, a regression line is obtained using the least squares method, and the grouping is performed to minimize the sum of the residuals of these regression lines. The RMSE value of the intersection point of these two regression lines is extracted for the plot. This process is carried out for all the plots in Fig. 2(b1, b2), and the largest RMSE value is defined as the threshold.

3.2. Correlation between Estimation Accuracy and Characteristics of Cell Morphology

We examined the relationship between cell morphology and estimation accuracy by analyzing the dependence of cell morphology on the line tension Λ and perimeter elasticity Γ. Following a previous study [17], we divided the parameter space into three regions based on the ground state of the energy function (Eq. (4)), as shown by the dashed line in Fig. 2(a). We then compared cell morphology and estimation accuracy (Fig. 2(d1-d4)) as well as the true and estimated force values under four typical conditions, namely $(\Lambda, \Gamma) = (-0.8, 0.11)$ (Fig. 2(c1)), $(\Lambda, \Gamma) = (-0.3, 0.11)$ (Fig. 2(c2)), $(\Lambda, \Gamma) = (-0.3, 0.16)$ (Fig. 2(c3)), and $(\Lambda, \Gamma) = (0.1, 0.04)$ (Fig. 2(c4)). For the first condition, where the estimation accuracy is low, the cell shapes tend to be elongated and have multiple configurations that can form at the energy minimum. In contrast, for the other conditions, where the estimation accuracy is relatively high, the cell shapes tend to be relatively round.

For a more quantitative understanding of the relationship, we computed several characteristic cell morphologies for each parameter set (Fig. 3(a1-a3)) and compared them with the estimation accuracy (Fig. 3(b1-b3)). The dependence of circularity ($4\pi s/p^2$) on the line tension Λ and perimeter elasticity Γ is shown in Fig. 3(a1). The circularity increases with increasing either Λ or Γ. By comparing this heatmap and Fig. 2(a), we obtained the circularity dependence of estimation accuracy (Fig. 3(b1)). For the scatter plot, the regression line is obtained using the least squares method, and the circularity value of the intersection between this regression line and the line of the RMSE threshold is defined as the circularity threshold: 0.82. Moreover, the results for the perimeter are shown in Fig. 3(a2, b2). As a

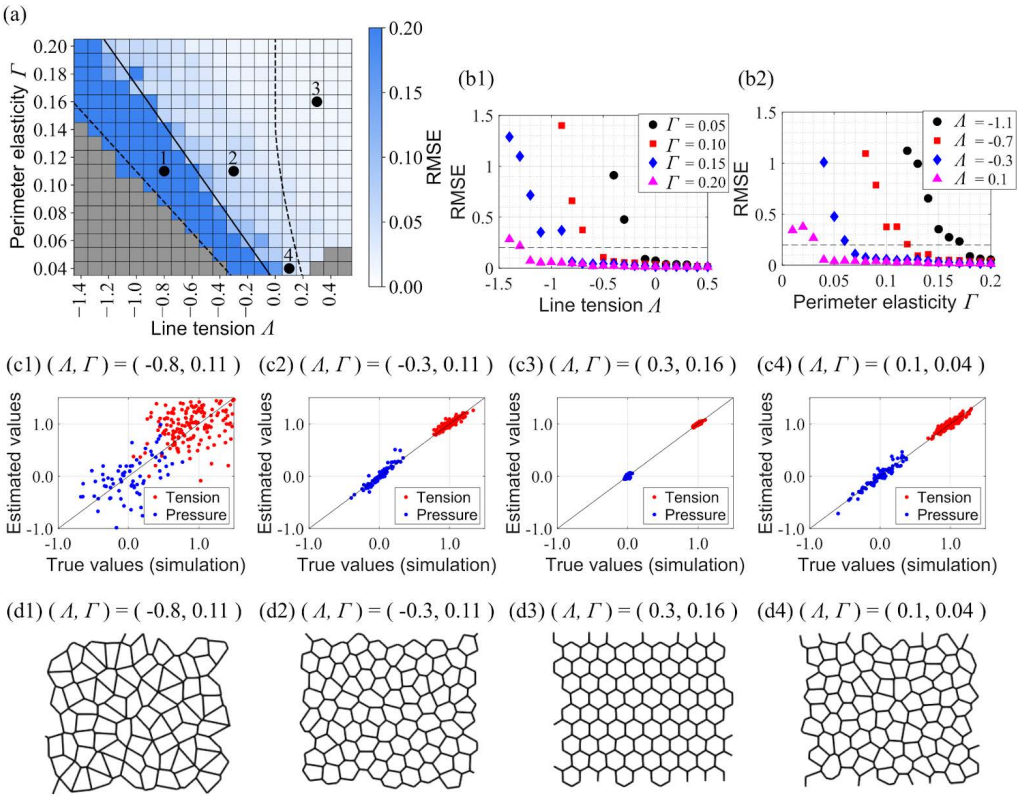

Fig. 2　Parameter dependence of estimation accuracy in systems with homogeneous cells

(a) Heatmap of RMSE in 2D parameter space of parameter elasticity and line tension (Λ, Γ): Gray cells indicate parameter sets for which the simulation stopped due to a large distortion of cell morphology. (b1, b2) Dependence of estimation accuracy on Λ and Γ: Dashed line shows the threshold of high-accuracy estimation. (c1-c4) Scatter plots of estimated values and true values at four representative points (1−4) indicated in (a), namely $(\Lambda, \Gamma) = (-0.8, 0.11)$, $(\Lambda, \Gamma) = (-0.3, 0.11)$, $(\Lambda, \Gamma) = (0.3, 0.16)$, and $(\Lambda, \Gamma) = (0.1, 0.04)$. The parameter set $(\Lambda, \Gamma) = (0.1, 0.04)$ was used by Ishihara *et al.* [9] for verifying their technique: All edge tensions (red) and cell pressures (blue) are plotted. (d1-d4) Cell morphology for four conditions simulated using 2D vertex model

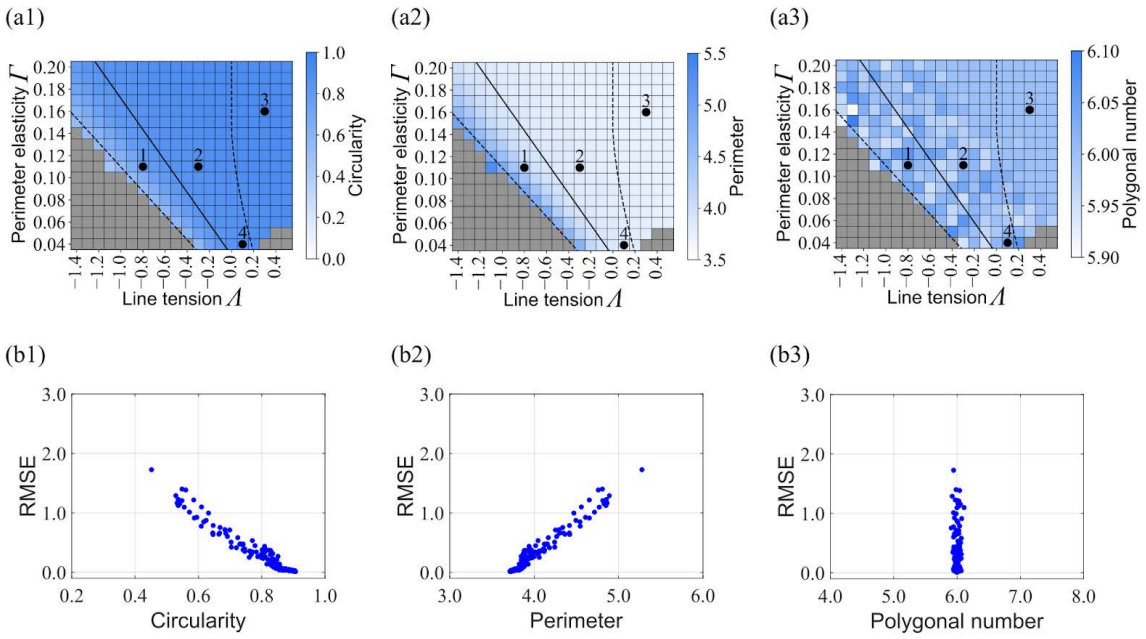

Fig. 3　Parameter dependence of cell shape characteristics and correlation with estimation accuracy

(a1-a3) Heatmap of cell shape characteristics (circularity, perimeter, and polygonal number) in 2D parameter space of parameter elasticity and line tension (Λ, Γ): Solid line is the threshold (RMSE = 0.2) and dashed lines divide the parameter region defined in a previous study [17]. Points 1−4 correspond to representative points in Fig. 2(a). (b1-b3) Scatter plots of RMSE versus cell shape characteristics obtained by comparing (a1-a3) and Fig. 2(a)

result, the correlation between the perimeter and accuracy is opposite to that of the correlation between circularity and accuracy. This is because a larger circularity generally results in a smaller perimeter, based on the definition of circularity ($4\pi s/p^2$). Furthermore, the results for the polygonal number are plotted in Fig. 3(a3, b3), where no correlation with accuracy is observed.

3.3. Estimation Accuracy for Heterogeneous Cells

To investigate the applicability of the force inference method to systems with heterogeneous cells, we conducted numerical simulations for various values of perimeter elasticity of individual cells and then applied the inference method to the resulting cell morphologies. The cell morphologies are shown in Fig. 4(a1-a4), where the color contours indicate the perimeter elasticity Γ of each cell. It is observed that cells with a lower perimeter elasticity tend to have a larger area. Scatter plots of the estimated and simulated force values are shown in Fig. 4(b1-b4). As σ_Γ increases, the dispersion of tension and pressure also increases; however, the estimated values are close to the true values even for large values of σ_Γ. Figure 5(a) shows the RMSE for each analysis. As shown in this plot, the RMSE increases with increasing perimeter elasticity σ_Γ. Nonetheless, the RMSE values for all four analyses remain below the threshold (RMSE < 0.2), indicating the possibility of estimating forces with high accuracy, at

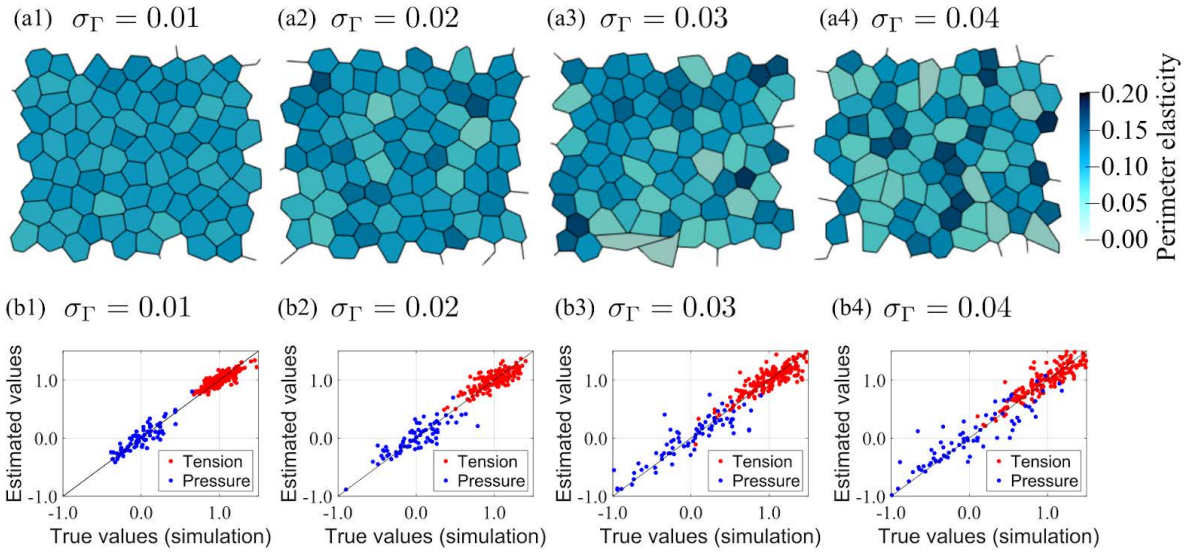

Fig. 4 Cell morphology and estimation accuracy in systems with heterogeneous cells

(a1-a4) Cell morphology calculated using 2D vertex model with perimeter elasticity having Gaussian distribution (expressed by color contour): The results were obtained under the conditions where the standard deviation of the perimeter elasticity is set as σ_Γ = 0.01, 0.02, 0.03, and 0.04. (b1-b4) Scatter plots of true and estimated values for each cell morphology

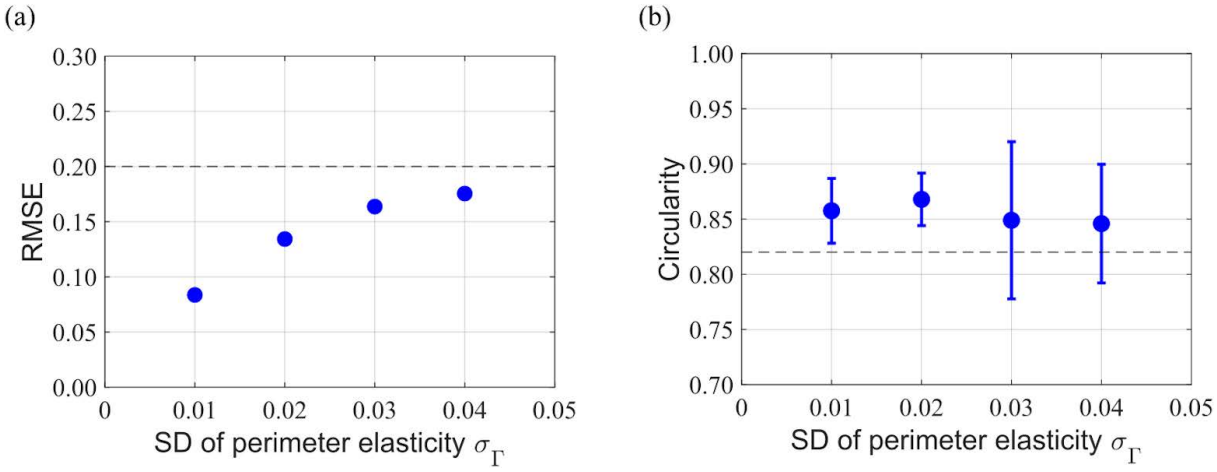

Fig. 5 Dependence of estimation accuracy and circularity on cell heterogeneity

(a) Dependence of estimation accuracy on the standard deviation of perimeter elasticity σ_Γ for system with heterogeneous cells: Dashed line is the RMSE threshold (0.2). (b) Circularity for each analysis condition: Points represent the mean circularity value and error bars represent its standard deviation. Dashed line is the circularity threshold (0.82). SD: standard deviation.

least within the heterogeneous range of $\sigma_\Gamma < 0.4$. The distribution of circularity for each analysis is shown in Fig. 5(b). The average circularity slightly decreases and its variance increases with increasing perimeter elasticity σ_Γ. All circularity values are either higher than or comparable to the circularity threshold (dashed line in the figure).

4 Discussion

In this study, we employed a two-dimensional vertex model to numerically assess the applicability of the force inference method proposed by Ishihara *et al.* [9] to systems with homogeneous and heterogeneous cells. The parameter map in Fig. 2(a) provides a visual aid for understanding the applicability of this method. To utilize this map, the perimeter elasticity and line tension of the observed cells must be obtained. These parameters can be derived by comparing simulated cell morphologies with actual cell shapes, as demonstrated in previous research on *Drosophila* cells [16], [17]. Our results are consistent with these earlier findings; the parameters for *Drosophila* cells fall within the high-precision range found in our study. Moreover, cell morphology can serve as an index of applicability. We found that when cell circularity exceeds 0.82, high-accuracy estimation is achieved. This suggests that researchers can assess applicability based on cell circularity, which can be calculated using standard microscopy software such as NIS-Elements (Nikon, Tokyo, Japan).

Our findings also indicate that this inference method is applicable to heterogeneous cell systems with a relative standard deviation of perimeter elasticity below 40%. This is due to the RMSE values falling below the established threshold (RMSE < 0.2). Circularity is also a useful index of applicability to heterogeneous cell systems, as demonstrated in Fig. 5(b) (circularity values above a threshold of 0.82). Under actual biological conditions, the mechanical and biochemical properties of cells may vary for a given cell type due to factors such as individual characteristics, the cell cycle, and apoptosis. In our study, we assumed that each cell has a distinct actin cytoskeleton and that perimeter elasticity has a Gaussian distribution. Our results show that the inference method is effective for systems that resemble actual biological conditions. By modifying other factors (*e.g.*, ideal cell area and initial edge length), we can further explore its applicability to heterogeneous systems.

The force inference method has the potential to replace conventional cell evaluation techniques. In medical cell diagnosis and cell culture studies, for example, the mechanical properties of cells could be used to identify senescent cells, which can be distinguished based on altered cell morphology [3]. Given that the estimation method is accurate even for systems with heterogeneous cells, it may be possible to calculate the force exerted on individual cells and distinguish senescent cells from healthy ones based on variations in applied force. If the forces between the two cell types significantly differ, the force distribution may become bimodal. As the prior distribution of Bayesian estimation is linked to force distribution, a potential avenue for future research is to update the prior distribution to further expand the applicability of the inference method. In this study, numerical simulations were used to validate and demonstrate the applicability of the inference method in heterogeneous cells systems, as described above. In order to establish its applicability to actual cells, it is necessary to quantitatively measure the forces acting between heterogeneous cells, and experimental verification is needed in the future.

5 Conclusion

Our study demonstrated the potential application of the force inference method proposed by Ishihara *et al.* [9] to heterogeneous cells systems using a 2D vertex model. Numerical simulations showed the effectiveness of this method in estimating forces for systems with either homogeneous or heterogeneous cells. We also showed the assessment of its applicability using cell circularity. Although we did not apply the method to actual medical diagnosis, our analyses suggest its potential use. Force inference methods have the potential to advance cell evaluation techniques in biomedicine.

Acknowledgments. We thank Dr. Shuji Ishihara for providing the data used to validate our estimation software.

References

[1] H. L. Ou, R. Hoffmann, C. González-López, G. J. Doherty, J. E. Korkola, and D. Muñoz-Espín, "Cellular senescence in cancer: from mechanisms to detection," *Mol Oncol.* vol. 15, no. 10, pp. 2634–2671, 2021.

[2] A. Giatromanolaki, M. Kouroupi, K. Balaska, and M. I. Koukourakis, "Immunohistochemical detection of senescence markers in human sarcomas," *Pathol Res Pract*, vol. 216, no. 2, 2020.

[3] C. Nafsika, M. Silvia, G. Costanza, Z. Xinyu, Z. Tomaso, and E. Vasileios, "Mechanical fingerprint of senescence in endothelial cells," *Nano Letters*, vol. 21, no. 12, p. 49114920,

2021.

[4] E. B. Suki and B. Suki, "Tuning mitochondrial structure and function to criticality by fluctuation-driven mechanotransduction," *Scientific Reports*, vol. 407, no. 10, 2020.

[5] J. S. de Sousa, R. S. Freire, F. D. Sousa, M. Radmacher, A. F. B. Silva, M. V. Ramos *et al*., "Double power-law viscoelastic relaxation of living cells encodes motility trends," *Scientific Reports*, vol. 4749, no. 10, 2020.

[6] W. Polacheck and C. Chen, "Measuring cell-generated forces: a guide to the available tools," *Nat Methods*, vol. 13, pp. 415–423, 2016.

[7] R. Fernandez-Gonzalez, S. M. Simoes, J. C. Roper, S. Eaton, and J. A. Zallen, "Myosin II dynamics are regulated by tension in intercalating cells," *Dev Cell*, vol. 17, no. 5, pp. 736–743, 2009.

[8] R. Krenger, J. T. Burri, T. Lehnert, B. J. Nelson, and M. A. M. Gijs, "Force microscopy of the Caenorhabditis elegans embryonic eggshell," *Microsyst Nanoeng*, vol. 29, no. 6, 2020.

[9] S. Ishihara and K. Sugimura, "Bayesian inference of force dynamics during morphogenesis," *Journal of Theoretical Biology*, vol. 313, pp. 201–211, 2012.

[10] S. Ishihara, K. Sugimura, S. J. Cox, I. Bonnet, Y. Bellaïche, and F. Graner, "Comparative study of non-invasive force and stress inference methods in tissue," *European Physical Journal E*, pp. 36–45, 2013.

[11] K. K. Chiou, L. Hufnagel, and B. I. Shraiman, "Mechanical stress inference for two dimensional cell arrays," *PLOS Computational Biology*, vol. 8, no. 5, 2012.

[12] G. W. Brodland, V. Conte, P. G. Cranston, J. Veldhuis, S. Narasimhan, M. S. Hutson, *et al*., "Video force microscopy reveals the mechanics of ventral furrow invagination in Drosophila," *Proc. Natl. Acad. Sci. U.S.A*, vol. 107, pp. 22111–22116, 20120.

[13] K. Sugimura, Y. Bellaïche, F. Graner, P. Marcq, and S. Ishihara, "Robustness of force and stress inference in an epithelial tissue," *Annu. Int. Conf. IEEE Eng. Med. Biol. Soc*., pp. 2712–2715, 2013.

[14] K. Sugimura and S. Ishihara, "The mechanical anisotropy in a tissue promotes ordering in hexagonal cell packing," *Development*, vol. 140, no. 19, pp. 4091–4101, 2013.

[15] S. Alt, P. Ganguly, and G. Salbreux, "Vertex models: from cell mechanics to tissue morphogenesis," *Philos Trans R Soc Lond B Biol Sci*, vol. 372, no. 1720, 2017.

[16] R. Farhadifar, J. C. Röper, B. Aigouy, S. Eaton, and F. Jülicher, "The influence of cell mechanics, cell-cell interactions, and proliferation on epithelial packing," *Current Biology*, vol. 17, no. 24, pp. 2095–2104, 2007.

[17] A. Adan, Y. Kiraz, and Y. Baran, "Cell proliferation and cytotoxicity assays," *Current Pharmaceutical Biotechnology*, vol. 17, pp. 1213–1221, 2016.

[18] J. Kursawe, R. E. Baker, and A. G. Fletcher, "Impact of implementation choices on quantitative predictions of cell-based computational models," *Journal of Computational Physics*, vol. 345, pp. 752–767, 2017.

[19] S. Okuda, E. Kuranaga, and K. Sato, "Apical Junctional Fluctuations Lead to Cell Flow while Maintaining Epithelial Integrity," *Biophysical Journal*, vol. 116, no. 6, pp. 1159–1170, 2019.

宮坂　翔　Shou MIYASAKA
先進技術開発本部 数理技術研究所
Mathematical Sciences Research Laboratory
Advanced Technology Research & Development

和泉啓太　Keita IZUMI
先進技術開発本部 数理技術研究所
Mathematical Sciences Research Laboratory
Advanced Technology Research & Development

奥田　覚　Satoru OKUDA
金沢大学
Kanazawa University

三木裕一朗　Yuichiro MIKI
先進技術開発本部 数理技術研究所
Mathematical Sciences Research Laboratory
Advanced Technology Research & Development

宮坂　翔
Shou MIYASAKA

和泉啓太
Keita IZUMI

三木裕一朗
Yuichiro MIKI

新規光学素子への応用に向けたLa_2O_3–TiO_2系超高屈折率ガラスの研究開発

吉本幸平，髙須脩平，上田　基，井上博之，増野敦信

La_2O_3-TiO_2-based Ultra-high Refractive Index Glasses for Application as New Optical Elements

Kohei YOSHIMOTO, Shuhei TAKASU, Motoi UEDA, Hiroyuki INOUE and Atsunobu MASUNO

高屈折率ガラスは光学機器の小型化や収差性能等の向上に不可欠であるが，通常の光学ガラスでは着色や結晶化などの問題により屈折率が2.0以下に制限されている．La_2O_3–TiO_2 (LT) ガラスは無容器法による合成が可能であり，2.3を超える屈折率と可視域において良好な光透過性を示す有望な材料である．しかし，ガラスサイズの制約（数 mm 以下）が応用における大きな課題であった．本研究では，多成分系 LT ガラスを開発し，従来の二成分系 LT ガラスに比べて大幅なサイズ拡大（直径 25 mm）を実現した．これにより，精密な屈折率計測とモールドプレス成形によるレンズ試作が可能となった．さらに，高エネルギー X 線回折および第一原理分子動力学計算による構造解析の結果，カチオン－酸素多面体の高配位構造や稜・面共有が確認され，これらの構造的特徴が高イオン充填構造に寄与していることが示唆された．また，電子状態解析から，カチオン - 酸素間におけるイオン結合性と酸素の電子分極率との間に相関関係が確認された．上記結果は，LT 系ガラスの光学素材としての応用に向けたマイルストーンであるとともに，本ガラス系の物性発現機構の理解にも繋がる知見であると考えられる．

High-refractive-index glasses are essential for downsizing optical systems and improving their performance. La_2O_3-TiO_2 (LT) glasses are promising candidates owing to their remarkably high refractive indices (> 2.3) and good optical transmittance in the visible range. However, practical application of LT glasses is limited by their low glass-forming ability and small size of obtainable samples. This paper reports the development of new multicomponent LT-based glasses with enhanced glass stability, enabling the fabrication of significantly larger samples (up to 25 mm in diameter) compared to binary LT glass. Precise refractive index measurements showed values between 2.16 and 2.31. Despite their high refractive indices, these glasses maintained good transmittance in the visible region. Prototype lenses were successfully fabricated using a glass molding press, demonstrating their potential for practical applications. High-energy X-ray diffraction experiment and *ab initio* molecular dynamics simulations revealed a unique glass structure characterized by high cation-oxygen coordination numbers and a prevalence of edge- and face-sharing polyhedral connections, contributing to the high packing density. Electronic structure analysis indicated that the predominantly ionic nature of the cation-oxygen bonds increased electron polarizability of oxygen atoms. These findings provide a fundamental understanding of the ultra-high refractive index exhibited by LT-based glasses.

Key words ガラス，高屈折率，構造解析，第一原理計算，無容器法
glass, high refractive index, structural analysis, *ab initio* calculation, containerless processing

1 Introduction

Optical glasses are essential components in various optical applications, including digital imaging cameras, objective lenses of microscopes, endoscopes, and binoculars. High-refractive-index glass is particularly advantageous for miniaturizing optical systems owing to them requiring less curvature of the lens for achieving the same focal power compared to that made of low-refractive-index glass [1]. High-refractive-index lenses also contribute to high performance of optical systems such as reduced aberrations, high numerical aperture, and adequate working distances [2]. Recently, augmented reality and mixed reality glasses have emerged as next-generation smart devices, requiring high-refractive-index substrates for waveguides to achieve sufficient fields of view [3]. Consequently, the demand for high-refractive-index optical glass is increasing. However, developing practical optical glasses with refractive indices exceeding 2.0 is challenging owing to limitations in glass stability against crystallization and coloration [4].

The La_2O_3–TiO_2 (LT) system is a promising candidate to address these issues. Binary LT glasses can be synthesized using containerless processing without requiring typical network formers such as SiO_2, B_2O_3, P_2O_5, and GeO_2 [5]–[8]. LT glasses exhibit significantly high refractive indices (> 2.3) and relatively high optical transmittance in the visible range despite the high refractive index [6]. The glass-forming region of the binary LT system is reportedly narrow, ranging from 66.7 to 76.2 mol% TiO_2, and the resulting glass size is typically limited to 2–3 mm in diameter [7]. To develop LT-based glasses for practical applications as optical materials, enlarging glass sizes and precisely measuring the optical properties are necessary. This study aimed to develop new LT-based multicomponent glasses that enable larger glass sizes and precise determination of optical properties. Furthermore, the mechanisms underlying the unique optical properties of LT-based glasses were investigated by analyzing the glass structures and electronic states through diffraction experiment and molecular dynamics simulations.

2 Methods

2.1. Glass Synthesis

Six multicomponent LT-based glasses were prepared. High-purity La_2O_3, Y_2O_3, TiO_2, ZrO_2, Ta_2O_5, Al_2O_3, and SiO_2 were mixed in stoichiometric ratios. The oxide components of each composition and sample name, abbreviated according to their composition, are presented in Table 1. For each composition, the mixed powder was pressed into a cylindrical pellet at 20 MPa and air-sintered at 1200°C for 12 h. The sintered pellet was placed on the gas nozzle of a self-built aerodynamic levitation system and levitated using airflow. The levitated sample was heated using 100 W CO_2 lasers. Post-melting, the lasers were turned off, and the melt was allowed to cool naturally to room temperature to form a glass.

2.2. Measurements of Thermal and Optical Properties

The glass transition temperature (T_g) and crystallization onset temperature (T_x) were determined by differential thermal analysis in air at a heating rate of 10°C/min using a Thermo Plus EVO2 TG8121 thermal analyzer (Rigaku Co. Ltd., Tokyo, Japan). All glass samples were annealed at approximately their T_g to remove internal strain. Density was measured using an AccuPyc II 1340 gas pycnometer (Micromeritics Instrument Co., Norcross, USA) with an accuracy of ± 0.01 g/cm^3. Refractive index was measured using one of three methods, depending on the sample size: the prism coupling, V-block, or minimum deviation methods. Details of the measurement procedure by the prism coupling method are described in our previous work [9]. Measurements by the V-block method were performed using a Kalnew KPR-3000 precision refractometer (Shimadzu Corp., Kyoto, Japan) with an accuracy of $\pm 1 \times 10^{-5}$. The measurements by minimum deviation method were performed using an HR SpectroMaster UV-VIS-IR high-precision spectrorefractometer (Trioptics GmbH, Hamburg, Germany) with an accuracy of $\pm 1 \times 10^{-6}$. Optical transmittance spectra were acquired at 300–700 nm using a UH4150 UV-Vis-NIR spectrophotometer (Hitachi High-Tech Corp., Tokyo, Japan).

2.3. Diffraction Experiment

High-energy X-ray diffraction (HEXRD) experiment was conducted at the BL04B2 beamline of the SPring-8 synchrotron radiation facility [10] for LTZ using 113 keV X-rays. The total correlation function ($T^x(r)$) was then obtained by the Fourier transformation of the structure factors from 0.3 to 22 Å^{-1}.

2.4. Molecular Dynamics Simulations

Structural models of six LT-based glasses were constructed using *ab initio* molecular dynamics (AIMD) simulations based on density functional theory. Simulations were performed using hybrid Gaussian and plane wave method implemented in the QUICKSTEP module of the CP2K code [11]. Details of the AIMD simulations are shown in Nikon Research Report Vol. 3. The classical molecular dynamics (CMD) simulations with the LAMMPS code were used to create the initial configuration for AIMD simulations [12]. Each simulation model contained approximately 550 atoms. Multiwfn software package was used for post-processing and electronic structures, including calculations of electron populations, bond orders, and localized functions were analyzed [13], [14].

Table 1 Oxide components contained in LT-based multicomponent glasses

	Oxide components
LT	La_2O_3, TiO_2
LTZ	La_2O_3, TiO_2, ZrO_2
LTS	La_2O_3, TiO_2, SiO_2
LTZS	La_2O_3, TiO_2, ZrO_2, SiO_2
LTZTS	La_2O_3, TiO_2, ZrO_2, Ta_2O_5, SiO_2
LYTZAS	La_2O_3, Y_2O_3, TiO_2, ZrO_2, Al_2O_3, SiO_2

3 Results and Discussion

3.1. Thermal Properties

Table 2 presents the results of thermal analysis and density measurements. The temperature gap between T_x and T_g, denoted as ΔT (= T_x − T_g), is used as a measure of glass stability against crystallization [15]. The results indicate that both ZrO_2 and SiO_2 enhance the thermal stability of the glass, with LTZS (containing both ZrO_2 and SiO_2) exhibiting the highest ΔT among the fabricated samples. Therefore, we attempted to increase the size of the LT-based multicomponent glasses using a larger-diameter gas nozzle. Consequently, larger glass samples were successfully fabricated: approximately 10 mm in diameter for LTZ, 15 mm for LTS and LTZTS, and 25 mm for LTZS and LYTZAS. However, for the binary LT, glasses with diameter larger than 3 mm could not be obtained owing to crystallization. Figure 1 shows the photograph of LT and LTZS.

3.2. Optical Properties

Larger sample sizes enabled precise refractive-index measurements, which were previously challenging with the typical 2–3 mm diameter glasses obtained by containerless processing. The refractive indices of LT were measured using the prism coupling method; LTS and LTZTS were measured using the V-block method; and LTZ, LTZS, and LYTZAS were measured using the minimum deviation method. Figure 2 presents the refractive index (n_d) and the Abbe number (ν_d) of the LT-based glasses, comparing them with those of commercial optical glasses. The Abbe number was calculated from the refractive indices at the F (486.133 nm), d (587.562 nm), and C (656.273 nm) lines as follows:

$$\nu_d = \frac{n_d - 1}{n_F - n_C} \quad (1)$$

In Fig. 2, the LT-based glasses exhibit significantly higher refractive indices and relatively larger dispersion compared

Table 2 Thermal properties and densities of LT-based glasses

	T_g (°C)	T_x (°C)	ΔT (°C)	ρ (g/cm^3)
LT	800	862	62	4.91
LTZ	810	922	112	5.06
LTS	781	916	135	4.57
LTZS	794	973	179	4.88
LTZTS	793	966	173	5.11
LYTZAS	811	920	109	4.89

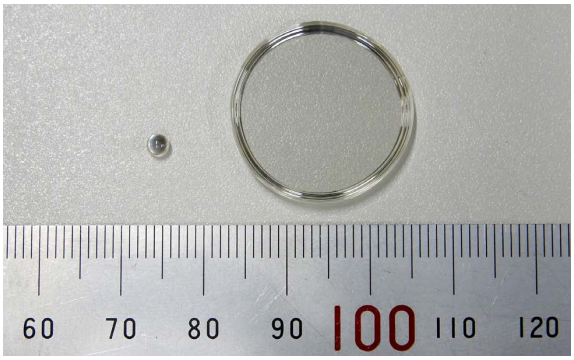

Fig. 1 Photograph of LT (left, 2.8 mm in diameter) and LTZS (right, 23 mm in diameter): LTZS is polished into disk (3 mm thickness) for the optical property measurement.

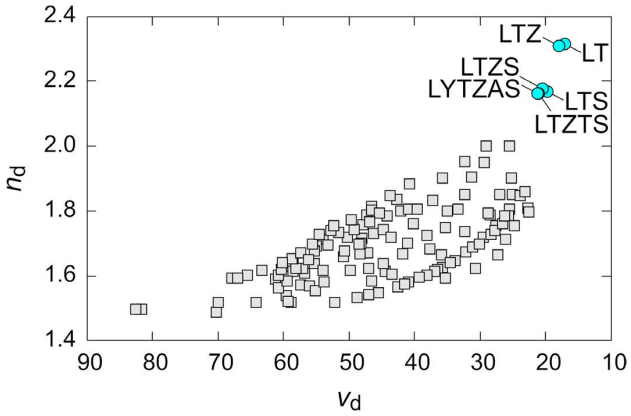

Fig. 2 Comparison of LT-based glasses (cyan circles) and commercial optical glasses (gray squares) in n_d vs. ν_d plot

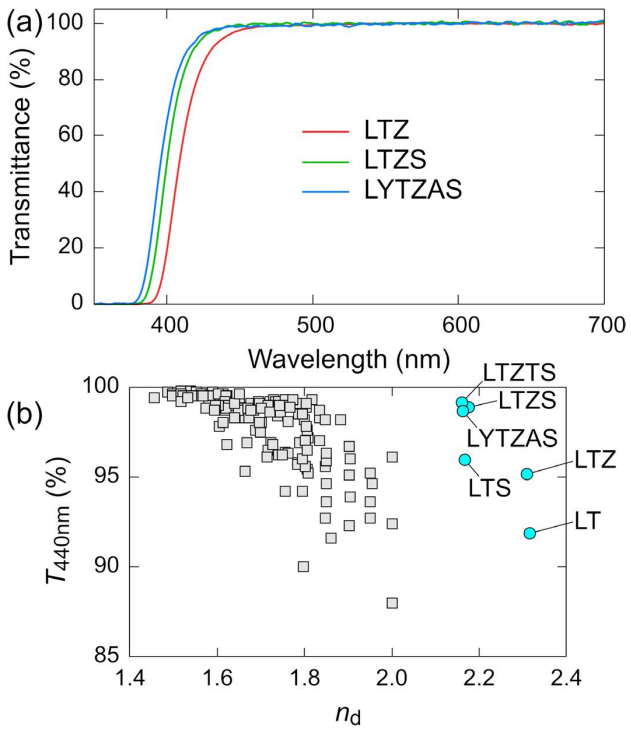

Fig. 3 (a) Internal transmittance spectra of LTZ, LTZS, and LYTZAS (10 mm thickness)
(b) Comparison of T_{440nm} and n_d for LT-based glasses (cyan circles) and commercial optical glasses (gray squares)

to the commercial optical glasses. LT and LTZ show particularly high refractive indices around 2.3, while the other SiO_2-containing compositions have refractive indices around 2.17.

The internal transmittance spectra of the LT-based glasses (10 mm thickness) are shown in Fig. 3(a). High transmittance is observed in the visible range, with a sharp absorption edge near 400 nm. Figure 3(b) shows the relationship between the internal transmittance at 440 nm (T_{440nm}, 10 mm thickness) and the refractive index (n_d) for both the LT-based glasses and commercial optical glasses. For both glass families, T_{440nm} tends to decrease with increasing n_d. However, the LT-based glasses maintain relatively high transmittance despite having significantly higher refractive indices than the commercial optical glasses.

3.3. Glass Molding Press

In this study, we developed multicomponent LT-based glasses with improved thermal stability, achieving glass sizes significantly larger than the typical 2–3 mm diameter obtained by containerless processing. These results motivated us to fabricate prototype lenses using a glass molding press in which glass preforms are reheated and molded into their final shape. The preform of LT-based glasses was placed between the molds and heated to a molding temperature above T_g of the sample. Once the molding temperature was reached, the upper mold was pressed onto the glass preform, giving it the shape of the mold. The molded sample was then released from the mold and polished to obtain the prototype lens. Using this method, a 25 mm diameter concave meniscus lens (Fig. 4(a)) and a 27 mm diameter biconvex lens (Fig. 4(b)) were fabricated from 20 mm diameter LYTZAS preforms. Furthermore, a 41 mm diameter, 1 mm thick wafer-shaped sample (Fig. 4(c)) was fabricated from a 22 mm diameter LTZS preform. No cracks or crystallization were observed in the molded samples. These results are expected to significantly expand the application potential of ultra-high refractive index glasses produced by containerless processing.

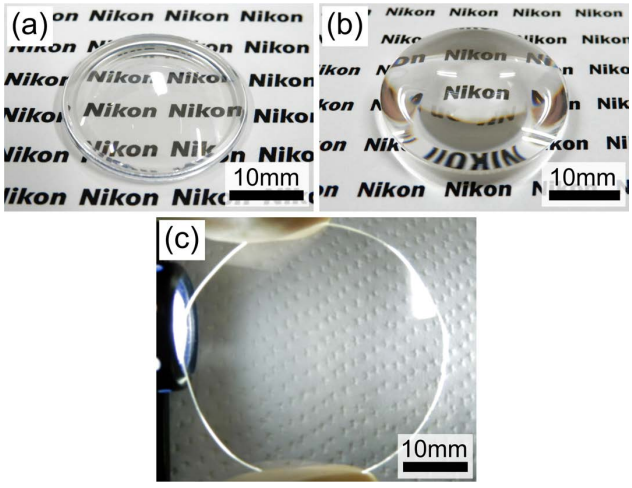

Fig. 4 Photographs of the prototype lenses of LT-based glasses fabricated using the glass molding test: (a) concave meniscus lens (LYTZAS, 25 mm in diameter), (b) biconvex lens (LYTZAS, 27 mm in diameter), and (c) wafer (LTZS, 41 mm in diameter).

3.4. Glass Structures

The X-ray weighted total correlation functions ($T^X(r)$s) for LTZ obtained from HEXRD experiments and AIMD are shown in Fig. 5(a). The AIMD-derived $T^X(r)$ agrees well with the experimental result, reproducing both the short-range order (~1–5 Å) and medium-range order (~5–10 Å) accurately. However, the mismatch at approximately 4 Å suggest that the M–M distance was reproduced slightly shorter in AIMD. The R_x factor, an agreement index [16] between the experimental and calculated $T^X(r)$s (calculated over the range of 1–10 Å), was 2.8%. Figure 5(b) shows the struc-

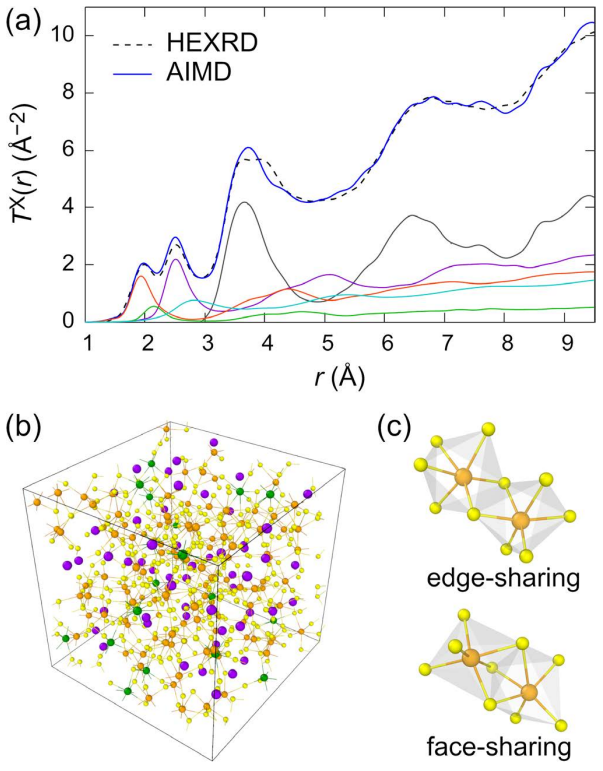

Fig. 5 (a) X-ray weighted total correlation functions, $T^X(r)$s, of LTZ obtained from HEXRD and AIMD simulations. Partial correlation functions for Ti–O (orange), La–O (violet), Zr–O (green), O–O (cyan), and M–M (gray) obtained from AIMD are also shown. (b) Snapshot of the LTZ structure obtained by AIMD simulation (c) Snapshot of edge- and face-sharing TiO_6–TiO_6 polyhedral linkages from the AIMD-derived structure
Atom colors: Ti (orange), Zr (green), La (violet), and O (yellow)

Table 3 Average M–O coordination numbers in LT-based glasses derived from AIMD

	N_{La-O}	N_{Y-O}	N_{Ti-O}	N_{Zr-O}	N_{Ta-O}	N_{Al-O}	N_{Si-O}
LT	8.97	–	5.67	–	–	–	–
LTZ	8.91	–	5.69	6.89	–	–	–
LTS	8.48	–	5.47	–	–	–	4.00
LTZS	8.83	–	5.68	7.06	–	–	4.08
LTZTS	8.74	–	5.58	6.94	6.11	–	4.15
LYTZAS	8.83	7.36	5.70	6.76	–	4.80	4.26

tural model of the LTZ obtained from AIMD simulation. The model suggests average M–O (M denotes the metal cation) bond lengths of 1.90 Å (Ti–O), 2.13 Å (Zr–O), and 2.49 Å (La–O) and average M–O coordination numbers of 5.69 (Ti–O), 6.89 (Zr–O), and 8.91 (La–O). A distinctive structural feature of LTZ is the large fraction of edge- and face-sharing connections between MO_n polyhedra (Fig. 5(c)). The connectivity between TiO_n polyhedra in LTZ was 69.8% corner-sharing, 28.9% edge-sharing, and 1.2% face-sharing, while the connectivity between LaO_n polyhedra was 35.7% corner-sharing, 48.7% edge-sharing, and 15.7% face-sharing. These structural features of high coordination numbers and prevalence of edge- and face-sharing polyhedral connectivity in LTZ do not follow the well-known Zachariasen's rules for glass formation [17].

Regarding the structural features of the LT-based glasses, Table 3 lists the average M–O coordination numbers derived from the AIMD simulations. Si, a typical network-former cation, exhibits 4-fold coordination with oxygen atoms. By contrast, transition metal cations (Ti, Zr, and Ta) show higher oxygen coordination numbers (approximately 6–7), and rare-earth cations (La and Y) have even higher coordination numbers (approximately 8–9 and 7, respectively). Figure 6 shows the average M–O coordination number (N_{M-O}) and the percentage of edge- and face-sharing MO_n–MO_n polyhedral linkages calculated from the AIMD models. The LT-based glasses in this study exhibit a positive correlation between the total fraction of edge- and face-sharing linkages and N_{M-O}. This suggests that the high proportion of edge- and face-sharing polyhedral connections in these glasses can be attributed to the high oxygen coordination numbers of the constituent rare-earth and transition metal oxides. Edge- and face-sharing polyhedral linkages reduce the inter-cation distances compared to corner-sharing, resulting in significantly high oxygen packing density in LT-based glasses [6], and consequently, contributing to the high refractive index.

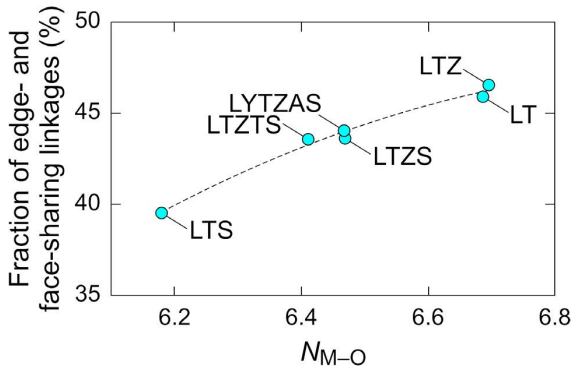

Fig. 6 Correlation between average coordination number (N_{M-O}) and the fraction of edge- and face-sharing polyhedral linkages in LT-based glasses (derived from AIMD simulations)
The dotted line is guide to the eye.

3.5. Electronic Structures

According to Mulliken population analysis [18], the net charge of atom A (ΔQ_A) is calculated by subtracting the gross atomic population (Q_A) from the nuclear charge (Z_A):

$$\Delta Q_A = Z_A - Q_A \tag{2}$$

Q_A is the sum of the net atomic population (Q_{AA}) and half of the total overlap population ($(1/2)\Sigma Q_{AB}$), where B represents an atom bonded to atom A:

$$Q_A = Q_{AA} + \frac{1}{2}\sum Q_{AB} \tag{3}$$

Q_{AA} and Q_{AB} are given by:

$$Q_{AA} = \sum_{\mu\in A}\sum_{\nu\in A}\sum_{i} n_i c_{\mu i} c_{\nu i} \int \chi_\mu(\mathbf{r})\chi_\nu(\mathbf{r})d\mathbf{r} \tag{4}$$

$$Q_{AB} = 2\sum_{\mu\in A}\sum_{\nu\in B}\sum_{i} n_i c_{\mu i} c_{\nu i} \int \chi_\mu(\mathbf{r})\chi_\nu(\mathbf{r})d\mathbf{r} \tag{5}$$

where $\chi_\mu(\mathbf{r})$ and $\chi_\nu(\mathbf{r})$ are the atomic orbitals; $c_{\mu i}$ and $c_{\nu i}$ are the contribution of $\chi_\mu(\mathbf{r})$ and $\chi_\nu(\mathbf{r})$ in the molecular orbital $\varphi_i(\mathbf{r})$; and n_i is the number of electrons in $\varphi_i(\mathbf{r})$. Figure 7 presents the results of population analysis based on above method for oxygen atoms in the LT-based glasses. The average electronic polarizability of oxygen atoms (α_O) was calculated using the procedure described in [6]. While the gross atomic population of oxygen (Q_O) shows minimal variation, the net atomic population (Q_{OO}) and the total overlap population (ΣQ_{OM}) exhibit significant changes with oxygen polarizability. The decrease in ΣQ_{OM} with increasing α_O suggests a decrease in covalent nature of O–M bonds. Furthermore, the increase in Q_{OO} implies an increase in the number of non-bonding electrons on oxygen atoms, which likely contributes to the increased oxygen polarizability. Table 4 lists the average bond orders of M–O pairs in each glass, calculated using the aforementioned Mulliken scheme

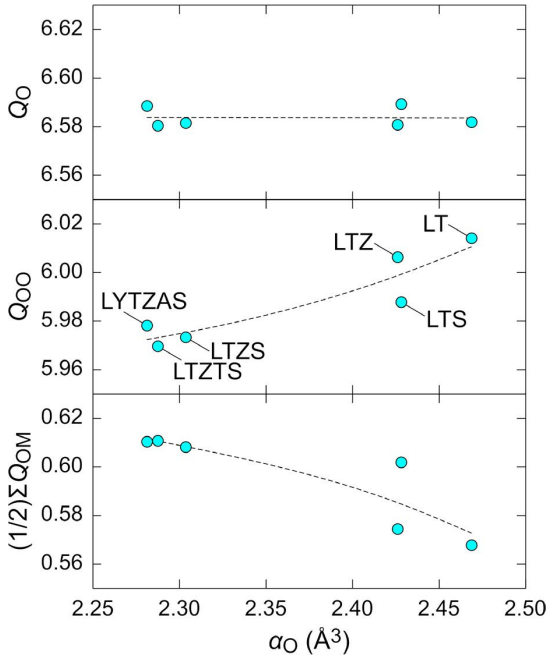

Fig. 7 Results of population analysis and electronic polarizability of oxygen atoms in LT-based glasses
Dotted lines are guides to the eye.

Table 4 Average bond orders of M–O pairs in LT-based glasses

	La–O	Y–O	Ti–O	Zr–O	Ta–O	Al–O	Si–O
LT	0.132	–	0.441	–	–	–	–
LTZ	0.132	–	0.435	0.393	–	–	–
LTS	0.145	–	0.445	–	–	–	0.873
LTZS	0.135	–	0.432	0.381	–	–	0.853
LTZTS	0.136	–	0.440	0.388	0.524	–	0.840
LYTZAS	0.135	0.241	0.431	0.395	–	0.409	0.821

(equivalent to Q_{MO} in Eq. (5)). Si–O bonds exhibit high values of bond order (> 0.8), indicating strong covalent character. By contrast, the transition metal and rare-earth cations, which are the primary components of the LT-based glasses, exhibit much lower values of bond order, indicating predominantly ionic bonds with oxygen atoms. These highly ionic characters increase the net atomic population of oxygen atoms (Q_{OO}), resulting in high electron polarizability of oxygen atoms.

Finally, the chemical bonding nature was visualized using the electron localization function (ELF) [19], as shown in Fig. 8. ELF is an indicator of electron localization in space [20]. In Fig. 8, the ELF localizes between Si and O atoms, indicating shared electron pairs and strong covalency of Si–O bonds. Meanwhile, the spherical distribution of ELF around oxygen atoms in Ti–O bonds suggests a more ionic bonding character.

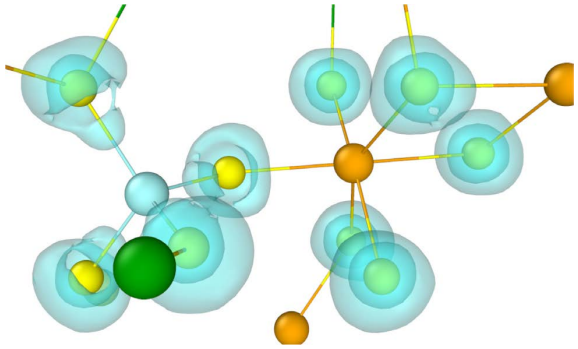

Fig. 8 ELF isosurface at level of 0.82 for SiO_4–TiO_6 fragment extracted from AIMD model of LTZS
Colors of atoms: Ti(orange), Zr (green), Si (cyan), and O (yellow)

4 Conclusion

This study successfully developed new multicomponent La_2O_3–TiO_2 (LT)-based glasses exhibiting enhanced thermal stability and significantly larger sizes compared to binary LT glasses. The incorporation of ZrO_2 and SiO_2 improved glass stability, enabling the fabrication of samples suitable for precise optical measurements and prototype lens production via glass molding press. These LT-based glasses exhibited exceptionally high refractive indices (n_d = 2.16–2.31) and good transmittance in the visible range, making them suitable candidates for a variety of optical applications. Structural analysis revealed a unique glass structure characterized by high coordination numbers and abundant edge- and face-sharing polyhedral linkages, possibly contributing to increased packing density. Notably, containerless processing allowed for achieving the glassy structure despite the presence of large fraction of edge- and face-sharing linkages. Furthermore, the predominantly ionic character of the cation–oxygen bonds resulted in increased oxygen polarizability, further enhancing the refractive index. This study demonstrated the potential of multicomponent LT-based glasses for practical applications requiring high-refractive-index materials. The findings indicate scope for future advancements in the miniaturization and performance enhancement of optical devices.

Acknowledgment. High-energy X-ray diffraction experiment was performed at beamline BL04B2 of SPring-8 under the approval of the Japan Synchrotron Radiation Research Institute (Proposal No. 2021A1297). This research utilized computational resources of the Oakforest-PACS supercomputer system provided by the Information Technology Center at the University of Tokyo. The authors thank all the members

at Advanced Technology Research & Development and Production Technology in Nikon Corp. for their support to this work.

References

[1] G. S. Jha, G. Seshadri, A. Mohan, and R. K. Khandal, "Sulfur containing optical plastics and its ophthalmic lenses applications," *e-Polym.,* vol. 8, no. 035, pp. 1–27, 2008.

[2] K. Watanabe and A. Nonaka, "Objective lens, optical system, and microscope," US. Patent 11782253B2, Oct. 2023.

[3] A. Kalinina and A. Putilin, "Wide-field-of-view augmented reality eyeglasses using curved wedge waveguide," in *Proceedings of SPIE*, vol. 11350, France, 2020, pp. 27–34.

[4] W. H. Dumbaugh, "Heavy metal oxide glasses containing Bi_2O_3," *Phys. Chem. Glasses,* vol. 27, no. 3, pp. 119–123, 1986.

[5] Y. Arai, K. Itoh, S. Kohara, and J. Yu, "Refractive index calculation using the structural properties of $La_4Ti_9O_{24}$ glass," *J. Appl. Phys*., vol. 103, 094905, 2008.

[6] H. Inoue, Y. Watanabe, A. Masuno, M. Kaneko, and J. Yu, "Effect of substituting Al_2O_3 and ZrO_2 on thermal and optical properties of high refractive index La_2O_3–TiO_2 glass system prepared by containerless processing," *Opt. Mater.,* vol. 33, no. 12, pp. 1853–1857, 2011.

[7] M. Kaneko, J. Yu, A. Masuno, H. Inoue, M. S. V. Kumar, O. Odawara, and S. Yoda, "Glass formation in $LaO_{3/2}$–TiO_2 binary system by containerless processing," *J. Am. Ceram. Soc*., vol. 95, no. 1, pp. 79–81, 2011.

[8] A. Masuno, Y. Watanabe, H. Inoue, Y. Arai, J. Yu, and M. Kaneko, "Glass-forming region and high refractive index of TiO_2-based glasses prepared by containerless processing," *Phys. Status Solidi C*, vol. 9, no. 12, pp. 2424–2427, 2012.

[9] K. Yoshimoto, A. Masuno, M. Ueda, H. Inoue, H. Yamamoto, and T. Kawashima, "Low phonon energies and wideband optical windows of La_2O_3-Ga_2O_3 glasses prepared using an aerodynamic levitation technique," *Sci. Rep*., vol. 7, 45600, 2017.

[10] S. Kohara, M. Itou, K. Suzuya, Y. Inamura, Y. Sakurai, Y. Ohishi, and M. Takata, "Structural studies of disordered materials using high-energy X-ray diffraction from ambient to extreme conditions," *J. Phys.: Condens. Matter,* vol. 19, 506101, 2007.

[11] J. VandeVondele, M. Krack, F. Mohamed, M. Parrinello, T. Chassaing, and J. Hutter, "Quickstep: Fast and accurate density functional calculations using a mixed Gaussian and plane waves approach," *Comput. Phys. Commun*., vol. 167, no. 2, pp. 103–128, 2005.

[12] S. Plimpton, "Fast parallel algorithms for short-range molecular dynamics," *J. Comput. Phys.,* vol. 117, no. 1, pp. 1–19, 1995.

[13] T. Lu and F. Chen, "Multiwfn: A multifunctional wavefunction analyzer," *J. Comput. Chem*., vol. 33, no. 5, pp. 580–592, 2012.

[14] T. Lu, "A comprehensive electron wavefunction analysis toolbox for chemists, Multiwfn," *J. Chem. Phys*., vol. 161, 082503, 2024.

[15] A. Dietzel, "Glasstruktur und Glaseigenschaften," *Glastech. Ber*., vol. 22, pp. 41–50, 1948.

[16] A. C. Wright, "Neutron scattering from vitreous silica. V. The structure of vitreous silica: What have we learned from 60 years of diffraction studies?," *J. Non-Cryst. Solids*, vol. 179, pp. 84–115, 1994.

[17] W. H. Zachariasen, "The atomic arrangement in glass," *J. Am. Chem. Soc*., vol. 54, no. 10, pp. 3841–3851, 1932.

[18] R. S. Mulliken, "Electronic population analysis on LCAO–MO molecular wave functions. I.," *J. Chem. Phys*., vol. 23, no. 10, pp. 1833–1840, 1955.

[19] T. Lu and F.-W. Chen, "Meaning and functional form of the electron localization function," *Acta Phys.-Chim. Sin*., vol. 27, no. 12, pp. 2786–2792, 2011.

[20] A. Savin, R. Nesper, S. Wengert, and T. F. Fässler, "ELF: The electron localization function," *Angew. Chem. Int. Ed. Engl*., vol. 36, no. 17, pp. 1808–1832, 1997.

吉本幸平　Kohei YOSHIMOTO
生産本部 技術統括部 光学素材部
Optical Material Department
Technology Sector
Production Technology

髙須脩平　Shuhei TAKASU
先進技術開発本部 材料・要素技術研究所
Materials & Advanced Research Laboratory
Advanced Technology Research & Development

上田　基　Motoi UEDA
先進技術開発本部
Advanced Technology Research & Development

井上博之　Hiroyuki INOUE
東京大学
The University of Tokyo

増野敦信　Atsunobu MASUNO
京都大学
Kyoto University

Nikon Research Report Vol. 7
Published October 2025

Unauthorized reproduction prohibited

NIKON CORPORATION